博士論文

DOCTORAL DISSERTATION

モード分割多重伝送のための
選択型モード合分波器に関する研究

Study on Selective Mode Multiplexer for Mode Division Multiplexing Transmission

北海道大学　大学院情報科学院

Hokkaido University Graduate School of Information Science

メディアネットワークコース

Media Network Course

情報通信フォトニクス研究室

Laboratory of Information Communication Photonics

王　晗

HAN WANG

Contents

Chapter 1 Introduction 4

1.1 Research background of mode division multiplexing 4

1.2 Mode multiplexing transmission system 7

1.3 Background of PLC photonic lantern mode MUXs 8

1.4 Background of PLC E31, E13 mode converters 10

1.5 Background of photonic crystal mode MUXs 11

1.6 Content and innovation points 12

Chapter 2 Numerical analysis method 15

2.1 Preface 15

2.2 Basic equations for waveguide propagation analysis 15

2.3 Perfectly Matched Layer 16

2.4 Formulation of 3D scalar finite element beam propagation method 18

Chapter 3 PLC photonic lantern 4-mode selective MUX 22

3.1 Preface 22

3.2 Waveguide modes and optical fiber modes 22

3.3 PLC photonic lantern 4-mode MUX 23

Chapter 4 Photonic lantern 6-mode selective MUX/DMUX 28

4.1 Preface 28

4.2 Structural design of PLC photonic lantern 6-mode MUX 28

4.3 Performance evaluation of PLC photonic lantern 6-mode MUX/DMUX 36

Chapter 5 Photonic lantern 10-mode selective MUX/DMUX 40

5.1 Preface 40
5.2 Structural design of PLC photonic lantern 10-mode MUX 40
5.3 Performance evaluation of PLC photonic lantern 10-mode MUX/DMUX 48
Chapter 6 PLC E31, E13 taper mode converters using FAQUAD method 52
6.1 Preface 52
6.2 The principles of FAQUAD method 53
6.3 PLC FAQUAD E_{31}-E_{13} taper mode converter 55
6.4 PLC FAQUAD E-LP taper mode converter for 6-mode photonic lantern MUX 62
6.5 PLC FAQUAD E-LP taper mode converter for 10-mode photonic lantern MUX 66
Chapter 7 Photonic crystal mode MUXs 73
7.1 Preface 73
7.2 The working principle of photonic crystal 74
7.3 PBG calculation method – plane wave expansion method 77
7.4 5-mode MUX using pillar type PCWs 80
7.5 Ultra-compact 2-mode MUX using air-hole type PCWs 86
Chapter 8 Conclusion 93
Acknowledgements 95
Research achievements 96
References 98

Copyright Notice

This thesis summarizes, analyzes, and reorganizes based on the following papers.

Chapter 1 Introduction

1.1 Research background of mode division multiplexing

In recent years, with the advancement of communication technology, the number of Internet users is growing exponentially. With the popularization of personal mobile communication terminals such as smartphones and tablet computers has shifted the primary means through which people understand the world from traditional information sources like television and broadcasts to digitized forms such as online news and short videos. Humanity is taking significant strides toward becoming an all-network information society. With the gradual popularization of advanced technologies such as 4k/8k high-quality video technology and Internet of Things (IoT) technology, communication technology, which is the basic technology supporting the Internet, needs to make progress in the direction of larger communication capacity and lower consumption of electric power in order to provide more efficient and higher-quality advanced services brought about by the advancement of the Internet. The COVID-19 in 2020 has brought a great impact on people's lives. Online meetings and remote work surged in popularity, leading to a substantial increase in Internet users. Even today, many IT companies are continuing to promote remote work. These are bringing greater challenges to the communication industry undoubtedly.

Traditional communication systems utilize electrical currents or microwaves as signal carriers, and copper cables or air as transmission medium. The bandwidth of electrical current signals is significantly constrained due to the low-frequency characteristics. Additionally, copper cables or air have a strong absorption effect on the signal but are also susceptible to the influence of the external environment, which leads to a large loss. In 1966, Chinese-American scientist Charles Kuen Kao proposed optical fiber could be used as a medium of information transmission [1],

introduced a new development direction for the communication industry, and this groundbreaking idea earned him the Noble Prize in Physics in 2009. Since the first development of optical fibers with a loss rate below 20 dB/km by Corning Inc. in 1970, optical fiber communication technology has continuously evolved. From data centers to communication base stations and extending to fiber-to-the-home connections, contemporary communication technology has transformed into a foundation supported primarily by optical fiber-based wired and wireless communications.

Traditional Single-Mode optical Fibers (SMFs) have been widely used due to propagating only one mode, resulting in smaller mode dispersion and crosstalk. For optical fiber transmission, the dimensions that can carry information include wavelength, polarization, and phase, among others. Since the 1980s, optical fiber communication technology has undergone multiple technological innovations in these dimensions. The developments in Time Division Multiplexing (TDM), Wavelength Division Multiplexing (WDM), Polarization Division Multiplexing (PDM), and Orthogonal Frequency Division Multiplexing (OFDM) have significantly enhanced the communication capacity of SMFs. However, the communication capacity of SMFs cannot be infinitely increased. Issues such as multiple inputs, increasing optical power, and the emergence of nonlinear optical effects impose physical limitations on the communication capacity of traditional SMFs. This limit is known as the nonlinear Shannon limit of 100 Tb/s, as shown in Fig. 1.1 [2]. In order to break through this limit, optical fiber communication systems need to increase communication capacity and reduce power consumption.

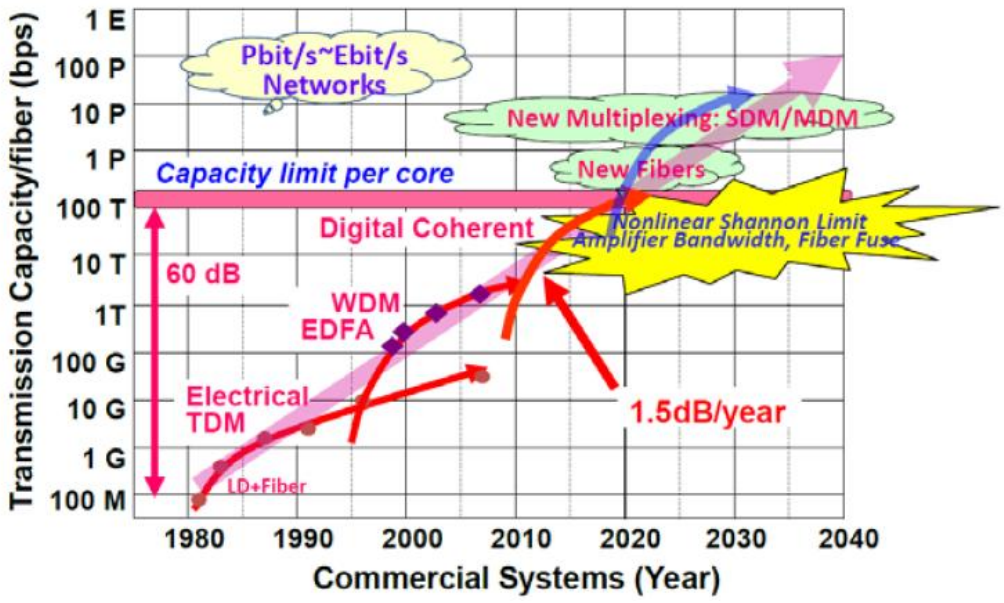

Figure 1.1 Development trend of optical communication capacity [2].

In the context where the information dimensions of optical transmission such as wavelength, polarization, and phase have been explored, it is necessary to make breakthroughs in new dimensions to further enhance the communication capacity of optical fiber transmission. Space Division Multiplexing (SDM) technology, focusing on the spatial dimension, has garnered increasing attention from researchers [3]. As shown in Fig. 1.2, SDM technology can be broadly categorized into two main directions. One is the Multi-Core Fiber (MCF) technology in which multiple cores are configured in a single fiber, where uncoupled MCFs refer to multiple cores with sufficient spacing between them to avoid coupling. Conversely, coupled MCFs exhibit inter-core coupling, resulting in the output of either super modes (strong coupling) or modes with crosstalk (weak coupling). This necessitates Digital Signal Processing (DSP) techniques at the receiver sides to separate modes or eliminate crosstalk. The other direction is Mode Division Multiplexing (MDM) technology. MDM technology allows optical fibers to support the propagation of higher-order modes beyond the fundamental mode by expanding the core diameter of a conventional SMF. These modes are orthogonal to each other and thus can carry different information as independent signal channels, thereby significantly increasing the communication capacity.

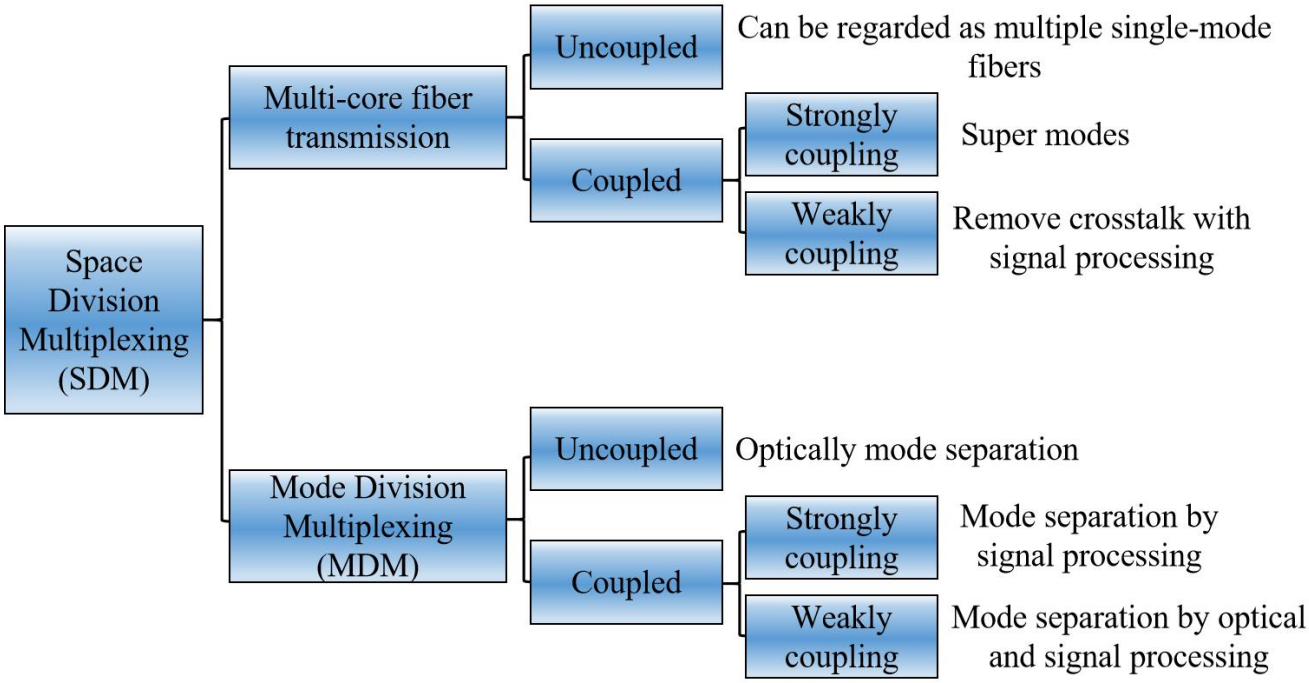

Figure 1.2 Classification of space division multiplexing.

1.2 Mode multiplexing transmission system

Figure 1.3 shows the structure of a simple MDM transmission system. First, at the signal-sending end, various signal sources modulate information onto fundamental modes (LP_{01} mode) of SMFs. Subsequently, multiple SMFs through a mode Multiplexer (MUX) to multiplex the LP_{01} mode into various higher-order LP_{mn} modes of a Few-Mode Fiber (FMF) for transmission. At the signal reception end, a mode Demultiplexer (DMUX) separates the different modes within the FMF into the fundamental mode of various SMFs. The optical signals are then converted to digital signals by photo-detectors. Multiple Input Multiple Output (MIMO) signal processing technique is used to process signals, such as remove crosstalk and reduce mode dispersion loss. Finally, the receivers receive the signals. Similar to WDM systems, MDM systems require a series of passive devices for support, such as fiber input/output [4], connectors between fibers or fiber and waveguides [5], and active components like optical amplifiers [6]. Among these, the mode MUX/DMUX is a mode control device used to realize mode conversion, coupling, and separation. It is undoubtedly the key device in the

MDM transmission system.

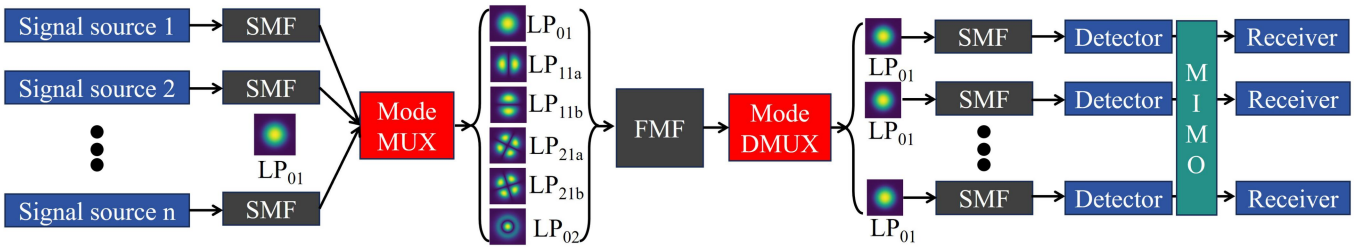

Figure 1.3 Mode division multiplexing system.

1.3 Background of PLC photonic lantern mode MUXs

According to electromagnetic theory, modes are stable field distributions based on the refractive index distribution of the waveguide cross-section that satisfies Maxwell's equations. The difference between each mode is mainly reflected in the intensity and phase of the mode field distribution. In other words, by controlling the mode field and phase distribution, conversion between modes can be achieved.

Based on the working principle of mode conversion, mode MUXs are generally categorized into spatial-type mode MUX utilizing spatial light field matching, fiber-type mode MUX based on optical fibers and waveguide-type mode MUX designed to control optical modes through optical waveguide structures. Spatial-type mode MUXs typically implemented using a combination of prisms, phase, and spatial light modulators [7], [8]. Fiber-type mode MUXs usually implemented by directly designing the fiber structure or tapering the fiber, such as fused fiber Directional Coupler (DC) [9] and fiber-type photonic lantern [10]–[16].

With the development and progress of semiconductor technology, applications such as data centers and communication base stations increasingly demand optical communication devices to evolve towards smaller sizes and greater integration at the chip level. Integrated optical waveguides have gained increasing attention in this context. Optical waveguide refers to a medium geometric structure that can confine light waves inside or on the surface of a medium and guide the light waves to propagate along a specific path. The mainstream optical waveguide material platforms include SiO_2 [17]–[21], Si [22], polymers [23]–[25], and others. Among them, silica-based Planar Lightwave Circuits (PLCs) are characterized by low

transmission losses and share the same material as optical fibers, facilitating convenient connectivity with optical fibers.

As shown in Fig. 1.4, previous PLC mode MUXs have mostly been based on Asymmetric Directional Coupler (ADC) structures [17]. As the number of multiplexing modes gradually increases, the structure of the ADC device will become very complex, and the volume will also increase greatly. From previous research on fiber-type mode MUXs, mode MUX using photonic lanterns has the characteristics of easy expansion of the number of modes, broad applicable wavelength range, and small device size [11]. The study of waveguide-type photonic lanterns can solve the problem of increasing the number of modes in ADC mode MUXs while reducing device size.

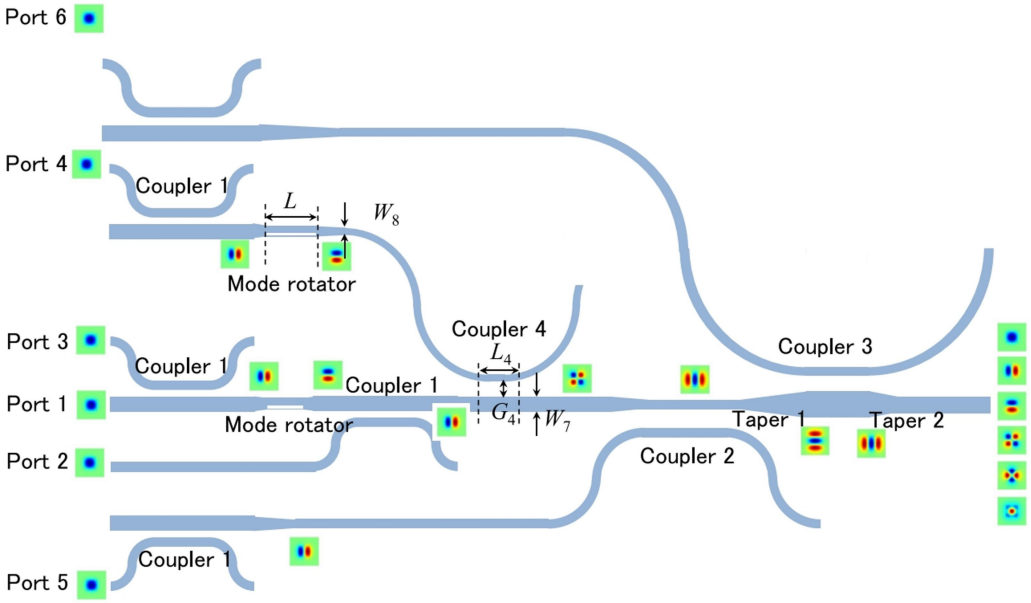

Figure 1.4 PLC 6-mode MUX based on ADCs [17].

The output end of the non-selective mode MUX is difficult to distinguish because all modes are involved, these modes follow several different propagation paths. Since the length of each propagation path can be different, the delay time of each propagation path will be different, and complex MIMO processing is required after output, making the entire process very complicated [17]. The mode-selective mode MUX can obtain the specific mode which is desired at the multi-mode output port by selecting the single-mode input port, to equalize mode dependent effects such as Mode Dependent Loss (MDL) [26].

A photonic lantern selective 4-mode MUX composed of polymer waveguides

was proposed [27], which offers advantages such as a simple structure and a compact device size. However, it supports only four modes, and compared to polymer waveguides, PLCs exhibit better stability, lower losses, and can be easily connected to optical fibers. Therefore, in this study, we attempt to use PLC to design a photonic lantern mode MUX and explore the expansion of the number of modes in PLC-based photonic lantern mode MUX by adopting new design methods and designing new structures.

1.4 Background of PLC E_{31}, E_{13} mode converters

In PLC mode MUX, the cross-section of the output port is often designed as a rectangle (which means that the waveguide width W and the waveguide height H are not equal), which makes the output mode a rectangular waveguide mode. As shown in Fig. 1.5, rectangular waveguide modes and fiber LP-like modes have different field distributions in high-order modes such as E_{31} and E_{13} modes. To avoid unnecessary losses during the connection between PLC mode MUX and optical fibers, a mode converter consisting of a tapered structure is usually introduced at the rectangular output port to realize the conversion between rectangular waveguide modes and fiber LP-like modes.

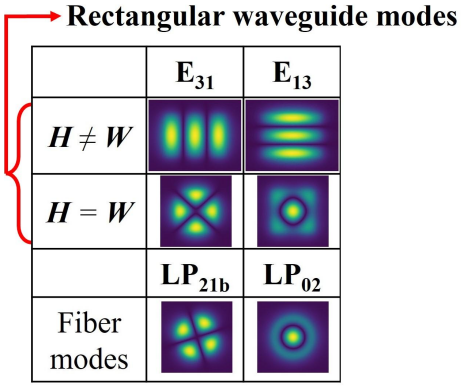

Figure 1.5 Corresponding relationship between rectangular waveguide modes and optical fiber modes.

Previous PLC E_{31} and E_{13} mode converters have utilized linear taper structures to satisfy adiabatic coupling conditions and achieve high-order mode conversion. In recent years, a quantum-inspired technique known as Shortcut to Adiabaticity (STA) has been increasingly used in the field of optics [28]. A novel STA protocol

called Fast Quasi-Adiabatic Dynamics (FAQUAD) has been proposed recently [29]. This method aims to accelerate the adiabatic coupling process by controlling adiabatic parameters to achieve uniform distribution during the coupling process. Devices such as Y-branch waveguides [30]–[32] and ADCs [33]–[35] designed using the FAQUAD method have been reported, demonstrating adiabatic coupling even with relatively short device lengths. However, current research on the FAQUAD protocol is mainly limited to Si and polymer platforms. While PLC mode converters for E_{12} and E_{21} modes have been proposed [36], these designs only consider structurally complex 2-LP mode conversion and have not explored higher-order modes. Therefore, in this study, we will discuss FAQUAD E_{31} and E_{13} mode converters tailored for matching photonic lantern mode MUXs [37].

1.5 Background of photonic crystal mode MUXs

In recent years, nanophotonic technology has received significant attention from researchers to meet the high integration requirements of chip-level communication devices. Photonic Crystals (PC) in nanophotonic technology, due to their unique bandgap characteristics and high integration density, have been extensively studied and applied in the WDM technology. As shown in Fig. 1.6, a PC is formed by the periodic arrangement of one medium in another, resulting in a Photonic Band Gap (PBG) — a special bandgap characteristic. Utilizing the PBG, removing a medium pillar/air hole from the complete PC structure can form a point defect, creating a PC cavity. Similarly, removing a row of medium pillars/air holes forms a line defect, leading to the formation of a Photonic Crystal Waveguide (PCW) (specific principles will be described in detail in Chapter 7 of PC mode MUX).

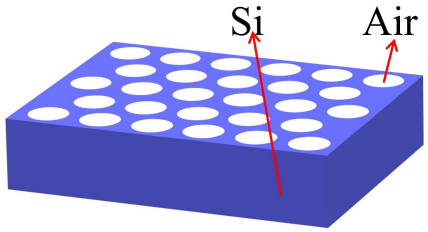

Figure 1.6 2D air-hole triangular-lattice PC.

To further increase optical communication capacity, hybrid multiplexing technology combining WDM and MDM has been reported [38]–[40]. This

technology significantly increases the number of channels by simultaneously realizing both WDM and MDM technologies, thereby expanding communication capacity substantially. However, these studies often rely on two different structures: the WDM part typically uses PC structures due to the small device size and high Q-factor of PC cavities, while the MDM part typically uses Si wire waveguide structures. The connection between the two different structures leads to significant losses, with literature indicating that the losses in the connection segment can account for up to 30% of the overall losses in the hybrid MUX [38]. If one aims to retain the advantages of a PC structure in WDM while reducing the losses of the hybrid MUX, the entire MUX needs to be designed using PC structures. Therefore, the study on PC mode MUX is necessary.

Currently, research on PC mode MUX mainly focuses on structures utilizing dielectric pillar-type PCs [39], [41]. Pillar-type PCs are formed by periodically arranging dielectric pillars in the air, but at present, they can only support 2-mode multiplexing and are considered impractical from a manufacturing perspective. In this study, we accumulate design methods for PCs by discussing the mode expansion of pillar-type PC mode MUX [42] and will mainly discuss the air-hole-type PC mode MUX [43] that is more realistically manufacturable.

1.6 Content and innovation points

Based on the above research background, we conducted a study on PLC photonic lantern mode MUXs. Subsequently, as a sequel to the photonic lantern mode MUX, we investigated PLC mode converters using the FAQUAD protocol. Finally, in response to the increasing demand for higher integration of optical devices, we conducted research on PC mode MUXs.

The following is the outline of this paper.

Chapter 1: We introduced the research background of MDM technology, MDM transmission system, PLC photonic lantern mode MUX, PLC mode converter, and PC mode MUX respectively.

Chapter 2: We will introduce the derivation of the calculation formula of the optical waveguide analysis method mainly used in this study. Depending on the

design of each device, we also need to use some specific calculation methods, which will be described separately in each device chapter.

Chapter 3: In this chapter, we will present a PLC photonic lantern 4-mode MUX. We demonstrate the feasibility of changing the photonic lantern structure from polymer material to PLC in the designing of PLC photonic lantern mode MUXs.

Chapter 4: We will introduce the design and optimization method of the PLC photonic lantern 6-mode MUX, and then evaluate the performance through simulation.

Chapter 5: We will introduce the design and optimization method of the PLC photonic lantern 10-mode MUX, and then evaluate the performance through simulation.

Chapter 6: This chapter introduces the PLC E_{31} and E_{13} mode converters designed using the FAQUAD protocol, and evaluate the performance through simulation.

Chapter 7: In this chapter, we will introduce the design of the pillar-type PC 5-mode MUX and verify the mode scalability of the pillar-type PC. Then the design of air-hole-type PC 2-mode MUX is introduced.

Chapter 8: We will show the conclusion of this paper.

The innovative points of this paper are as follows:

- We expanded the previous photonic lantern 4-mode MUX to 6 and 10 modes, which greatly increased the number of channels and thus expanded the communication capacity. Compared with the previous PLC ADC 6-mode MUX [17], the size of the PLC photonic lantern 6-mode MUX has been reduced by more than 2/3 in the propagation direction. The PLC photonic lantern 10-mode MUX was the first PLC 10-mode-selective MUX at the time the structure was published.
- We proposed a new initial structure design method for photonic lanterns. By matching the fundamental mode of the input port and the high-order mode of the output port, the initial structure can be more conveniently determined, and the complexity of the optimization process is reduced.
- We designed E_{31}-E_{13}, E-LP taper mode converters using FAQUAD protocol. The tapered length of the E_{31}-E_{13} mode converter has been significantly

reduced from 30,000 μm for the previous one-stage taper structure and 12000 μm for the three-stage taper structure [17] to 4000 μm. The taper length of the E-LP mode converter has been significantly reduced to 4000 μm from the previous 50000 μm for one-section taper structures and 6000 μm for two-section taper structure [17].

- We proposed the first air-hole PC mode MUX and verified the possibility of utilizing air-hole PCs for MDM transmission.

Chapter 2 Numerical analysis method

2.1 Preface

The Finite Element Method (FEM) is a kind of numerical analysis technology born from the field of structural mechanics. From the second half of the 1960s to the 1970s, the research of the finite element method applied in the field of electronic, electrical, information, and communication engineering began gradually. The finite element method is an attempt to solve a differential equation related to a target system by applying the variational principle to a function instead of directly solving it. The target region is divided into small parts called elements, it is an analysis method by connecting each element together at a node.

The Beam Propagation Method (BPM) is one of the electromagnetic field analysis methods when the waveguide structure changes very slowly. In this study, we analyze the propagation of optical waveguides using FEM-based BPM.

In this chapter, we formulate the 3D Scalar Finite Element Beam Propagation Method (3D-SFE-BPM) [44] for propagation analysis.

2.2 Basic equations for waveguide propagation analysis

Consider a case where an electromagnetic wave having an angular frequency ω and a propagation constant β propagates through an optical waveguide having an arbitrary shape cross section Ω in the xy plane and having a uniform structure and the same dielectric constant in the propagation direction z. Here, the phasor display electric field $\widetilde{\boldsymbol{E}}$, magnetic field $\widetilde{\boldsymbol{H}}$, electric flux density $\widetilde{\boldsymbol{D}}$, and magnetic

flux density $\widetilde{\boldsymbol{B}}$, which are related as

$$\boldsymbol{E}(\boldsymbol{r},t) = \mathrm{Re}[\widetilde{\boldsymbol{E}}(\boldsymbol{r}_t)\exp\{j(\omega t - \beta z)\}] \tag{2.1}$$

$$\boldsymbol{H}(\boldsymbol{r},t) = \mathrm{Re}[\widetilde{\boldsymbol{H}}(\boldsymbol{r}_t)\exp\{j(\omega t - \beta z)\}] \tag{2.2}$$

$$\boldsymbol{D}(\boldsymbol{r},t) = \mathrm{Re}[\widetilde{\boldsymbol{D}}(\boldsymbol{r}_t)\exp\{j(\omega t - \beta z)\}] \tag{2.3}$$

$$\boldsymbol{B}(\boldsymbol{r},t) = \mathrm{Re}[\widetilde{\boldsymbol{B}}(\boldsymbol{r}_t)\exp\{j(\omega t - \beta z)\}]\,, \tag{2.4}$$

are introduced here, and these are used as a function of the position $\boldsymbol{r}_t$ in the waveguide cross section, and written to $\boldsymbol{E}$, $\boldsymbol{H}$, $\boldsymbol{D}$, $\boldsymbol{B}$, the Maxwell equation becomes.

$$\nabla \times \boldsymbol{E} = -j\omega\boldsymbol{B} \tag{2.5}$$

$$\nabla \times \boldsymbol{H} = j\omega\boldsymbol{D} \tag{2.6}$$

$$\nabla \bullet \boldsymbol{D} = 0 \tag{2.7}$$

$$\nabla \bullet \boldsymbol{B} = 0 \tag{2.8}$$

2.3 Perfectly Matched Layer

In BPM analysis, since the size of the analysis area is finite, it is necessary to load a Perfectly Matched Layer (PML) to attenuate the radiated waves. Figure 2.1 shows a two-dimensional cross section of an optical waveguide loaded with anisotropic PML around the analysis area. W_x and W_y are the analysis region sizes in the x and y directions, respectively, and d_1 to d_4 are the thicknesses of the anisotropic PML region.

Maxwell's equations with anisotropic PML introduced can be written as

$$\nabla \times \boldsymbol{E} = -j\omega\mu_0[s]\boldsymbol{H} \tag{2.9}$$

$$\nabla \times \boldsymbol{H} = -j\omega\varepsilon_0 n^2[s]\boldsymbol{E} \tag{2.10}$$

$$\nabla \bullet \boldsymbol{D} = 0 \tag{2.11}$$

$$\nabla \bullet \boldsymbol{B} = 0\,, \tag{2.12}$$

n is the refractive index, and ε_0 and μ_0 are the vacuum permittivity and the vacuum magnetic permeability, respectively. Here, the matrix [s] is a PML parameter given by

$$s=\begin{bmatrix} s_y/s_x & 0 & 0 \\ 0 & s_x/s_y & 0 \\ 0 & 0 & s_x s_y \end{bmatrix} \tag{2.13}$$

and s_x, s_y is defined as shown in Table 2.1. Here, s_i (i = 1 ~ 4) in the table is defined as

$$s_i = 1 - i\alpha_i \tag{2.14}$$

At this time, α_i is a parameter that controls the attenuation of light waves in the PML region, and is represented by a square distribution as

$$\alpha_i = \left(\frac{\rho}{d_i}\right)^2 \tan\delta_i, \tag{2.15}$$

where the distance from the PML surface is ρ. Here, δ_i represents the loss angle in the PML region. Equations (2.9) to (2.12) can be expanded to

$$\frac{\partial E_z}{\partial y} - \frac{\partial E_y}{\partial z} = -j\omega\mu_0 \frac{s_y}{s_x} H_x \tag{2.16a}$$

$$\frac{\partial E_x}{\partial z} - \frac{\partial E_z}{\partial x} = -j\omega\mu_0 \frac{s_x}{s_y} H_y \tag{2.16b}$$

$$\frac{\partial E_y}{\partial x} - \frac{\partial E_x}{\partial y} = -j\omega\mu_0 s_x s_y H_z \tag{2.16c}$$

$$\frac{\partial H_z}{\partial y} - \frac{\partial H_y}{\partial z} = j\omega\varepsilon_0 n^2 \frac{s_y}{s_x} E_x \tag{2.17a}$$

$$\frac{\partial H_x}{\partial z} - \frac{\partial H_z}{\partial x} = j\omega\varepsilon_0 n^2 \frac{s_x}{s_y} E_y \tag{2.17b}$$

$$\frac{\partial H_y}{\partial x} - \frac{\partial H_x}{\partial y} = j\omega\varepsilon_0 n^2 s_x s_y E_z \tag{2.17c}$$

$$\frac{\partial}{\partial x}\left(\frac{s_y}{s_x}E_x\right) + \frac{\partial}{\partial y}\left(\frac{s_x}{s_y}E_y\right) + \frac{\partial}{\partial z}\left(s_x s_y E_z\right) = 0 \tag{2.18}$$

$$\frac{\partial}{\partial x}\left(\frac{s_y}{s_x}H_x\right) + \frac{\partial}{\partial y}\left(\frac{s_x}{s_y}H_y\right) + \frac{\partial}{\partial z}\left(s_x s_y H_z\right) = 0. \tag{2.19}$$

Here, E_x, E_y, E_z, H_x, H_y, H_z are the electric and magnetic field components in the x, y, z direction, respectively.

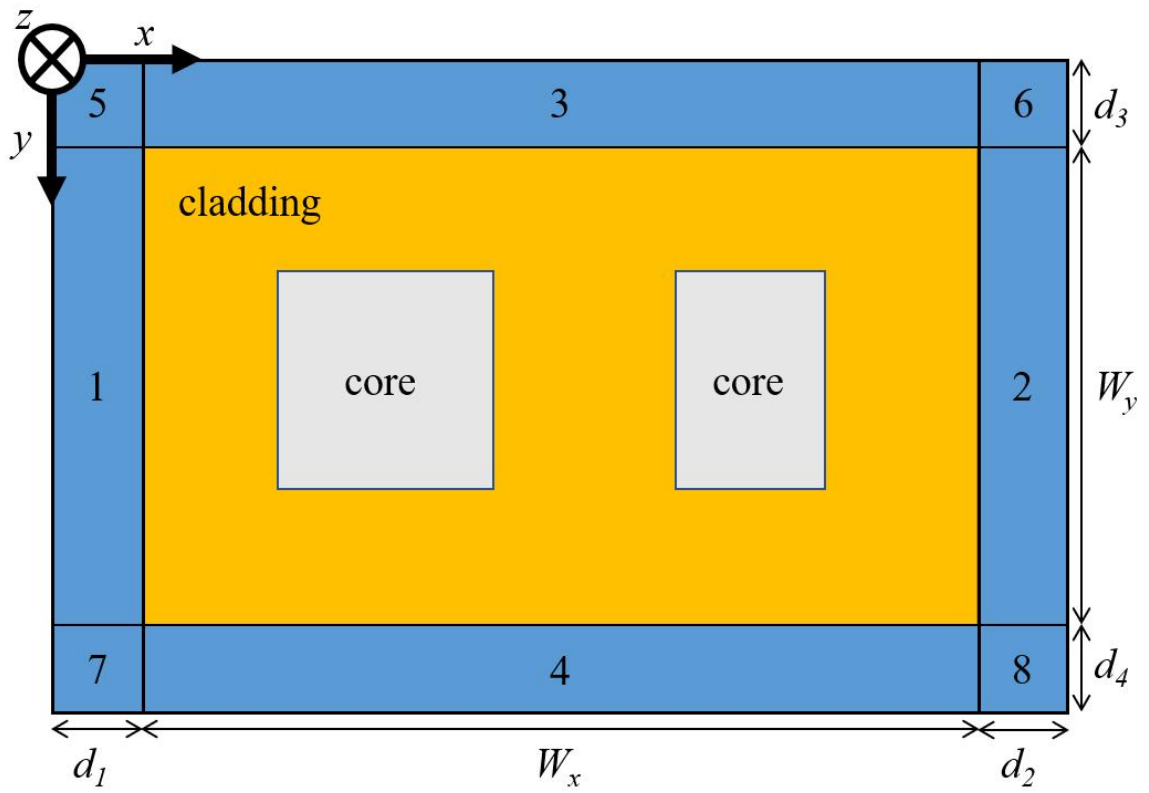

Figure 2.1 Two-dimensional cross section of an optical waveguide loaded with anisotropic PML around the analysis area.

Table 2.1 PML parameter.

PML Parameter	PML region							
	1	2	3	4	5	6	7	8
s_x	s_1	s_2	1	1	s_1	s_2	s_1	s_2
s_y	1	1	s_3	s_4	s_3	s_3	s_4	s_4

2.4 Formulation of 3D scalar finite element beam propagation method

Substituting (2.16b) and (2.16c) into equation (2.17a) and using the scalar wave approximation, the E_x mode scalar wave equation

$$\frac{\partial}{\partial x}\left(\frac{s_y}{s_x^3}\frac{\partial E_x}{\partial x}\right)+\frac{\partial}{\partial y}\left(\frac{1}{s_x s_y}\frac{\partial E_x}{\partial y}\right)+\frac{\partial}{\partial z}\left(\frac{s_y}{s_x}\frac{\partial E_x}{\partial z}\right)+k_0^2 n^2\frac{s_y}{s_x}E_x=0 \tag{2.20}$$

can be obtained. Further, by substituting (2.17b) and (2.17c) into equation (2.16a) and using the scalar wave approximation, the E_y mode scalar wave equation

$$\frac{\partial}{\partial x}\left(\frac{1}{n^2}\frac{s_y}{s_x^3}\frac{\partial H_x}{\partial x}\right)+\frac{\partial}{\partial y}\left(\frac{1}{n^2}\frac{1}{s_x s_y}\frac{\partial H_x}{\partial y}\right)+\frac{\partial}{\partial z}\left(\frac{1}{n^2}\frac{s_y}{s_x}\frac{\partial H_x}{\partial z}\right)+k_0^2\frac{s_y}{s_x}H_x=0 \tag{2.21}$$

can be obtained. Equations (2.20) and (2.21) can be summarized as

$$\frac{\partial}{\partial x}\left(p\frac{s_y}{s_x^3}\frac{\partial \Phi}{\partial x}\right)+\frac{\partial}{\partial y}\left(p\frac{1}{s_x s_y}\frac{\partial \Phi}{\partial y}\right)+\frac{\partial}{\partial z}\left(p\frac{s_y}{s_x}\frac{\partial \Phi}{\partial z}\right)+k_0^2 q\frac{s_y}{s_x}\Phi=0 \tag{2.22}$$

$$\begin{cases}\Phi=E_x\\ p=1\\ q=n^2\end{cases}\quad \text{For } E^x \text{ mode}$$

$$\begin{cases}\Phi=H_x\\ p=1/n^2\\ q=1\end{cases}\quad \text{For } E^y \text{ mode.}$$

The electromagnetic field Φ is divided into a term that changes slowly and a term that changes rapidly in the z direction Slowly Varying Envelope Approximation (SVEA), and is approximated to

$$\Phi(x,y,z)=\phi(x,y,z)\exp(-jk_0 n_0 z)\ , \tag{2.23}$$

using complex amplitude ϕ and reference refractive index n_0. Substituting equation (2.23) into (2.22) and setting $\partial\rho / \partial z = 0$ for E^y mode, the basic equation for the beam propagation method

$$p\frac{s_y}{s_x}\left(\frac{\partial^2\phi}{\partial z^2}-2jk_0 n_0\frac{\partial\phi}{\partial z}\right)+p\frac{\partial}{\partial x}\left(\frac{s_y}{s_x^3}\frac{\partial\phi}{\partial x}\right)+p\frac{\partial}{\partial y}\left(\frac{1}{s_x s_y}\frac{\partial\phi}{\partial y}\right)+k_0^2\frac{s_y}{s_x}\left(q-n_0^2 p\phi\right)=0 \tag{2.24}$$

is obtained.

The cross section of the optical waveguide is divided using the nodal element as shown in Fig. 2.2, and ϕ in each element is expressed as the following equation using the node value vector $\{\phi\}_e$ in the element.

$$\phi = \{N\}^{\mathrm{T}} \{\phi\}_e \tag{2.25}$$

Here, $\{N\}^{\mathrm{T}}$ is a shape function vector for the nodal element, and its contents are shown in Table 2.2. L_1, L_2, L_3 in the table are area coordinate variables. Substituting equation (2.25) into (2.24) and applying FEM gives.

$$[M]\frac{d^2\{\phi\}}{dz^2} - 2jk_0 n_0 [M]\frac{d\{\phi\}}{dz} + \left([K] - k_0^2 n_0^2 [M]\right)\{\phi\} = \{0\} \tag{2.26}$$

The matrices [K], [M] are given by equations (2.27) and (2.28), respectively.

$$[K] = \sum_e \iint_e \left[k_0^2 q \frac{s_y}{s_x} \{N\}\{N\}^{\mathrm{T}} - p\frac{s_y}{s_x^3}\frac{\partial\{N\}}{\partial x}\frac{\partial\{N\}^{\mathrm{T}}}{\partial x} - p\frac{1}{s_x s_y}\frac{\partial\{N\}}{\partial y}\frac{\partial\{N\}^{\mathrm{T}}}{\partial y} \right] dxdy \tag{2.27}$$

$$[M] = \sum_e \iint_e p\frac{s_y}{s_x}\{N\}\{N\}^{\mathrm{T}}\, dxdy \tag{2.28}$$

Applying the Padé approximant to equation (2.26) gives

$$-2jk_0 n_0 \left[\widetilde{M}\right]\frac{d\{\phi\}}{dz} + \left([K] - k_0^2 n_0^2 [M]\right)\{\phi\} = \{0\}. \tag{2.29}$$

The matrix [$\widetilde{M}$] is given as follows.

$$\left[\widetilde{M}\right] = [M] + \frac{1}{4k_0^2 n_0^2}\left([K] - k_0^2 n_0^2 [M]\right) \tag{2.30}$$

Applying the Crank Nicholson method to equation (2.29) gives a sequential equation.

$$[A]_i \{\phi\}_{i+1} = [B]_i \{\phi\}_i \tag{2.31}$$

$$[A]_i = -2jk_0 n_0 \left[\widetilde{M}\right]_i + 0.5\Delta z\left([K]_i - k_0^2 n_0^2 [M]_i\right) \tag{2.32}$$

$$[B]_i = -2jk_0 n_0 \left[\widetilde{M}\right]_i - 0.5\Delta z\left([K]_i - k_0^2 n_0^2 [M]_i\right) \tag{2.33}$$

Here, Δz is the step size in the propagation direction, and the subscript i represents the quantity related to the i-th propagation step. By giving the incident electromagnetic field distribution as the initial value, the electromagnetic field can be obtained sequentially.

Also, the reference index of refraction n_0 in each propagation step is updated by

$$n_{0,i}^2 = \mathrm{Re}\left[\frac{\{\phi\}_i^{\dagger} [K]_i \{\phi\}_i}{{k_0}^2 \{\phi\}_i^{\dagger} [M]_i \{\phi\}_i} \right]. \tag{2.3}$$

Here, † means complex conjugate transpose.

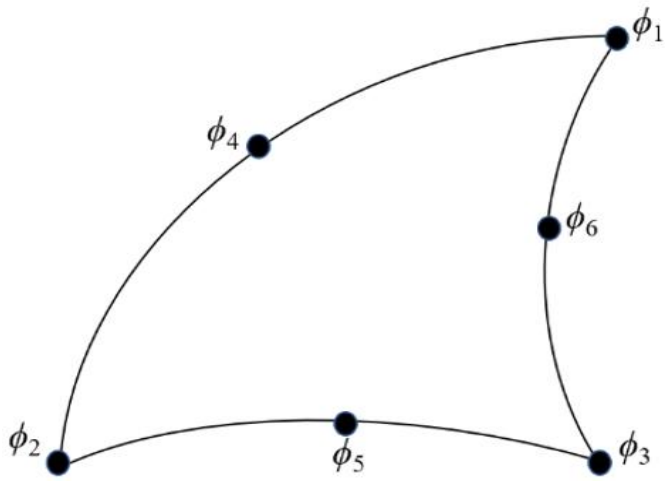

Figure 2.2 Triangle nodal element.

Table 2.2 Shape function vector for triangular nodal elements.

	Basic elements	**Higher-order elements**
$\{N\}$	$\begin{bmatrix} L_1 \\ L_2 \\ L_3 \end{bmatrix}$	$\begin{bmatrix} L_1(2L_1-1) \\ L_2(2L_2-1) \\ L_3(2L_3-1) \\ 4L_1L_2 \\ 4L_2L_3 \\ 4L_3L_1 \end{bmatrix}$

Chapter 3 PLC photonic lantern 4-mode selective MUX

3.1 Preface

The mode MUX with high mode selectivity can be realized by several waveguide structures, such as directional coupler structure [17], asymmetric Y-branch structure [45], and photonic lantern structure to achieve mode selective multiplexing. As the number of modes increases, the structure of the directional coupler type and asymmetric Y-branch structure will become very complicated, and the device volume will increase. Through the research of the previous fiber-type photonic lantern mode multiplexer, we know that the photonic lantern structure can increase the number of multiplexed modes simply and have the benefit of reducing the size of the device and can effectively reduce the high Insertion Loss (IL) and Mode Dependent Loss (MDL) caused by the number of modes increases. So far, photonic lantern mode multiplexers used fiber type [46], waveguide type using femtosecond laser [47]–[49], and waveguide type using polymer material have been reported [27], [50]. To verify the feasibility of the photonic lantern based on the PLC planar waveguide, we first proposed a 4-mode-selective photonic lantern mode MUX based on PLC.

3.2 Waveguide modes and optical fiber modes

Before designing the device, to ensure that the device can be easily connected to

the optical fiber, we have defined the corresponding relationship between the rectangular waveguide modes and the optical fiber modes, as shown in Fig. 3.1. Modes described in this paper (E_{11}, E_{21}, E_{12}, E_{22}, E_{31}, E_{13}, E_{32}, E_{23}, E_{41}, and E_{14} modes) refers to the rectangular waveguide modes when $H \neq W$.

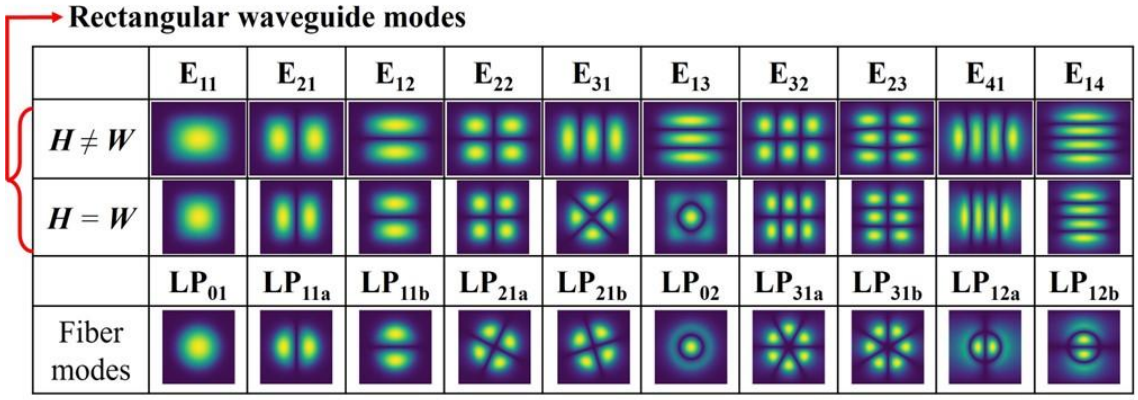

Fig. 3.1 Corresponding relationship between rectangular waveguide modes and optical fiber modes.

3.3 PLC photonic lantern 4-mode MUX

Figures 3.2 (a), (b), and (c) show the 3D structure of the entire device, XZ cross-sectional structure, and XY cross-sectional structure of the multi-mode output port of the PLC 4-mode-selective photonic lantern mode multiplexer respectively. It has a two-layer PLC structure in which four S-bend single-mode rectangular waveguides are close to each other, combined into a multimode waveguide.

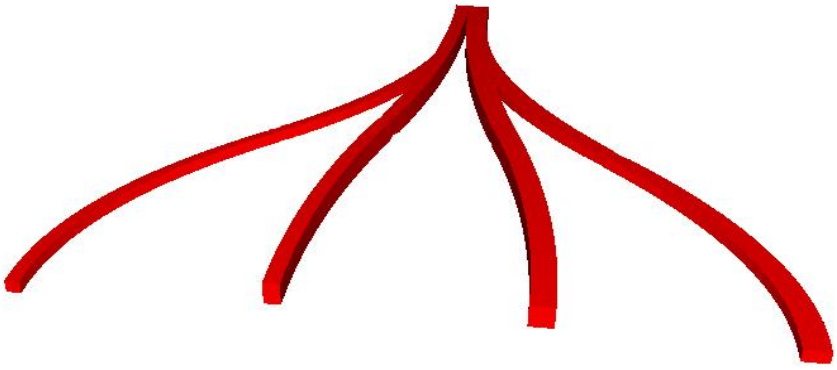

(a) 3D structure.

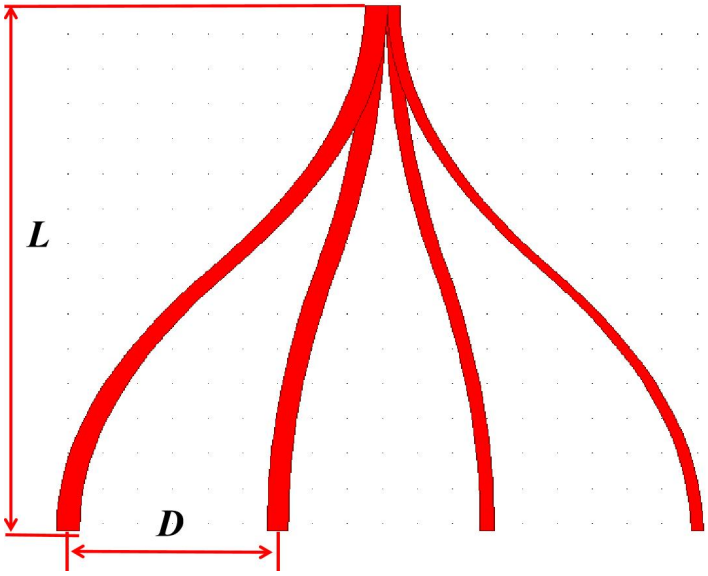

(b) XZ cross-sectional structure.

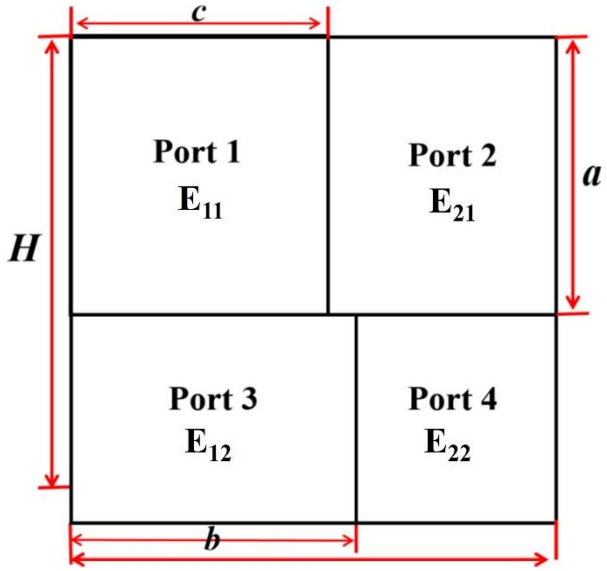

(c) XY cross-sectional structure of the multi-mode output port.

Figure 3.2 Structure of PLC photonic lantern 4-mode-selective MUX.

The previous photonic lantern mode MUX only supported four modes. As shown in Fig. 3.2 (c), the design focused on parameters *a*, *b*, and *c* can achieve 4-mode selective multiplexing. According to reference [27], in a two-layer photonic lantern structure, when the heights of the two layers are set to $a = 0.65*H$ and $H - a = 0.35*H$, each mode achieves a relatively high transmission. In other words, in the case of 4-mode, we only need to focus on the design of the two parameters *b* and *c* to easily realize 4-mode selective multiplexing. However, as the number of modes increases, the number of ports and the corresponding

parameters for each port will also increase accordingly, making the design and optimization processes very complex. Therefore, for the future expansion of modes in the photonic lantern mode MUX, we propose a novel and convenient method for designing the initial structure of the photonic lantern as follows.

To simplify the design process and achieve mode matching between single-mode input ports and multi-mode output port, here we introduce the parameter Δn_{eff}, where n_{eff} expresses the effective refractive index. The effective refractive index difference Δn_{eff} should be as close to 0 as possible. Δn_{eff} indicates the correspondence between the desired output port mode and input E_{11} mode to determine the widths of each branch waveguide in the initial structure. When the Δn_{eff} gets close to 0, the desired mode is easier to excite.

$$\Delta n_{eff} = n_{eff}(\text{Output} \quad \text{Mode}) - n_{eff}(\text{Input} \quad \text{LP}_{01} \quad \text{Mode}) \tag{3.1}$$

Figures 3.3 (a) and (b) show the relationship between the widths of each single-mode port and Δn_{eff} of each desired mode. From Fig. 3.3, the multi-mode waveguide composed of four single-mode waveguides is H = 10 μm in height and W = 10 μm in width, and the parameters of each single-mode waveguide are a = 6.5 μm, b = 6.5 μm, c = 6 μm. The total length of the device is L = 15 mm, and the distance between each single-mode port is D = 60 μm. The refractive index of the silica cladding is assumed to be 1.444. The relative refractive difference is Δ = 1.0 %. When E_{11} mode is input from Port1, it is coupled to E_{11} mode, when E_{11} mode is input from Port2, it is coupled to E_{21} mode, when LP_{01} mode is input from Port3, it is coupled to E_{12} mode, when E_{11} mode is input from Port4, it is coupled to E_{22} mode. Figures 3.4 (a)~(d) show the electric field distribution at the multi-mode output port when E_{11} mode is input from each single-mode port respectively, which is calculated by the BPM (Rsoft). It can be seen from Fig. 3.4 that this device has realized E_{11}, E_{21}, E_{12}, and E_{22} 4-mode multiplexing with high mode-selectivity. The transmission of each mode is E_{11}: -0.025 dB, E_{21}: -0.073 dB, E_{12}: -0.078 dB, and E_{22}: -0.053 dB respectively.

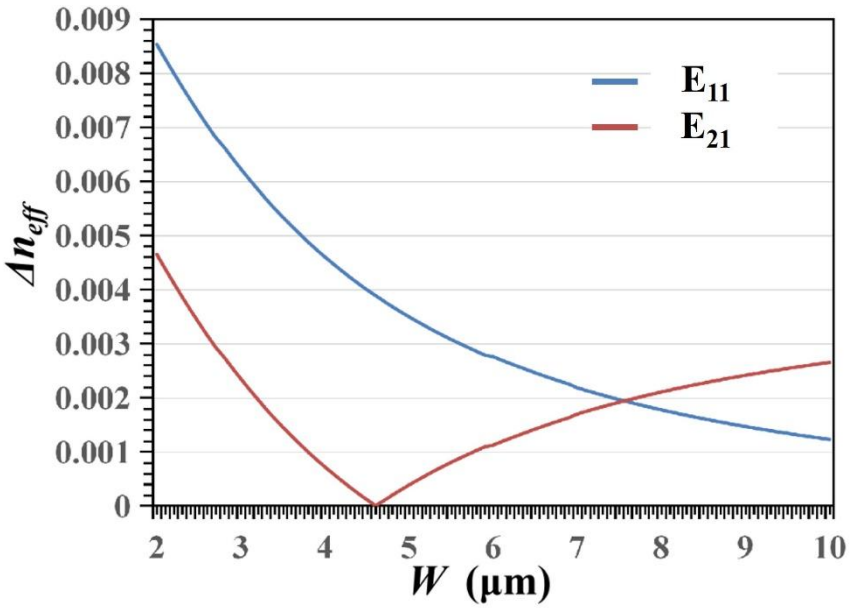

(a) Δn_{eff} of E_{11} and E_{21} mode for upper layer.

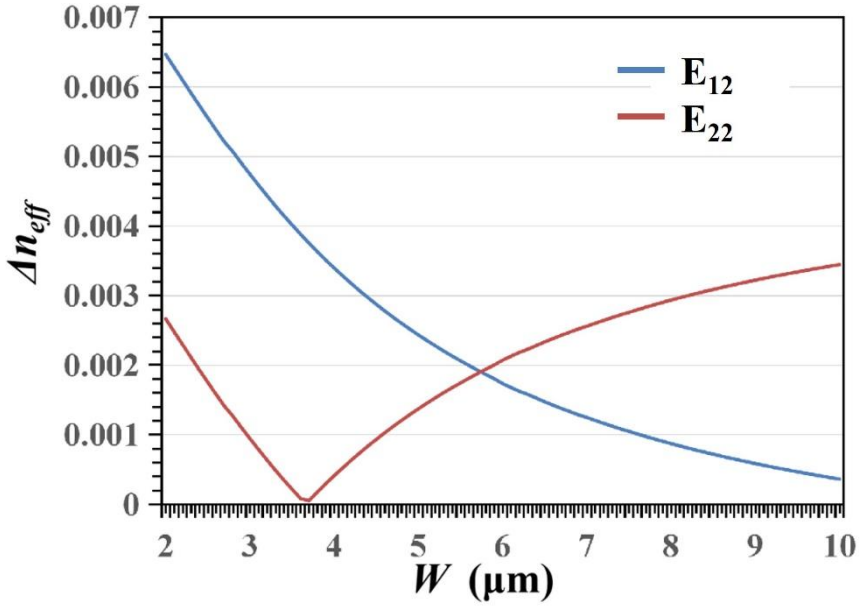

(b) Δn_{eff} of E_{12} and E_{22} mode for lower layer.

Figure 3.3 Relationship between the widths of each single-mode port and Δn_{eff} of each desired mode.

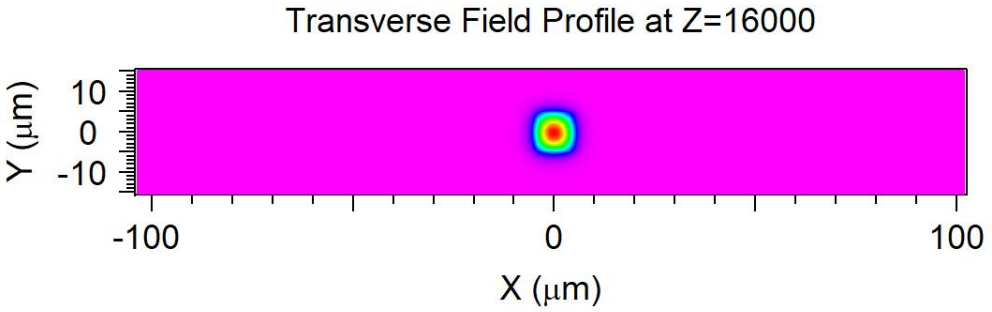

(a) Input from Port1.

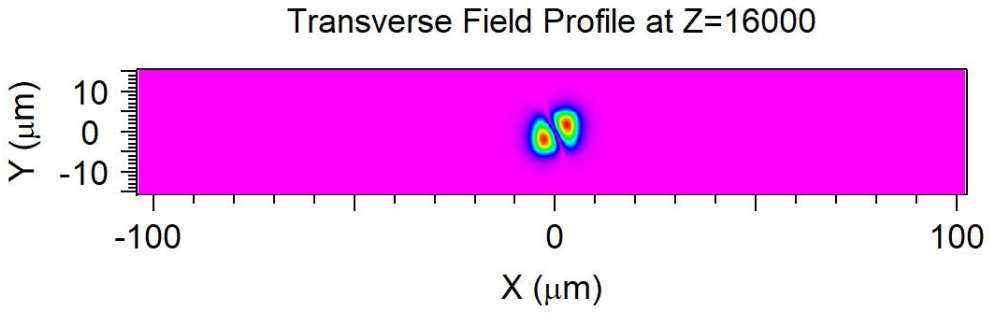

(b) Input from Port2.

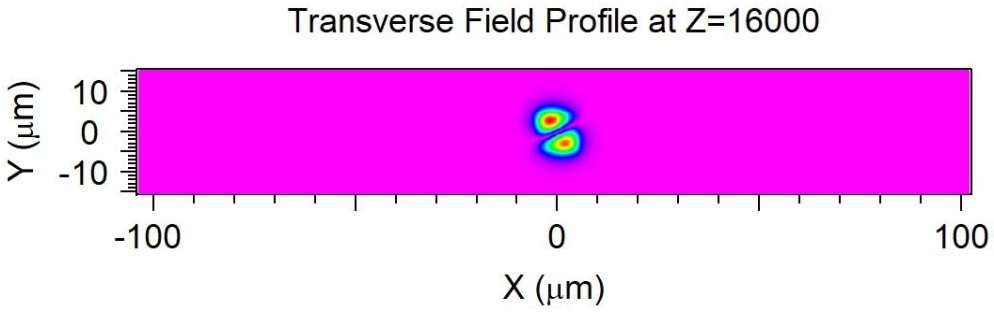

(c) Input from Port3.

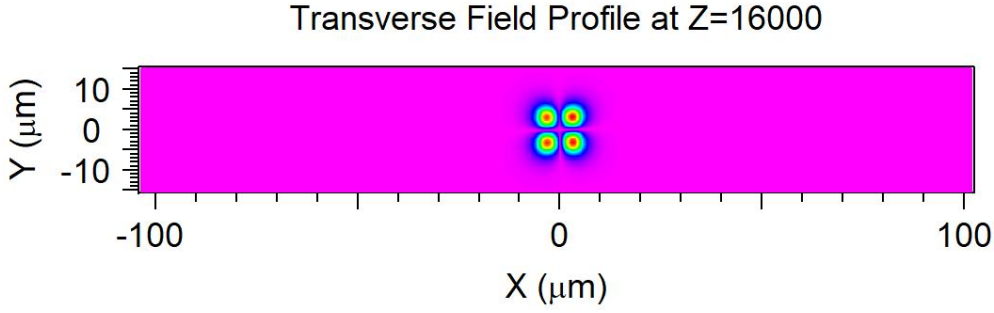

(d) Input from Port4.

Figure 3.4 Electric field distribution at the multi-mode output port.

Chapter 4 Photonic lantern 6-mode selective MUX/DMUX

4.1 Preface

It has been reported that the number of modes of a PLC-type mode multiplexer can be expanded to 6 modes by combining a directional coupler, a mode rotor, and a taper waveguide [17]. As the number of modes increases, the structure of the directional coupler type will become very complicated, and the device volume will increase greatly. In this study, we propose a 6-mode-selective photonic lantern mode multiplexer based on PLC, which can realize E_{11}, E_{21}, E_{12}, E_{22}, E_{31} and E_{13} 6-mode multiplexing with high selectivity. Then, we use the BPM to calculate and verify its performance.

4.2 Structural design of PLC photonic lantern 6-mode MUX

Figures 4.1 (a) and (b) show the 3D structure of the entire device and XY cross-sectional structure of the multi-mode output port of the 6-mode-selective photonic lantern mode multiplexer, respectively. It has a two-layer PLC structure in which six S-bend single-mode rectangular waveguides are close to each other, combined into a multi-mode waveguide. The refractive index of the silica cladding is assumed to be 1.444. The relative refractive index difference is $\Delta = 1.0$ %.

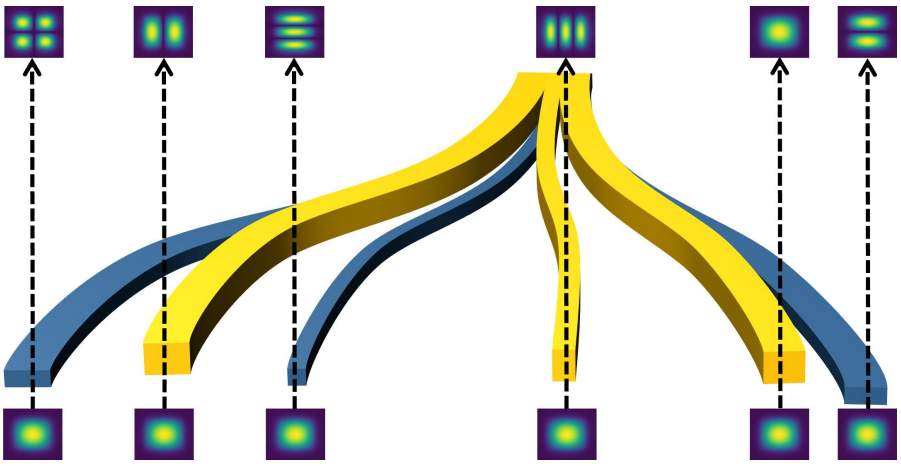

(a) 3D structure of the entire device.

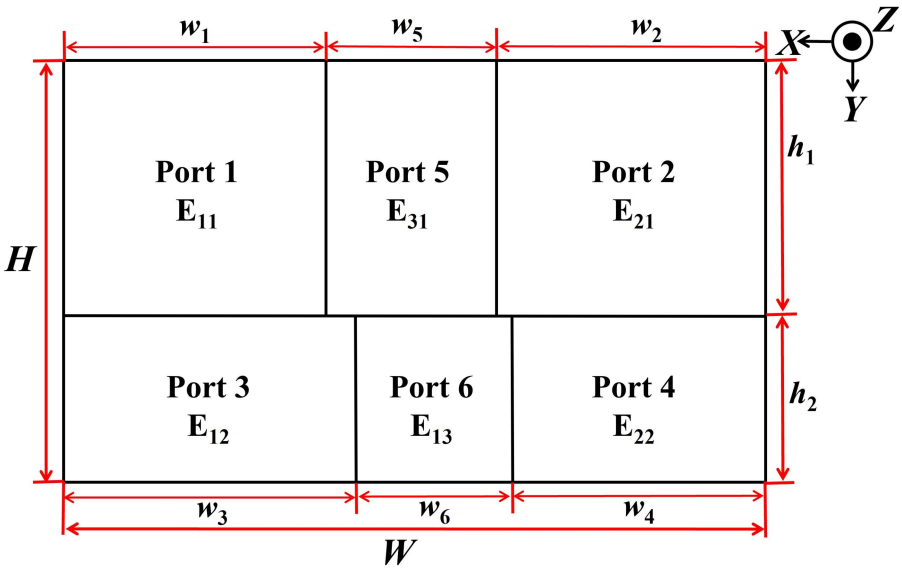

(b) XY cross-sectional structure of the multi-mode output port.

Figure 4.1 Structure of the 6-mode-selective photonic lantern MUX.

In order to let the multi-mode output port support six modes, first, we calculated the waveguide width dependency of the effective refractive index n_{eff} of each mode in a multi-mode waveguide when $W = H$, at the wavelength 1550 nm, which is shown in Fig. 4.2 (a). Around the near cutoff region (W = 8.7 ~ 9.5 μm), the highest-order mode (LP_{02}-like mode) corresponding to mode6 in Fig. 4.2 (a) will not guide well due to the low n_{eff}. It can be seen from Fig. 4.2 (a) that when H and W = 10 μm, 6 modes can be supported with enough large n_{eff} of mode6, and thus we focus on the vicinity of this parameter. To facilitate the adiabatic transport of modes for the purpose of mode selectivity, the sizes and n_{eff} of each branch waveguide should be sufficiently different to avoid the degeneracy of output port

modes. It can be seen from Fig. 4.2 (a) that when $W = H$, some modes had nearly equal n_{eff}, which will adversely affect the mode selection design. Figure 4.2 (b) shows the waveguide width dependency of the n_{eff} when fixed to H = 10 μm in height at the wavelength 1550 nm. According to Fig. 4.2 (b), a multi-mode waveguide size of H = 10 μm and W = 12 μm was chosen for subsequent simulations. At these dimensions, 8 modes can be supported by the waveguide but the n_{eff} of each mode is sufficiently separated to avoid mode degeneracy. This was considered more important than cutting off higher-order modes.

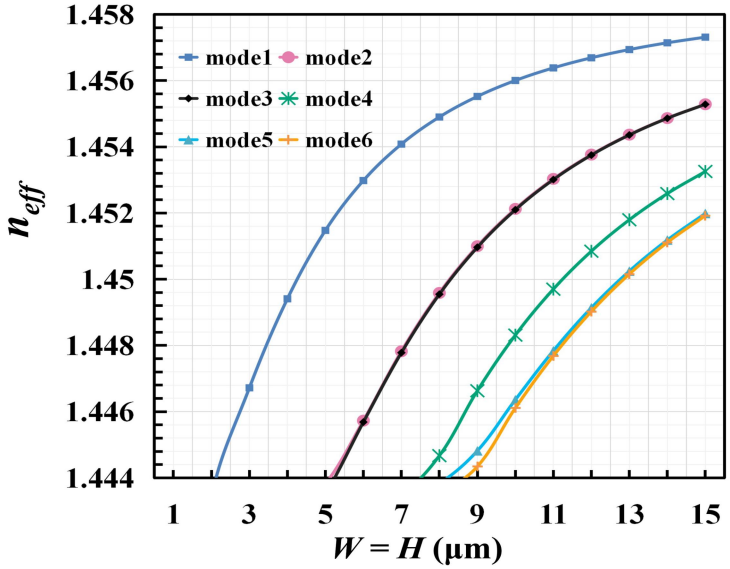

(a) In the case of $W = H$.

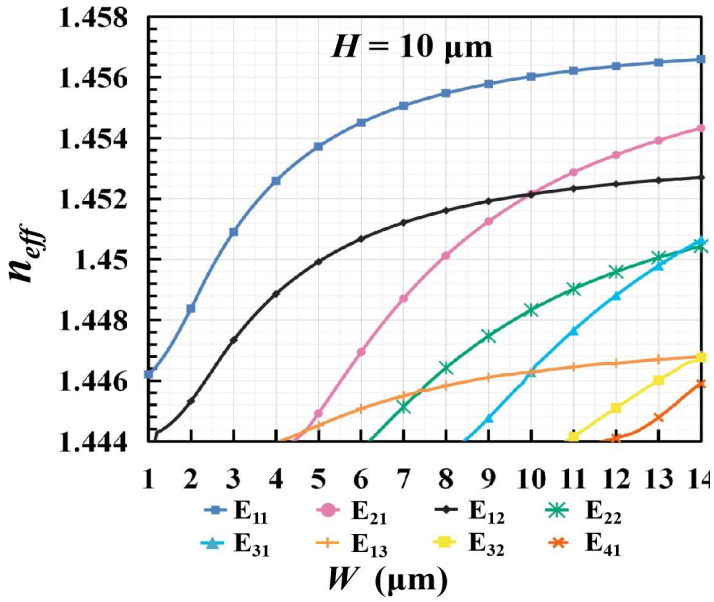

(b) In the case of H = 10 μm.

Figure 4.2 Waveguide width dependency of the n_{eff} of each mode.

As we mentioned before, to facilitate the mode selectivity, the sizes of each branch waveguide should be sufficiently different (including the height of each layer and the width of each branch waveguide). It has been confirmed that in a similar configuration, a higher transmission can be obtained when the layer height ratio of the two layers is about 0.65:0.35 [27]. Hence, we make the heights of the two layers different and set them to h_1 = 6.5 μm and h_2 = 3.5 μm.

Figures 4.3(a) and (b) show the relationship between the widths of each single-mode port w_i (i = 1~5) and Δn_{eff} of each desired mode. We found that as the waveguide height decreases, the waveguide width, at which the Δn_{eff} becomes minimum for each mode, gradually shifts to the right along the x-axis, which means that increasing the waveguide height can save the waveguide widths needed to excite each mode. To consider the allocation of six ports to six E_{ij} modes, it is effective to confirm the order of vertical field distribution. Among six modes, E_{11}, E_{21}, and E_{31} modes are the lowest order modes for the vertical axis. Therefore, these modes (E_{11}, E_{21}, and E_{31}) are allocated to the layer of h_1 = 6.5 μm, and the left three modes (E_{12}, E_{22}, and E_{13}) are allocated to the other layer of h_2 = 3.5 μm. Since E_{13} and E_{31} modes tend to radiate in the curved waveguide, we let these modes locate at the center of the horizontal axis.

The setting of other parameters (waveguide width of each branch waveguide) follows the following rules. The Δn_{eff} is only a rough representation of the mode matching between the branch waveguides and the multimode output port, so we selected the waveguide width parameters corresponding to the rule of Δn_{eff} = 0 only for the initial structure. Since it is difficult to excite the higher-order modes, such as E_{31} and E_{13} modes, we gave priority to satisfy the requirement that Δn_{eff} of the E_{13} mode in the lower layer and the E_{31} mode in the upper layer are as close to 0 as possible in the initial structure designing. Next, other modes are satisfied according to their n_{eff} from low to high. However, for example, due to the limitation of the overall waveguide width, E_{11} and E_{21} modes in the upper layer cannot fully meet the requirement that Δn_{eff} is close to 0, but because these modes are very easy to excite, these two lower-order modes can be excited as long as the waveguide width of the E_{11} mode is as large as that of the E_{21} mode.

The parameters should be carefully selected while reflecting the feedback of device characteristics such as transmissions shown later. After setting the

parameters of the initial structure, we optimized the structure by scanning the waveguide widths of each branch waveguide in a small range. The optimized parameters are determined as shown in Table 4.1. It can be seen from Table 4.1, that after optimization, the Δn_{eff} corresponding to each mode is not 0.

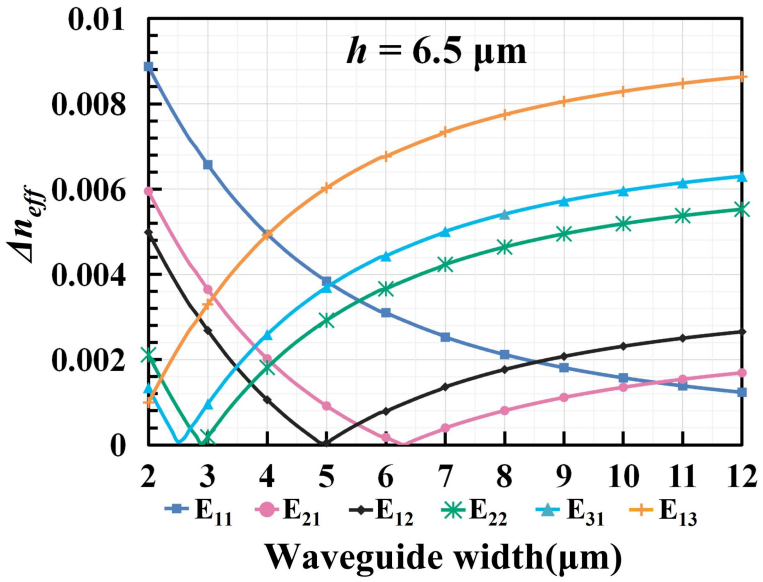

(a) Δn_{eff} of the upper layer.

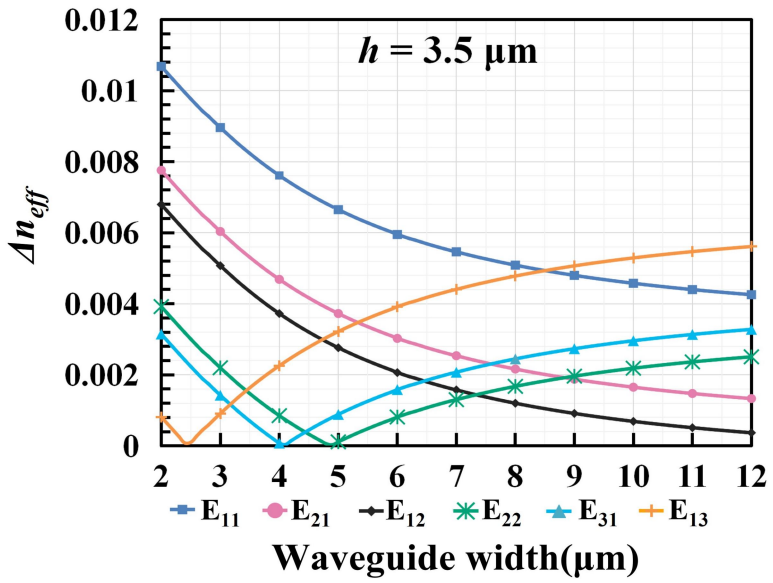

(b) Δn_{eff} of the upper layer.

Figure 4.3 Relationship between the widths of each single-mode port and Δn_{eff} of each desired mode.

Table 4.1 Optimized parameters of each branch waveguide an Δn_{eff} of each mode.

Upper layer h_1 = 6.5 μm			Lower layer h_3 = 3.5 μm		
Port (Mode)	Width (μm)	Δn_{eff}	Port (Mode)	Width (μm)	Δn_{eff}
Port1 (E_{11})	5.5 (w_1)	0.0034	Port3 (E_{12})	5.3 (w_3)	0.0025
Port2 (E_{21})	4.0 (w_2)	0.0020	Port4 (E_{22})	4.7 (w_4)	0.0002
Port5 (E_{31})	2.5 (w_5)	0.0001	Port6 (E_{13})	2.0 (w_6)	0.008

Figures 4.4 (a) and (b) show the XZ cross-section structure of the upper and lower layers of the 6-mode photonic lantern, respectively (Figs. 4.4 (a) and (b) are not to scale, the actual waveguides will not change in width when bent). In order to further optimize the device, we calculated the relationship between the transmission of each mode, the overall length L, and the distance between each single-mode port, D_i (D_1, D_2, D_3, D_4, D_5, and D_6 correspond to E_{11}, E_{21}, E_{12}, E_{22}, E_{31}, and E_{13} mode in Fig. 4.6, respectively), as shown in Figs. 4.5 and 4.6, which is calculated by the BPM. First, we discussed the L-dependency of transmission under the initial D_i condition (initial D_i is based on adiabatic transmission to minimize the energy exchange between the branch waveguides in the input part should be set large enough, in this case, initial D_i are determined as $D_1 = D_2 = 30$ μm, $D_3 = D_4 = 50$ μm, $D_5 = D_6 = 10$ μm). As seen from Fig. 4.5, because the E_{13} mode has the lowest effective refractive index and is too close to the higher-order mode when the total length L of the device increases, the E_{13} mode tends to couple to the higher-order E_{32} mode (We found that there is a correspondence between the E_{13} and the E_{32} modes due to the similar n_{eff}, the mode of Port6 excitation will be exchanged between the E_{13} and the E_{32} modes as L changes, which will be discussed in detail in Fig. 5.6 of section 5.2 Chapter 5). But if the device length L is controlled at 15 mm, the E_{13} mode with higher transmission can be obtained even without cutting off the higher-order mode. From Fig. 4.6, D_i has a smaller effect on the transmission when $D_i < 25$ μm. However, when the distance D_i is too

large, the high-order modes, such as E_{31} and E_{13} modes, are greatly radiated. Hence D_5 and D_6 should be set to less than 25 μm. By carefully selecting D_i to maximize the transmission of each mode, D_i are determined as D_1 = 34.5 μm, D_2 = 38 μm, D_3 = 46.5 μm, D_4 = 46 μm, D_5 = 11.5 μm, and D_6 = 20.5 μm.

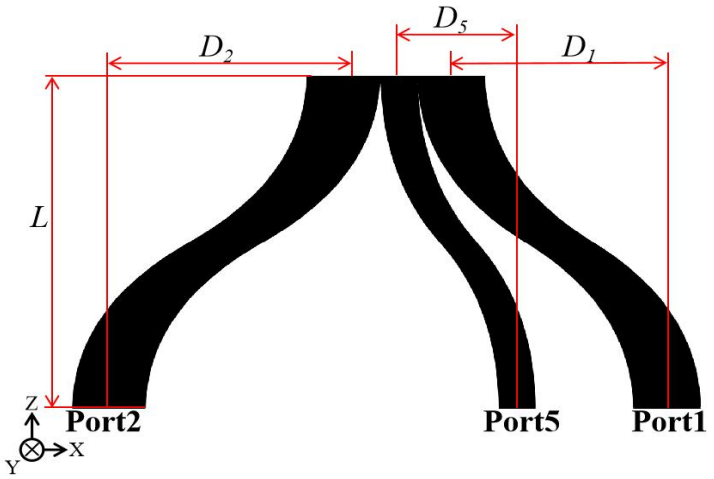

(a) Upper layer.

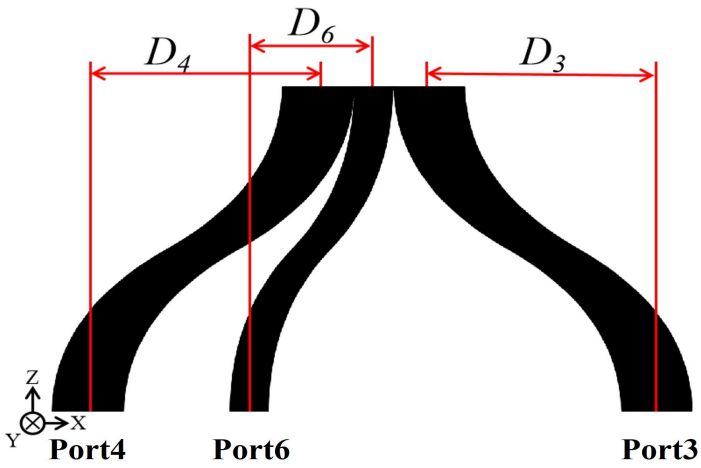

(b) Lower layer.

Figure 4.4 XZ cross-section structure of 6-mode photonic lantern.

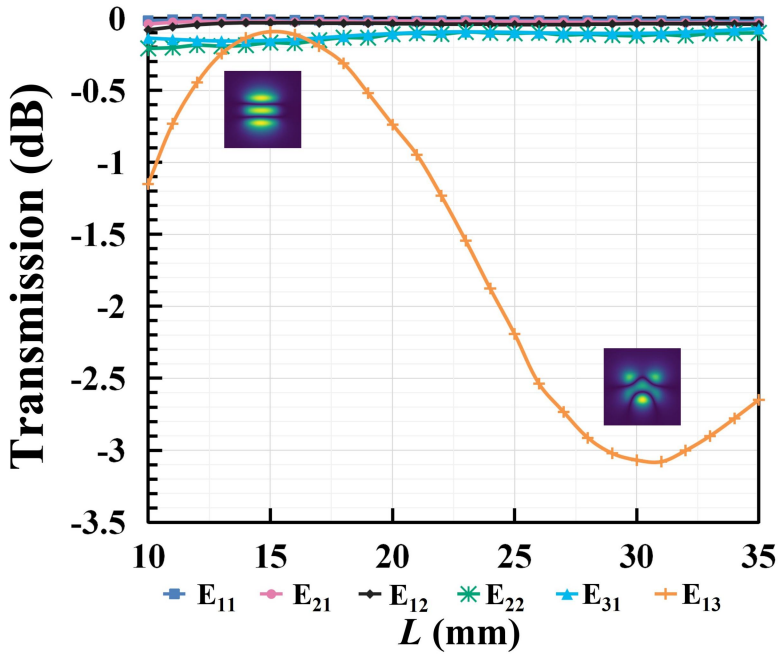

Figure 4.5 Relationship between the transmission and overall length L of the entire photonic lantern structure.

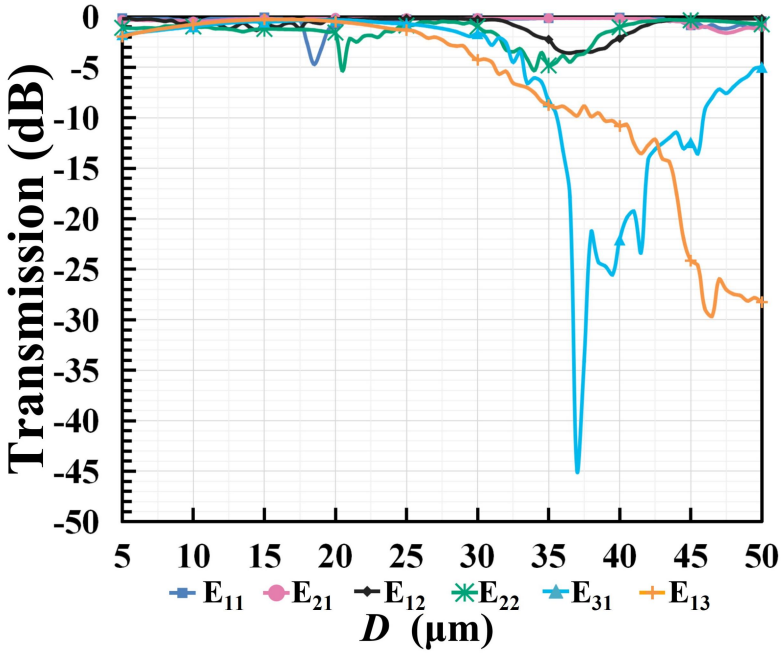

Figure 4.6 Relationship between the transmission of each mode and distance D_i between each single-mode port when L = 15 mm (D_1, D_2, D_3, D_4, D_5, and D_6 correspond to E_{11}, E_{21}, E_{12}, E_{22}, E_{31}, and E_{13} mode, respectively).

4.3 Performance evaluation of PLC photonic lantern 6-mode MUX/DMUX

Figures 4.7 (a)~(f) show the electric field distribution at the multi-mode output port when E_{11} mode is input from each single-mode port, respectively. It can be seen from Fig. 4.7 that this device has realized 6-mode multiplexing with high mode-selectivity.

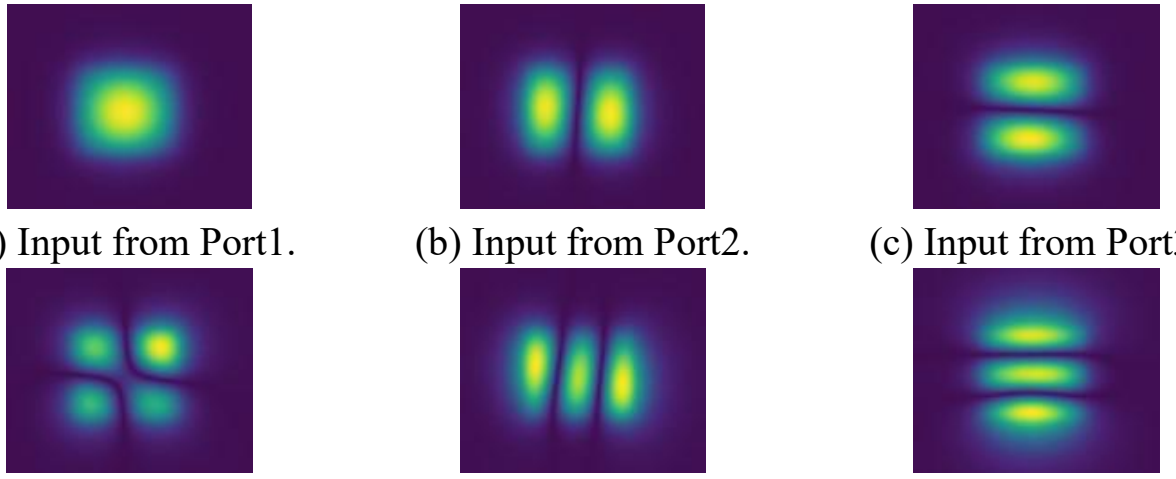

(a) Input from Port1. (b) Input from Port2. (c) Input from Port3.

(d) Input from Port4. (e) Input from Port5. (f) Input from Port6.

Figure 4.7 Electric field distribution at the multi-mode output port when E_{11} mode is input from each single-mode port.

Figures 4.8 (a)~(f) show the relationship between the transmission and wavelength of each mode of the output port when E_{11} mode is input from each single-mode port. The incomplete part of the E_{13} mode in Fig. 4.8 (b) indicates that the transmission of E_{13} mode is lower than -60 dB. It can be seen from Fig. 4.8 that the device has crosstalk between modes lower than −12.93 dB and low loss which is lower than 0.5 dB in the C+L band. The transmissions of each output desired E_{11}, E_{21}, E_{12}, E_{22}, E_{31}, and E_{13} modes are −0.01 dB, −0.02 dB, −0.03 dB, −0.19 dB, −0.18 dB, and −0.09 dB, respectively, and the MDL is 0.42 dB at the wavelength 1550 nm. Note that, the structural parameters (w_1, w_2, w_3, w_4, w_5, w_6, and D_i) are optimized to obtain high transmission and low MDL. Here, MDL is calculated as follows [20]. The transmission matrix is defined as

$$\boldsymbol{\phi}_{out} = \boldsymbol{T}\boldsymbol{\phi}_{in} \tag{4.1}$$

where $\boldsymbol{\phi}_{in}$ is input mode vector and $\boldsymbol{\phi}_{out}$ is output mode vector. $\boldsymbol{T}$ is the complex transmission matrix calculated by BPM. Theoretical MDL (in dB unit) is obtained by

$$\mathrm{MDL}=20\log_{10}\left(\frac{\lambda_{\max}}{\lambda_{\min}}\right) \tag{4.2}$$

where $\lambda_{\max}$ and $\lambda_{\min}$ are maximum and minimum singular values of $\boldsymbol{T}$ obtained by singular value decomposition.

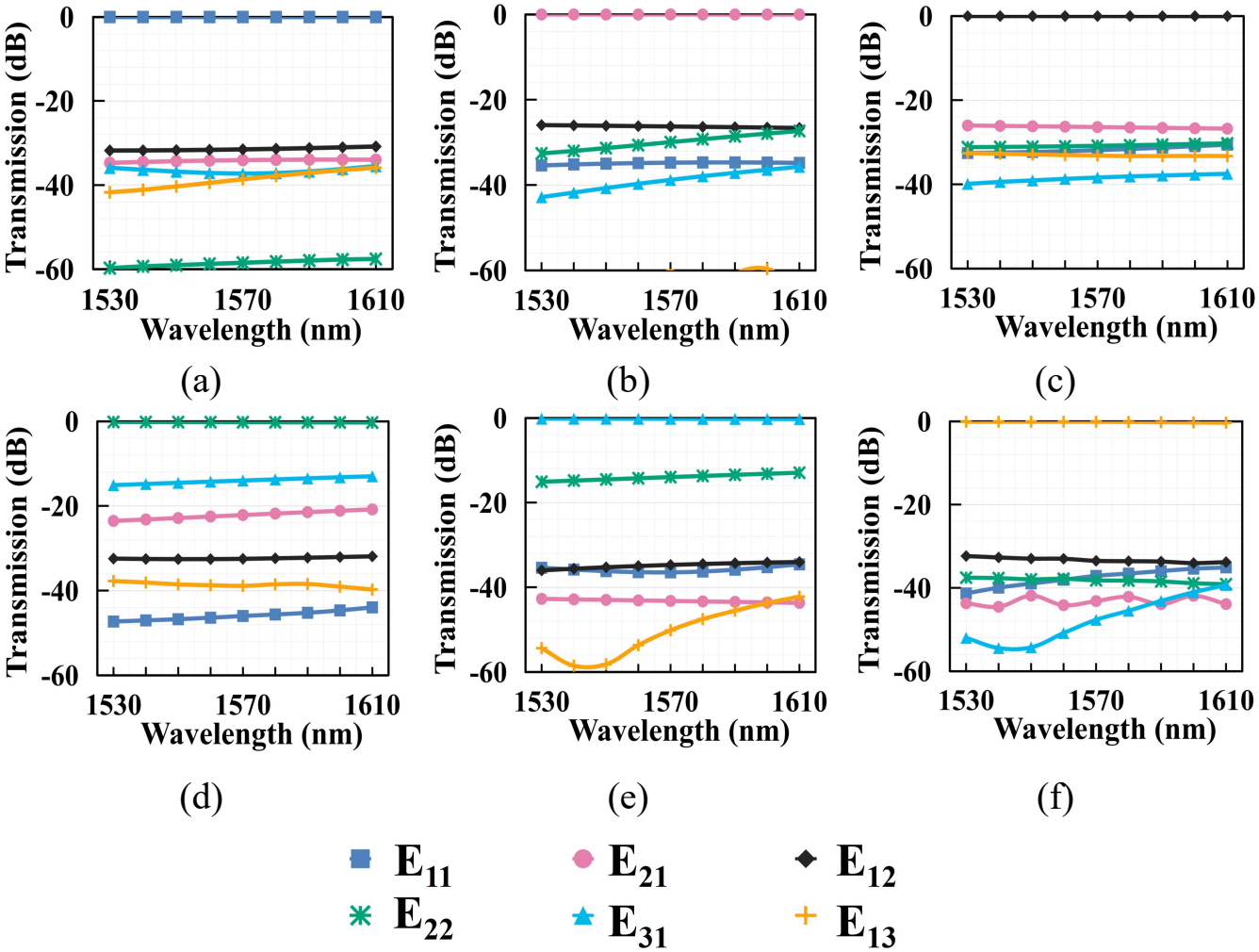

Figure 4.8 Relationship between the transmission and wavelength of each mode of the output port when E_{11} mode is input from (a) Port1, (b) Port2, (c) Port3, (d) Port4, (e) Port5, and (e) Port6, respectively.

We also calculated the case of demultiplexing. Figures 4.9 (a)~(f) show the electric field distribution of each branch waveguide port when E_{11}, E_{21}, E_{12}, E_{22}, E_{31}, and E_{13} modes are input from the multi-mode port, respectively. The transmissions at the wavelength 1550 nm of port1, port2, port3, port4, port5, and port6 are −0.02 dB, −0.04 dB, −0.03 dB, −0.18 dB, −0.15 dB, and −0.03 dB, respectively. And the crosstalk between single-mode ports is lower than -14.97 dB.

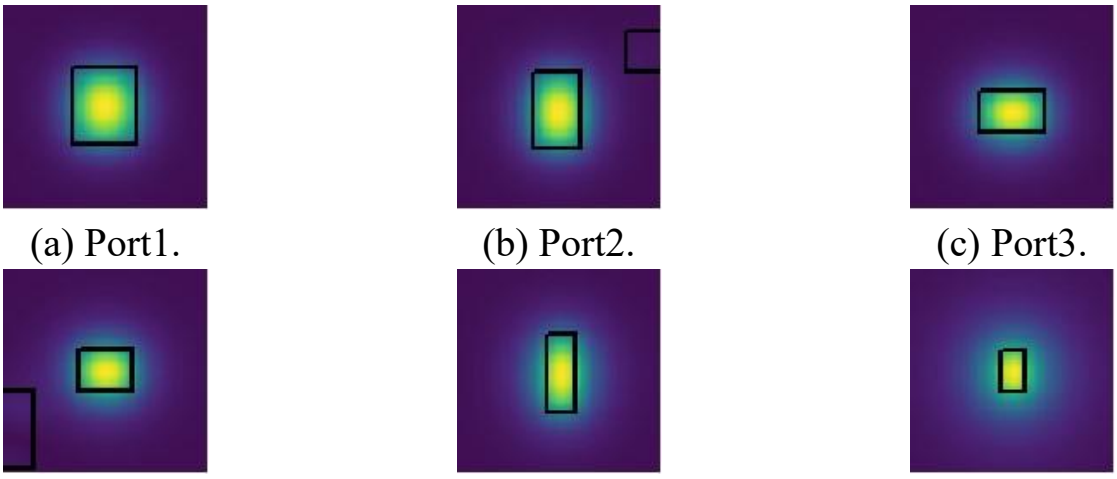

(a) Port1. (b) Port2. (c) Port3.

(d) Port4. (e) Port5. (f) Port6.

Figure 4.9 Electric field distribution of each single-mode port. Input modes are (a) E_{11}, (b) E_{21}, (c) E_{12}, (d) E_{22}, (e) E_{31}, and (f) E_{13}, respectively.

For manufacturing tolerances, the device height is easier to control in the case of PLC. So, we calculated the transmission of the 6-mode photonic lantern when the single-mode waveguide widths have structural errors of plus or minus 0.2 μm. Figures 4.10 (a)~(f) show the relationship between the transmission and single-mode waveguide widths structural errors Δw.

From Fig. 4.10, the transmission is greater than -1.99 dB, and the crosstalk between modes is lower than -5.75 dB. It can be seen from Figs. 4.10 (d) and (e) that since the n_{eff} of the E_{22} and E_{31} modes are relatively close, the two modes tend to degenerate when the width of each waveguide increases. In the terms of manufacturing tolerances, device performance is more likely to deteriorate as the waveguide widths increase.

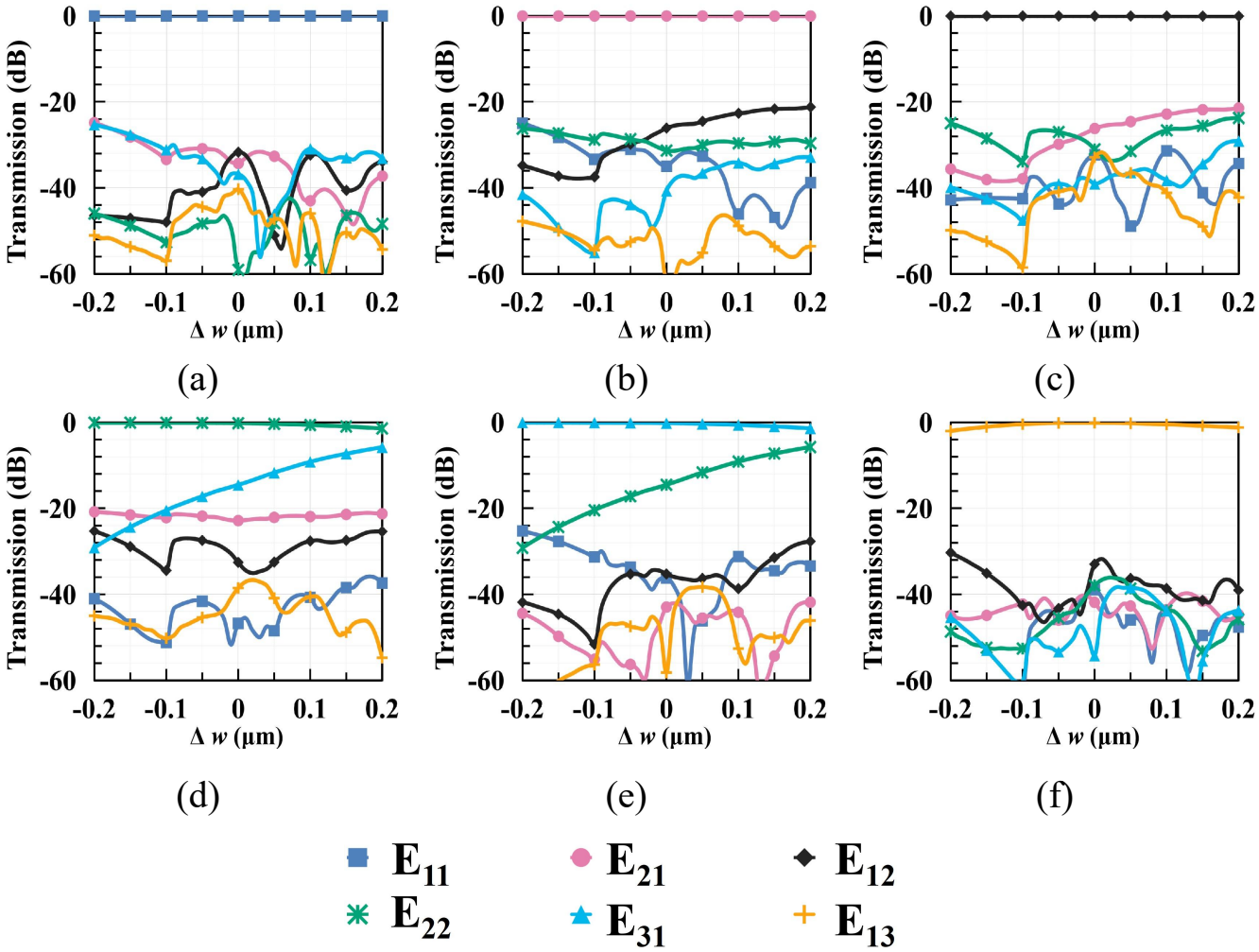

Figure 4.10 Relationship between the transmission and structural errors of branch-mode waveguide widths Δw when E_{11} mode is input from (a) Port1, (b) Port2, (c) Port3, (d) Port4, (e) Port5, and (e) Port6, respectively.

Chapter 5 Photonic lantern 10-mode selective MUX/DMUX

5.1 Preface

In this study, we propose a 10-mode-selective photonic lantern mode MUX based on PLC, which can realize E_{11}, E_{21}, E_{12}, E_{22}, E_{31}, E_{13}, E_{32}, E_{23}, E_{41}, and E_{14} 10-mode multiplexing with high selectivity. Then, we use the BPM to calculate and verify its performance. Since there is no previous research on 10-mode selective MUX, we encountered the problem of some unwanted high-order modes being excited that cannot be used for optical fiber transmission in this study. And that we can minimize the incentives of unwanted modes by setting optimized priorities.

5.2 Structural design of PLC photonic lantern 10-mode MUX

To increase the number of multiplexed modes to ten modes, we cannot directly add ports to a two-layer structure used in the 6-mode structure. This is because, to support ten modes, we must increase the width and height of the multi-mode waveguide output. However, as the width of the multi-mode waveguide increases, the width of ten branch waveguides needs to increase a lot to excite more higher-order modes. This will cause the width of the two-layer structure of the multi-mode output to be insufficient to accommodate ten branch waveguides. To solve this problem, we adopt a three-layer structure for the 10-mode photonic

lantern MUX. This structure has the same working principle as the two-layer structure. Figures 5.1 (a) and (b) show the 3D structure of the entire device and the XY cross-sectional structure of the multi-mode output port of the 10-mode photonic lantern MUX, respectively. It has a three-layer PLC structure in which ten S-bend branch rectangular waveguides are close to each other, combined into a multi-mode waveguide.

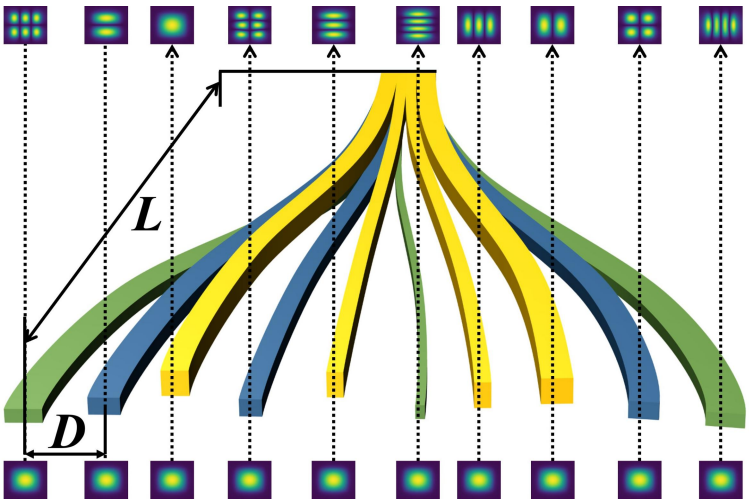

(a) 3D structure of the entire device.

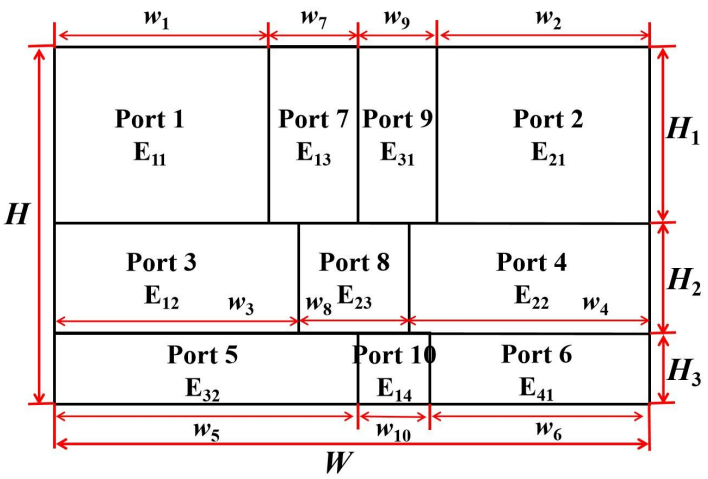

(b) XY cross-sectional structure of output port.

Figure 5.1 Structure of 10-mode-selective photonic lantern mode MUX.

The effective refractive index is the same as the previous subsection. Similar to the 6-mode multiplexer, the waveguide width dependency of n_{eff} of each mode in a waveguide is calculated when $W = H$, which shows in Fig. 5.2 (a). Figure 5.2 (b) shows the waveguide width dependency of n_{eff} when $H = 14$ μm. It is worth noting

that in this case, some modes (E_{33}, E_{42}) that cannot be used for fiber transmission can be excited, we want to excite the modes (E_{11}, E_{21}, E_{12}, E_{22}, E_{31}, E_{13}, E_{32}, E_{23}, E_{41}, and E_{14} modes) that can be used for fiber transmission. As we can see from Figs. 5.2 (a) and (b), because the mode degeneracy is prone to occur in the part where n_{eff} is close, and when the waveguide width is greater than 15 μm, the desired E_{14} mode can be easier to excite. To make the multi-mode port support desired ten modes, a multimode waveguide size of H = 14 μm and W = 17 μm was chosen for subsequent simulations. To avoid unnecessary energy exchange between the waveguides at the branch input ports, the distance between each branch waveguide should be large enough, set to D = 20 μm in the initial structure.

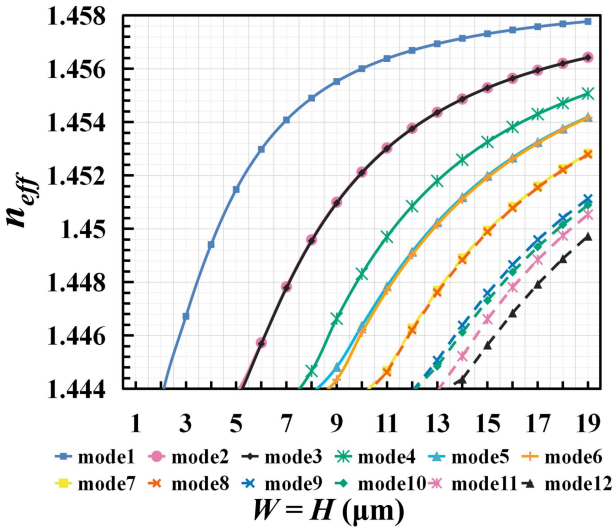

(a) In the case of $W = H$.

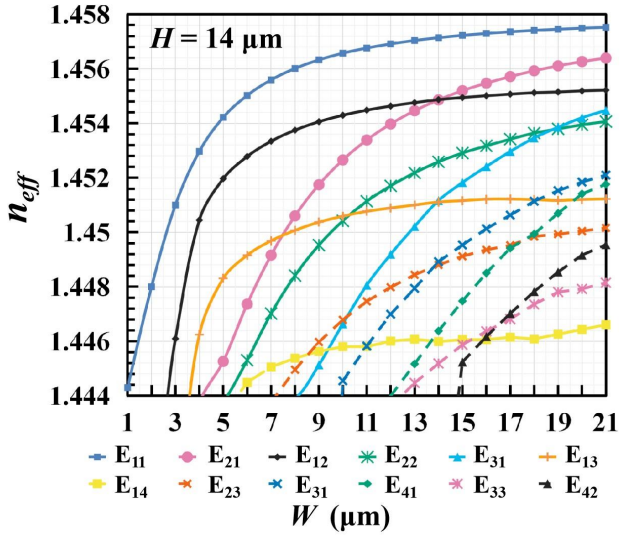

(b) In the case of H = 14 μm.

Figure 5.2 Waveguide width dependency of the n_{eff}.

It is worth noting that in this case, the E_{14} mode is not the n_{eff} ranked 10th mode. Therefore, in the 10-mode design, we must skip unwanted higher-order modes such as E_{42} and E_{33} to directly excite the mode E_{14} which has not been discussed in any previous related literature due to the further increase in the number of modes as shown in Fig. 5.3. We demonstrate the possibility to directly excite the target mode by skipping the unneeded modes using our design method.

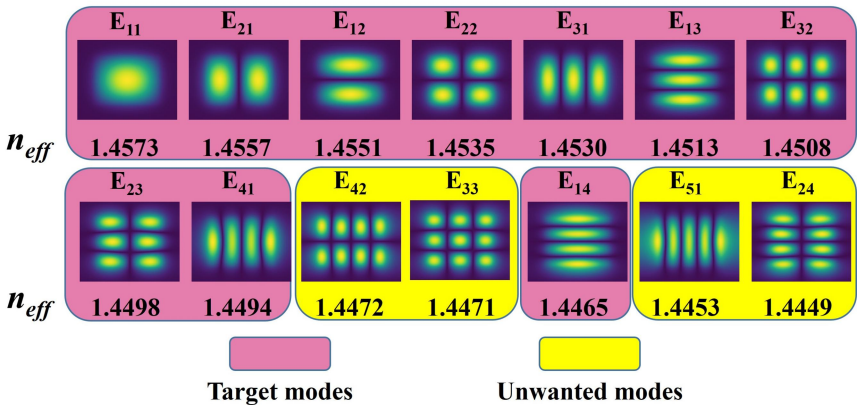

Figure 5.3 Modes supported by multimode output port when W = 17 μm and H = 14 μm.

The design method of this study is as follows. Firstly, select the height H_1, H_2, and H_3 of the initial structure of each layer appropriately according to the principle that the height of each layer should be as different as possible. At the same time, to prevent excessive radiation loss, the height of each layer should not be set too small. Secondly, in the same manner as the previous subsection, the parameters of each branch waveguide should be determined according to Δn_{eff}. Thirdly, optimize each parameter ($w_{1\sim8}$). We found that in the case when the overall waveguide width W is fixed, changing the waveguide width of any port will not only affect transmissions of the corresponding modes of this port and other ports in this layer but also affect the ports where the width of waveguide does not change in other layers. Therefore, when optimizing the waveguide width w_i of each port of each layer, we separated each layer, started from the third layer that is more difficult to excite, and optimized upwards to the upper layers one by one. After the optimization of the three layers is completed, the optimization of each layer is repeated according to device characteristics. Then optimize the heights of each

layer and the overall length L and repeat the above optimization steps according to device characteristics. Below we will show some representative optimization results and the parameters set according to the device characteristics.

Figures 5.4 (a), (b), and (c) show the relationship between the widths of each branch input port and Δn_{eff} of each desired mode (The heights of each layer h shown here are not initial parameters, but the result obtained after optimization. The optimization of the heights of each layer will be discussed in Fig. 5.5.). In the manner as the previous subsection, width parameters of each branch waveguide and Δn_{eff} of each mode have shown in Table 5.1. Based on adiabatic transmission to minimize the energy exchange between the branch waveguides in the input part, the distance between each branch waveguide D is determined as D = 20 μm.

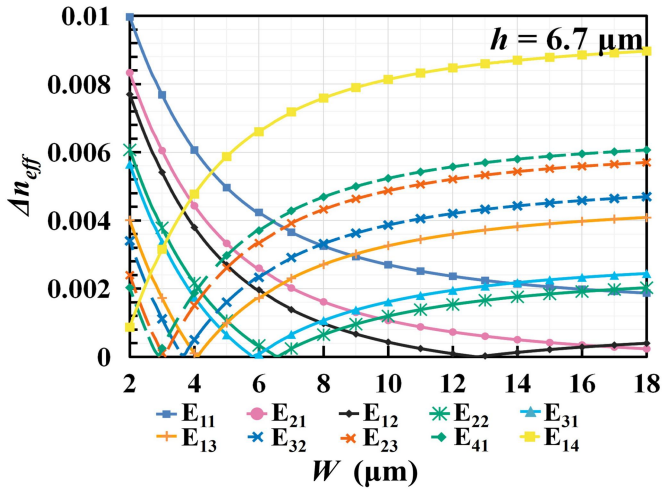

(a) Δn_{eff} of the upper layer.

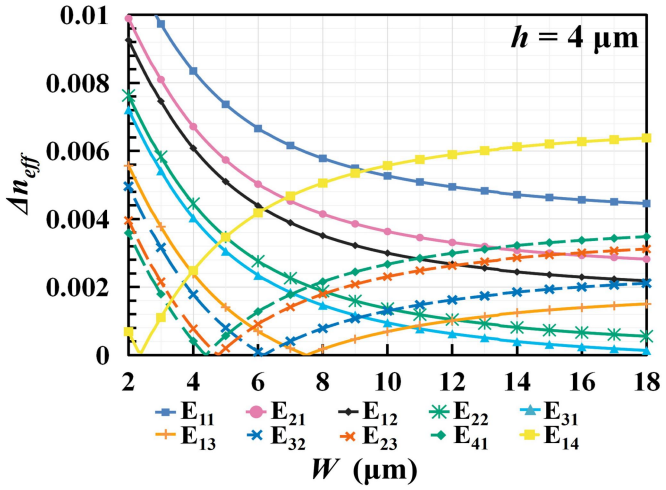

(b) Δn_{eff} of the middle layer.

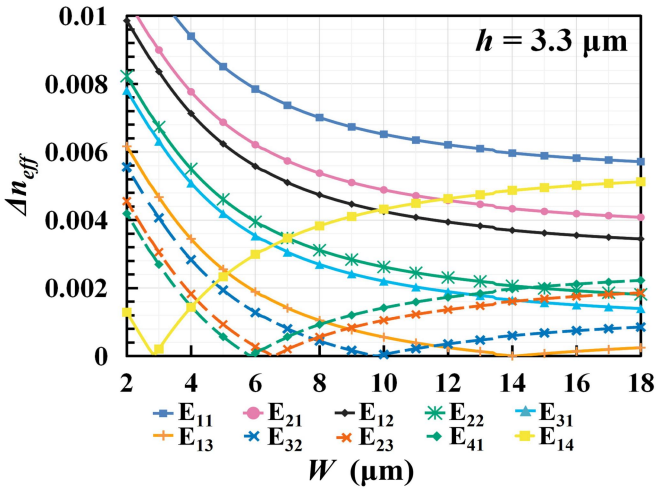

(c) Δn_{eff} of the lower layer.

Figure 5.4 Relationship between the widths of each branch waveguide port and Δn_{eff} of each desired mode.

Table 5.1 Width parameters of each branch waveguide and Δn_{eff} of each mode.

Upper layer $H_1 = 6.7$ μm			Middle layer $H_2 = 4$ μm			Lower layer $H_3 = 3.3$ μm		
mode	Δn_{eff}	Width (μm)	mode	Δn_{eff}	Width (μm)	mode	Δn_{eff}	Width (μm)
E_{11}	0.0041	6.0 (w_1)	E_{12}	0.0035	7.0 (w_3)	E_{32}	0.0000	7.6 (w_5)
E_{21}	0.0035	4.6 (w_2)	E_{22}	0.0025	5.8 (w_4)	E_{41}	0.0011	7.1 (w_6)
E_{31}	0.0029	3.1 (w_9)	E_{23}	0.0002	4.2 (w_8)	E_{14}	0.0005	2.3 (w_{10})
E_{13}	0.0010	3.3 (w_7)						

For the height of each layer H_1, H_2, and H_3, we calculated the relationship between the transmissions of each mode output at the multi-mode port and the height of each layer, as shown in Fig. 5.5. As can be seen from Fig. 5.5, E_{13} and E_{32} modes have higher transmission only in the small range enclosed by the black dotted line, we combined the transmission of other modes to select the height parameters of each layer at the X point mark to make the transmission of E_{13} and E_{32} modes as high as possible. The height of each layer is determined as $H_1 = 6.7$ μm, $H_2 = 4$ μm, and $H_3 = 3.3$ μm to increase the transmission of each mode.

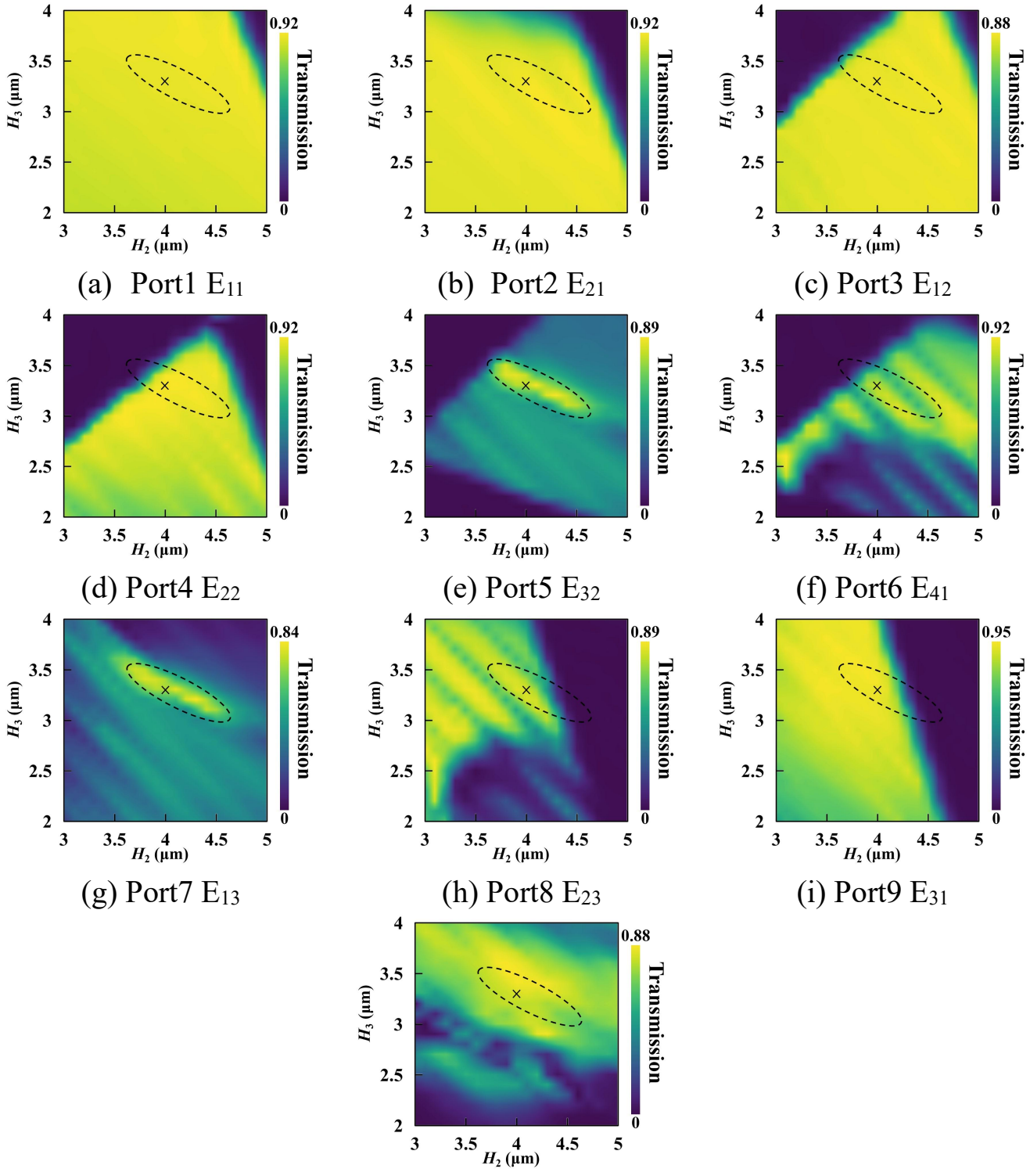

(a) Port1 E_{11} (b) Port2 E_{21} (c) Port3 E_{12}

(d) Port4 E_{22} (e) Port5 E_{32} (f) Port6 E_{41}

(g) Port7 E_{13} (h) Port8 E_{23} (i) Port9 E_{31}

(j) Port10 E_{14}.

Figure 5.5 Relationship between the transmissions of each output mode and heights of each output port.

To further optimize the device, we calculated the relationship between the transmission of each mode and the overall length *L*, as shown in Fig. 5.6. When

optimizing L, we found that because the n_{eff} of each high-order mode is relatively close, this leads to a correspondence between adjacent high-order modes like E_{13} and E_{32} modes as shown in Fig. 5.7, even if Δn_{eff} is as close to 0 as possible. This correspondence can also be observed between E_{23} and E_{41} modes. In other words, in two ports with corresponding higher-order modes, if one port excites one mode, the other port will excite the other mode certainly. For example, if we let Port5 excite the E_{32} mode, Port7 will excite the E_{13} mode certainly. The overall length is set to L = 28 mm according to Figs. 5.6 and 5.7 to obtain higher transmission for each mode.

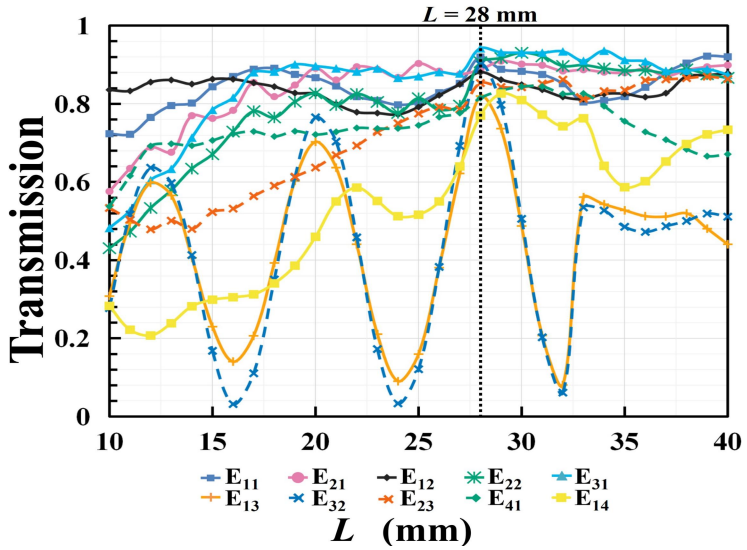

(a) Port5 excite E_{32} mode, Port7 excite E_{13} mode.

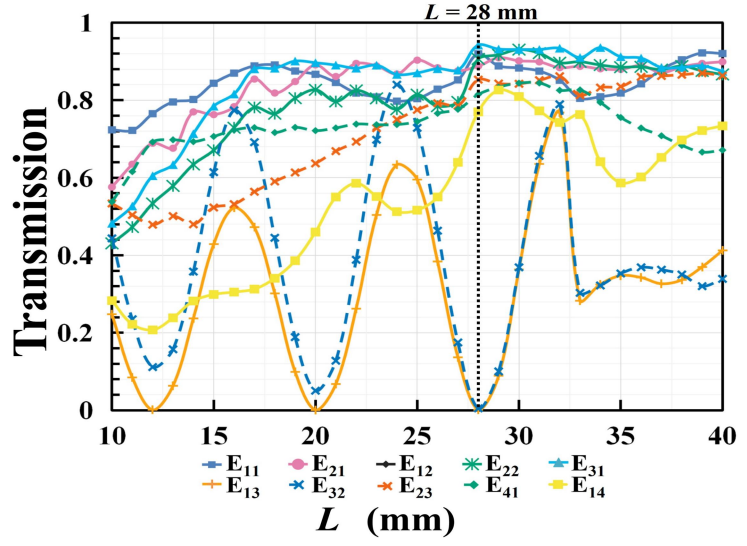

(b) Port5 excite E_{13} mode, Port7 excite E_{32} mode.

Figure 5.6 Relationship between the transmission of each mode and the overall length L.

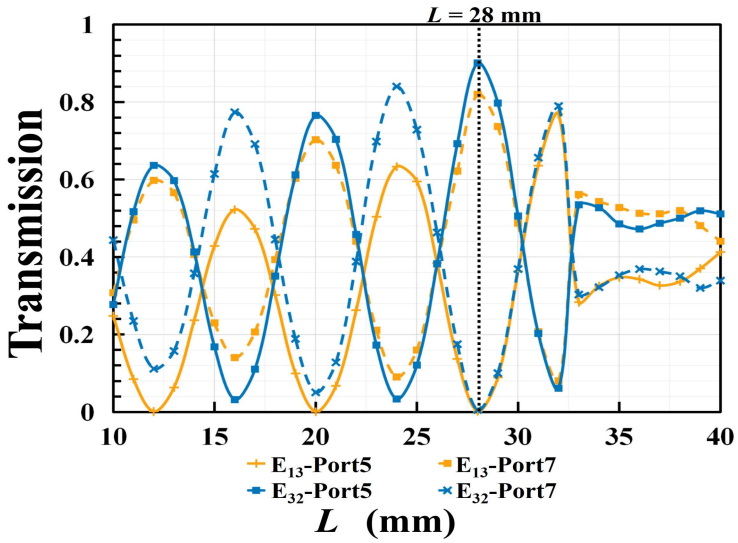

Figure 5.7 Correspondence between adjacent high-order modes (E_{13} and E_{32} modes) in Port5 and Port7.

5.3 Performance evaluation of PLC photonic lantern 10-mode MUX/DMUX

Figure. 5.8 shows the electric field distribution at the multi-mode output port when E_{11} mode is input from each branch waveguide input port, respectively. It can be seen from Fig. 5.8 that this device has realized ten-mode multiplexing. This also can verify that we can directly excite the required mode by optimizing the device and skipping some unnecessary modes.

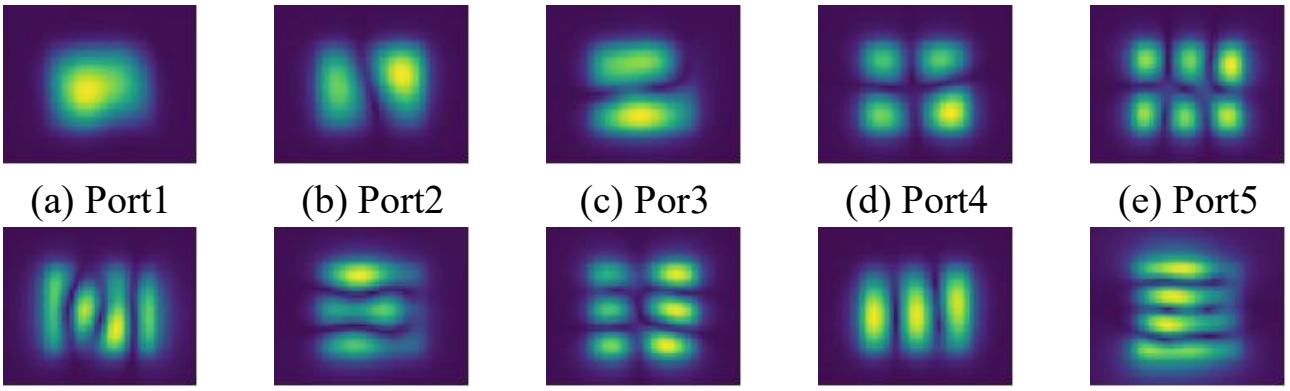

(a) Port1 (b) Port2 (c) Por3 (d) Port4 (e) Port5

(f) Port6 (g) Port7 (h) Port8 (i) Port9 (j) Port10

Figure 5.8 Electric field distribution at the multi-mode output port when E_{11} mode is input from each input port.

Figures. 5.9 (a)~(f) show the relationship between the transmission and wavelength of each mode of the output port when E_{11} mode is input from each branch waveguide port. According to Fig. 5.9, the transmissions of each output desired E_{11}, E_{21}, E_{12}, E_{22}, E_{31}, E_{13}, E_{32}, E_{23}, E_{41}, and E_{14} modes are −0.36 dB, −0.51 dB, −0.55 dB, −0.42 dB, −0.26 dB, −0.86 dB, −0.45 dB, −0.69 dB, −0.89 dB, and −1.15 dB, respectively, and the MDL is 1.43 dB at the wavelength 1550 nm. We can see that the structure can achieve ten-mode multiplexing in which the crosstalk between the main desired mode and the other modes is less than −10.97 dB when the wavelength is 1550 nm, and less than -8.74 dB in the C-band. In the 10-mode design, to reduce the size of the device, we chose smaller waveguide width and height as possible. We expect that this structure can obtain higher mode selectivity by relaxing the size limit of the waveguide.

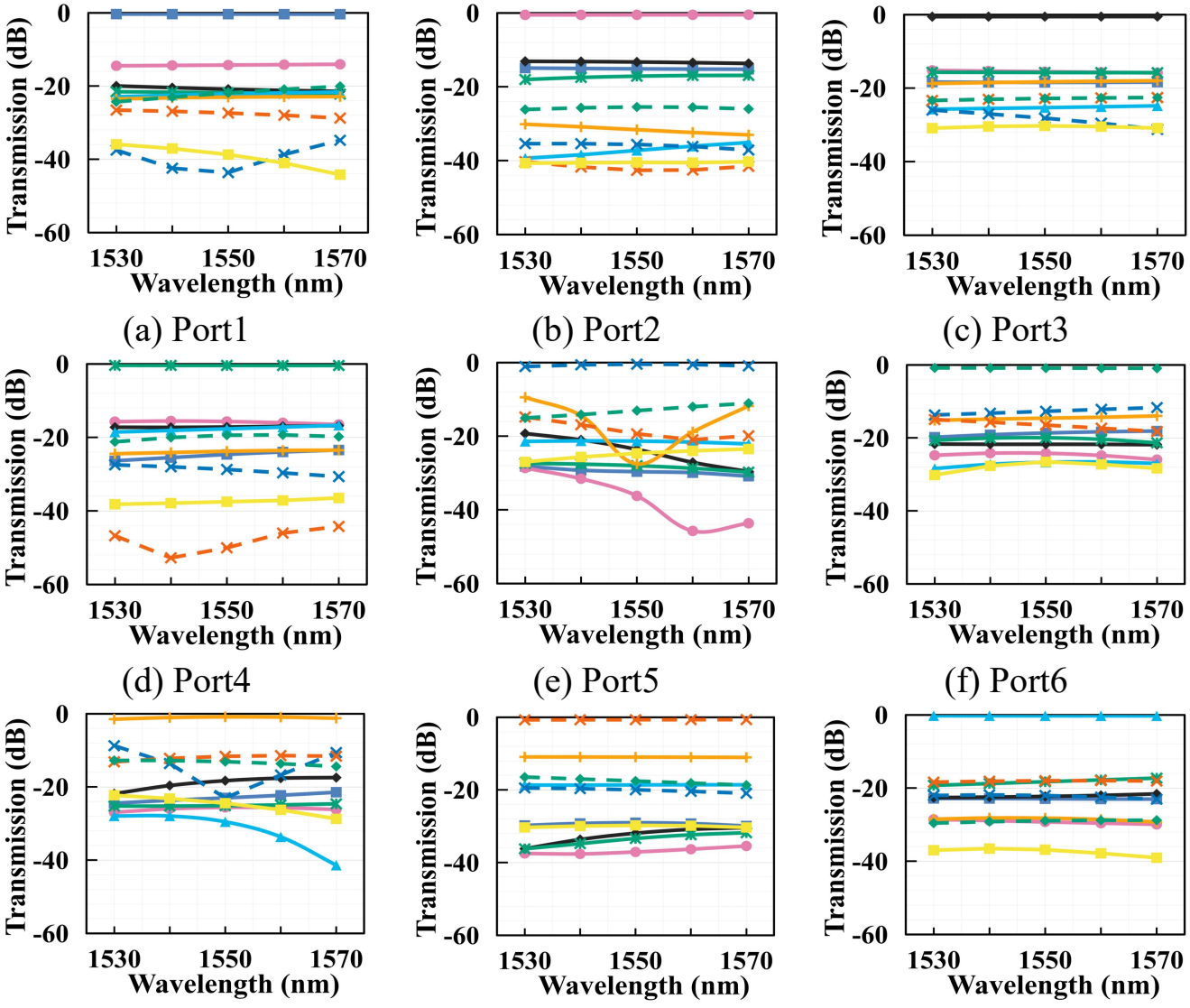

(a) Port1 (b) Port2 (c) Port3

(d) Port4 (e) Port5 (f) Port6

(g) Port7 (h) Port8 (i) Port9

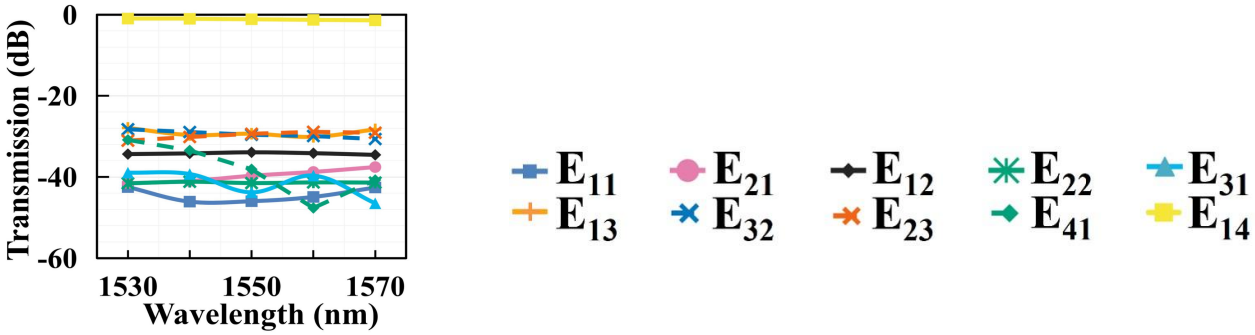

(j) Port10

Figure 5.9 Relationship between the transmission and wavelength of each mode of the output port when E_{11} mode is input from each input port.

We also calculated the case of demultiplexing. Figures 5.10 (a)~(f) show the electric field distributions of each branch waveguide port. The transmissions at the wavelength 1550 nm of Port1, Port2, Port3, Port4, Port5, Port6, Port7, Port8, Port9, and Port10, are −0.71 dB, −0.56 dB, −0.62 dB, −0.89 dB, −0.71 dB, −1.12 dB, −1.18 dB, −1.00 dB, −0.58 dB, and −1.14 dB, respectively. And the crosstalk between branch ports is lower than -8.99 dB.

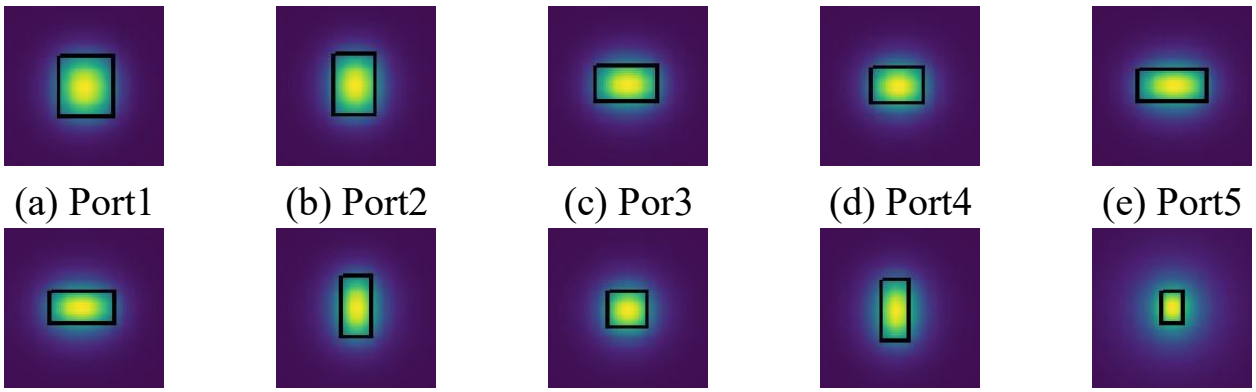

(a) Port1 (b) Port2 (c) Por3 (d) Port4 (e) Port5

(f) Port6 (g) Port7 (h) Port8 (i) Port9 (j) Port10

Figure 5.10 Electric field distribution of each branch waveguide port. Input modes are (a) E_{11}, (b) E_{21}, (c) E_{12}, (d) E_{22}, (e) E_{32}, (f) E_{41}, (g) E_{13}, (h) E_{23}, (i) E_{31}, and (j) E_{14}, respectively.

For manufacturing tolerances, we calculated the transmission of the 10-mode photonic lantern when the branch waveguide widths have structural errors of plus or minus 0.2 μm, as shown in Figs. 5.11 (a)~(j). It can be seen from Figs. 5.11(e) and (g) that since the n_{eff} of the E_{13} and E_{32} modes are relatively close, the device

performance is very easily affected by the width of the waveguide. As mentioned earlier, there is a correspondence between the E_{13} and E_{32} modes in Ports 5 and 7. Even though, the 10-mode photonic lantern can be used as a mode scrambler [19], since required modes are excited under the presence of waveguide width change.

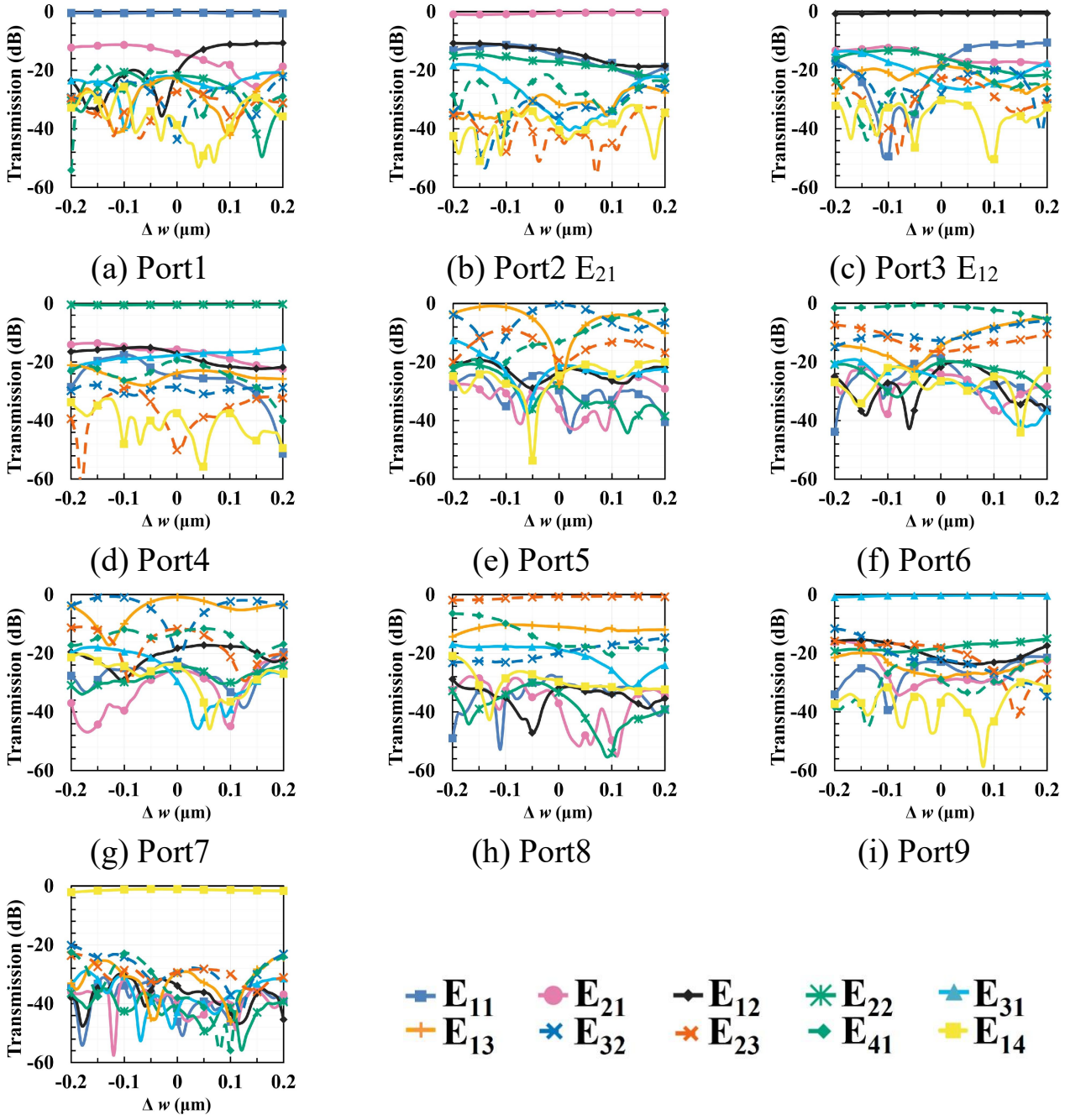

Figure 5.11 Relationship between the transmission and structural errors of branch-mode waveguide widths Δw when E_{11} mode is input from each input port.

Chapter 6 PLC E31, E13 taper mode converters using FAQUAD method

6.1 Preface

In the past few years, we have proposed two types of ADC structures and photonic lantern structures, respectively [17], [21]. In the ADC-based 6-mode MUX, to achieve 6-mode multiplexing, a linear taper waveguide structure is utilized to realize the conversion from the E_{31} mode to the E_{13} mode, enabling the excitation of the E_{13} mode [17]. In the 6-mode MUX based on the photonic lantern structure, the output waveguide is rectangular in shape (which means that the waveguide width W and waveguide H are not equal), resulting in waveguide modes being emitted [21]. To facilitate better connectivity with optical fibers, it is necessary to convert the waveguide modes into fiber-like waveguide modes as shown in Fig. 3.1 of section 3.2 Chapter 3. This can be achieved by using a taper waveguide structure to transition from a rectangular waveguide ($W \neq H$) to a square waveguide ($W = H$) [51].

The previous PLC E_{31} and E_{13} mode converters used linear taper structures to fulfill the adiabatic coupling condition and achieve a high mode conversion efficiency, which requires long taper lengths. In this study, we used the FAQUAD method to design the PLC E_{31}-E_{13} taper mode converter suitable for the 6-mode ADC mode MUX, and the PLC E-LP taper mode converter suitable for the PLC photonic lantern 6-mode MUX, and the PLC E-LP taper mode converter suitable for PLC photonic lantern 10-mode MUX.

6.2 The principles of FAQUAD method

Previously, such taper waveguides were constructed using a linear taper or a multi-stage linear taper structure [17]. However, to achieve a gradual adiabatic coupling process, an extremely long taper length L was required, resulting in a significant increase in the device size.

The adiabatic mode conversion process in optical waveguide devices requires the following relationship

$$c(z) \equiv \left| \frac{\iint \left[\mathbf{E}_m \times \frac{\partial}{\partial z} \mathbf{H}_n^* \right] \cdot \boldsymbol{i}_z dxdy}{\beta_m - \beta_n} \right| \ll 1 . \tag{6.1}$$

Here, $c(z)$ is called the adiabaticity parameter. $\mathbf{E}_m$ and $\mathbf{H}_n$ represent the electric field distribution of the mth eigenmode and the magnetic field distribution of the nth eigenmode of the waveguide, respectively. β_m and β_n represent the propagation constants of the mth and nth modes, respectively.

The FAQUAD method accelerates the adiabatic coupling evolution process by controlling the adiabatic parameters to achieve a uniform distribution during the adiabatic coupling process. The key to the FAQUAD method is to achieve a uniform distribution of the adiabatic parameter along the z-direction by fixing the adiabaticity parameter in Eq. (6.1) to a constant value ε. In other words, according to the following procedure [31], we should find $z_{\text{opt}}(W)$ satisfying $c(z) = \varepsilon$, where ε is a certain constant value. At the beginning, using the chain rule for z and W, Eq. (6.1) is rewritten as

$$c(z) = \left| \frac{dW}{dz} \right| \cdot c_W(W) = \varepsilon \tag{6.2}$$

$$c_W(W) = \left| \frac{\iint \left[\mathbf{E}_m \times \frac{\partial}{\partial W} \mathbf{H}_n^* \right] \cdot \boldsymbol{i}_z dxdy}{\beta_m - \beta_n} \right| . \tag{6.3}$$

Since dW/dz is a constant in the linear taper waveguide, the adiabatic parameter

for the linear taper waveguide as a function of W can be expressed as

$$c_{\mathrm{lin}}\left(W\right)=\frac{\left|W_{\mathrm{out}}-W_{\mathrm{in}}\right|}{L}c_{W}\left(W\right). \tag{6.4}$$

Substituting Eq. (6.2) into Eq. (6.4) and inverting z and W, we can obtain the following relationship.

$$\frac{dz}{dW}=\frac{L}{W_{\mathrm{out}}-W_{\mathrm{in}}}\cdot\frac{c_{\mathrm{lin}}\left(W\right)}{\varepsilon}, \tag{6.5}$$

noting that the sign of dz/dw should be coincident with that of $W_{\mathrm{out}}-W_{\mathrm{in}}$. Integrating Eq. (6.5) with the condition of $z(W_{\mathrm{in}}) = 0$, we can obtain $z_{\mathrm{opt}}(W)$ as

$$z_{\mathrm{opt}}\left(W\right)=\frac{L}{W_{\mathrm{out}}-W_{\mathrm{in}}}\frac{1}{\varepsilon}\int_{W_{\mathrm{in}}}^{W}c_{\mathrm{lin}}\left(t\right)dt, \tag{6.6}$$

where t is an integration variable. Noting that the length of the optimized taper given by z_{opt}, which is $L_{\mathrm{opt}} = z_{\mathrm{opt}}\ (W_{\mathrm{out}})$, depends on ε. If we fix ε to satisfy $L_{\mathrm{opt}} = L$, ε is derived as

$$\varepsilon=\frac{\int_{W_{\mathrm{in}}}^{W_{\mathrm{out}}}c_{\mathrm{lin}}\left(t\right)dt}{W_{\mathrm{out}}-W_{\mathrm{in}}}. \tag{6.7}$$

Substituting Eq. (6.7) into Eq. (6.6), we can finally obtain the structure of the FAQUAD taper waveguide with the taper length of L as the following expression.

$$z_{\mathrm{opt}}\left(W\right)=L\frac{\int_{W_{\mathrm{in}}}^{W}c_{\mathrm{lin}}\left(t\right)dt}{\int_{W_{\mathrm{in}}}^{W_{\mathrm{out}}}c_{\mathrm{lin}}\left(t\right)dt}. \tag{6.8}$$

By achieving a uniform distribution of $c(z)$ across the entire device, the length of the stronger coupling region can be adjusted to satisfy the adiabatic coupling condition, while the length of the weaker coupling region is minimized, thereby the length of the adiabatic taper waveguide can be greatly reduced.

6.3 PLC FAQUAD E_{31}-E_{13} taper mode converter

In this study, we used PLC waveguides with SiO_2 cladding, and the refractive index of the cladding is assumed to be 1.444. The relative refractive index difference between core and cladding is 1.0%. According to references [17], we have fixed the height of the waveguide to H = 10 μm and will focus our discussion solely on the waveguide width, denoted as W. Figure 6.1 (a) shows the calculated waveguide width dependency of the effective refractive index when H = 10 μm at the wavelength of 1.55 μm. In Fig. 6.1 (b), we have presented a zoomed-in view of the region corresponding to W ranging from 8 μm to 12 μm, as shown in the region enclosed by the red dashed line in Fig. 6.1 (a). From Fig. 6.1 (b), it can be seen that we can use a taper waveguide structure with a width ranging from 9 μm to 11 μm to achieve E_{31}-E_{13} mode conversions. In this case, the mth mode corresponds to the E_{13} ~ LP_{02} ~ E_{31} mode (cyan line), and the nth mode corresponds to the E_{31} ~ LP_{21b} ~ E_{13} mode (orange line) in Fig. 6.1 (b).

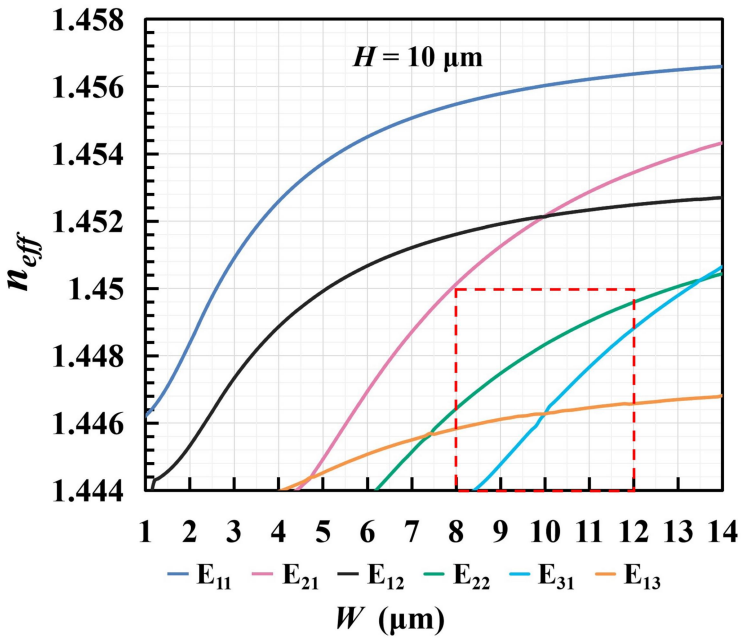

(a) In the case of H = 10 μm.

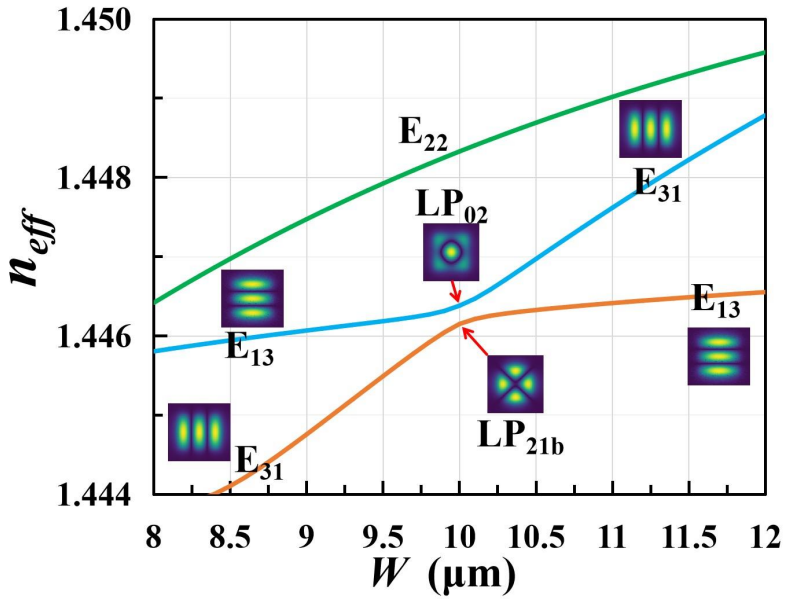

(b) The detail image of the region enclosed by the red dashed line in Fig. 6.1 (a).

Figure 6.1 Waveguide width dependency of the n_{eff}.

Figure 6.2 shows the linear taper structure with input waveguide width W_{in} = 9 μm and output waveguide width W_{out} = 11 μm. The waveguide height is fixed to H = 10 μm. Figure 6.3 shows the adiabaticity parameter $c(z)$ for the E_{31} and E_{13} or these hybrid modes in the linear taper. (The top axis represents the width of the linear taper waveguide, while the bottom axis represents the position z normalized to the taper length L in the propagation direction.) From Fig. 6.3, we can observe that the $c(z)$ of the linear taper waveguide sharply increases within the range of 9.5 μm to 10.5 μm in width. This implies that to satisfy the adiabatic coupling condition, the linear taper waveguide requires a sufficiently long waveguide length L to compensate for the large $c(z)$.

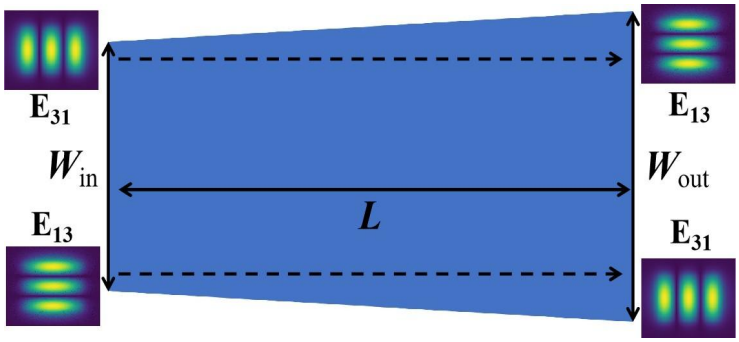

Figure 6.2 Linear taper structure with input waveguide width W_{in} = 9 μm and output waveguide width W_{out} = 11 μm.

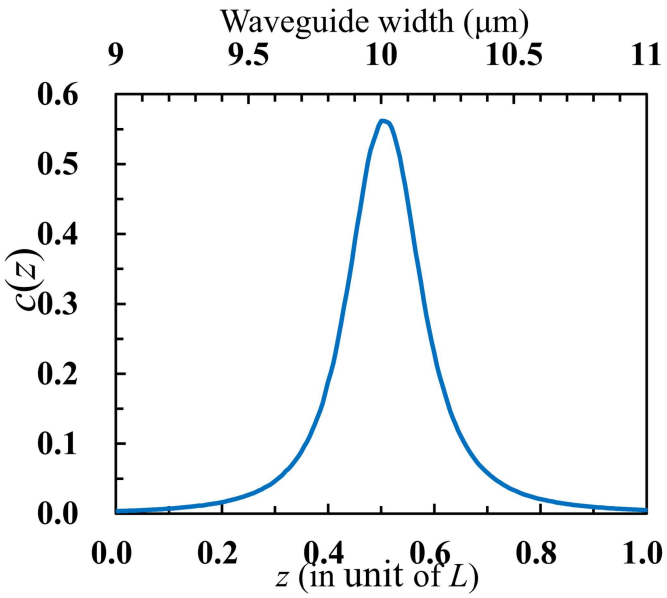

Figure 6.3 The adiabaticity parameter $c(z)$ for the E_{31} and E_{13} or these hybrid modes in the linear taper waveguide from W_{in} = 9 μm to W_{out} = 11 μm.

Figure 6.4 shows the shape parameters $z_{opt}(W)$ of the linear and FAQUAD taper waveguides with waveguide widths ranging from W_{in} = 9 μm to W_{out} = 11 μm. Figure 6.5 shows the structure of the FAQUAD taper obtained using the shape parameters from Fig. 6.4. Figure 6.6 shows the adiabaticity parameter $c(z)$ of the ideal FAQUAD taper using Eq. (6.7) (black dashed line), linear taper (blue line), and shape designed FAQUAD taper waveguide (structure in Fig. 6.5) using Eq. (6.1) (red line). From Fig. 6.6, the adiabaticity parameter of the FAQUAD taper waveguide approaches that of the ideal FAQUAD design.

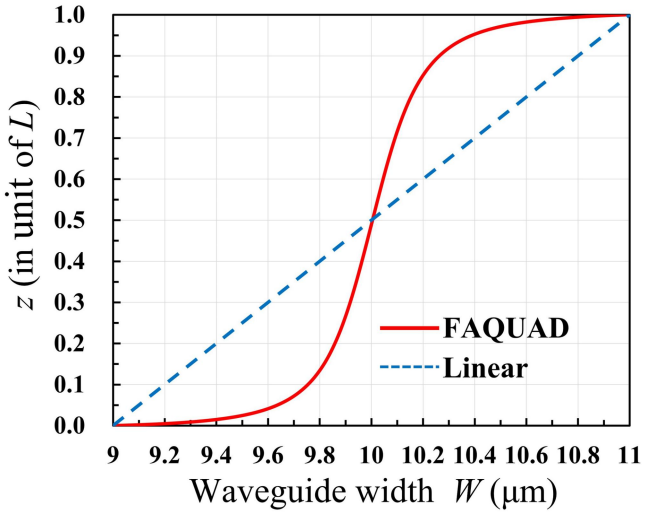

Figure 6.4 Shape parameters $z(W)$ for the linear and FAQUAD taper waveguides with waveguide widths ranging from W_{in} = 9 μm to W_{out} = 11 μm.

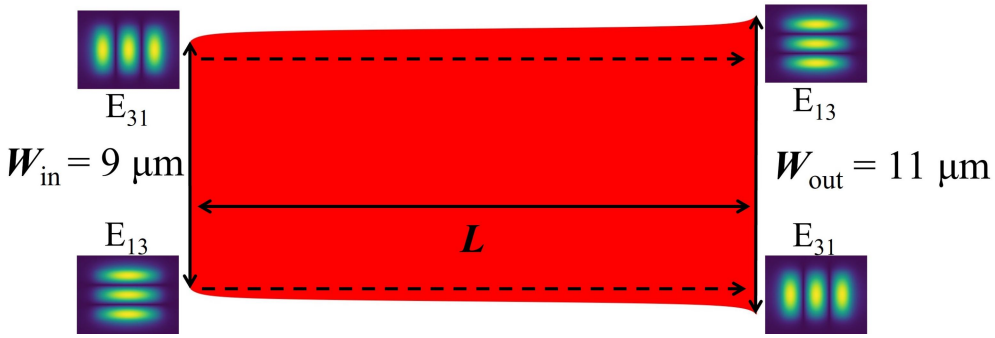

Figure 6.5 The structure of FAQUAD taper obtained using the shape parameters from Fig. 6.4.

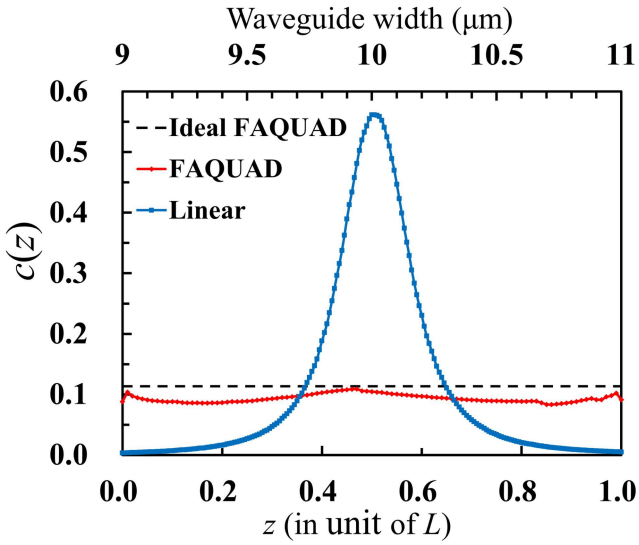

Figure 6.6 Adiabaticity parameter $c(z)$ for the linear taper (blue line), ideal FAQUAD taper (black dashed line), and shape designed FAQUAD taper waveguide (red line).

Since the waveguide shape parameters have been determined, the next step is to optimize the waveguide length by scanning the taper length L. As shown in Fig. 6.5, the variation in the shape of the FAQUAD taper in the propagation direction is non-linear. To verify the accuracy of the BPM calculation in this case, we used two calculation methods, BPM and Coupled Local Mode Theory (CLMT) for comparison. CLMT is a computationally accurate method for analyzing waveguide structures with varying widths. Figure 6.7 shows the approximated structure of a FAQUAD taper used in CLMT, which approximates the analytical structure as a continuous cuboid interval of length Δz.

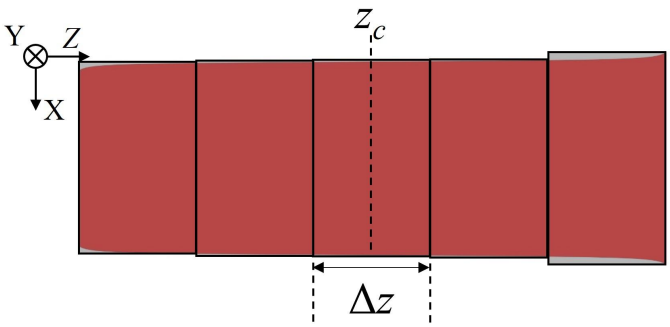

Figure 6.7 Approximated structure of a FAQUAD taper used in CLMT.

The field distribution at any arbitrary propagation position is approximated using the mode of the XY cross-section at the corresponding interval center $z = z_c$. The local coupled-mode equations of CLMT are expressed as follows [52].

$$\frac{da_m}{dz} = -\kappa_{mn}(z)\exp\left\{j\int_0^z\left[\beta_m(z)-\beta_n(z)\right]dz\right\}a_n \tag{6.9}$$

$$\kappa_{mn}(z) = \iint\left[\mathbf{E}_m \times \frac{\partial}{\partial z}\mathbf{H}_n^*\right]\cdot \boldsymbol{i}_z dxdy \tag{6.10}$$

Here, a_m, a_n are the complex amplitude coefficients of the mth and nth modes, respectively. And κ_{mn} represents the coupling coefficient between the mth and nth modes.

Figure 6.8 (a) and (b) show the relationship between the transmission for the input E_{31} mode and the waveguide length L in the case of (a) linear taper and (b)

FAQUAD taper, when W_{in} = 9 μm and W_{out} = 11 μm, respectively. From Fig. 6.8, it can be seen that the results of CLMT are basically consistent with those of BPM. According to the CLMT results, it is determined that a linear taper requires an L of 14200 μm to achieve a transmission over 90%, while an L of 30000 μm is needed to achieve a transmission over 99%. The FAQUAD taper only needs a length of about 4000 μm to achieve a transmission of over 99%. Figure 6.9 shows the relationship between the transmission for the input E_{31} mode and the wavelength of the FAQUAD E_{31}-E_{13} mode converter at various waveguide lengths (calculated by CLMT). According to Fig. 6.9, when L = 4000 μm or L = 4500 μm, the device can maintain transmission of over 90% within the wavelength range of 1.5 μm to 1.6 μm. Figure 6.10 shows the field distribution of the E_{31} mode input when L = 4000 μm, at the wavelength of 1.55 μm, which proves that the device can realize the E_{31}-E_{13} mode conversion with a shorter waveguide length.

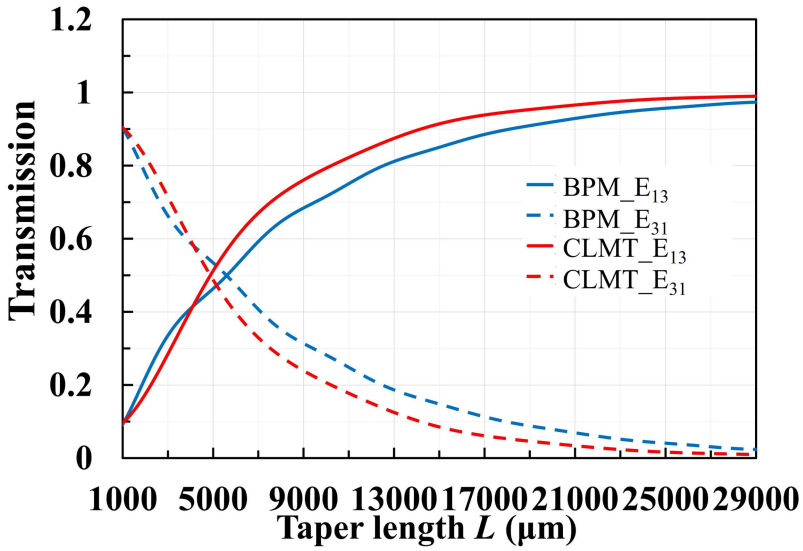

(a) In the case of linear taper.

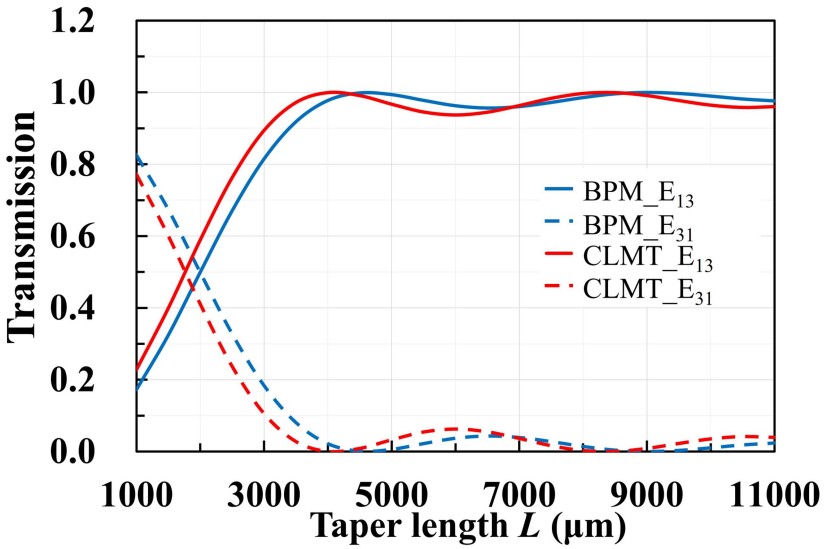

(b) In the case of FAQUAD taper, when W_{in} = 9 μm and W_{out} = 11 μm.

Figure 6.8 Relationship between the transmission for the input E_{31} mode and taper length L.

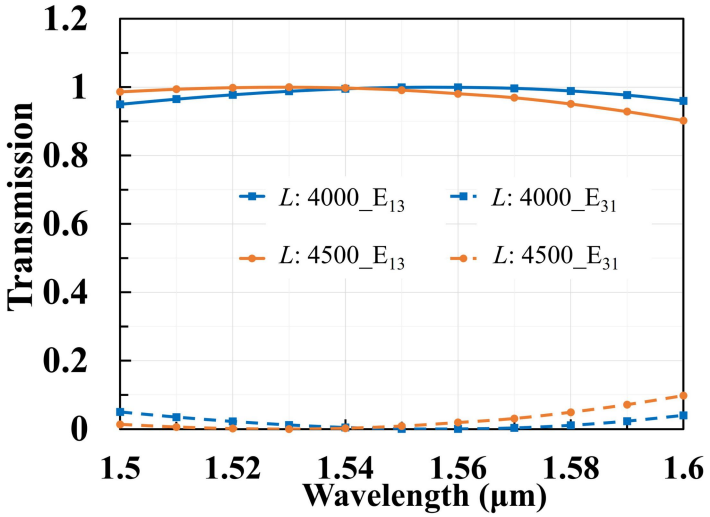

Figure 6.9 Relationship between the transmission for the input E_{31} mode and the wavelength for FAQUAD E_{31}-E_{13} mode converter at various waveguide lengths.

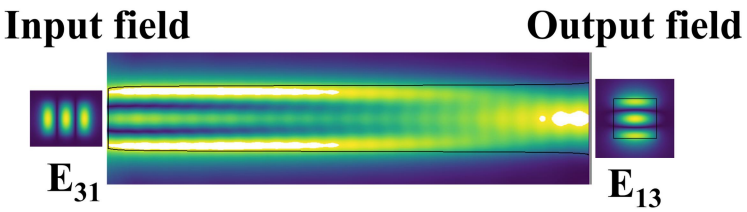

Figure 6.10 The field distribution when E_{31} mode is input from the input port. The taper length L = 4000 μm, at the wavelength of 1.55 μm.

6.4 PLC FAQUAD E-LP taper mode converter for 6-mode photonic lantern MUX

In the 6-mode MUX based on photonic lantern, the output waveguide is rectangular in shape, resulting in waveguide modes being emitted. To facilitate better connectivity with optical fibers, a tapered waveguide structure is needed at the output port to convert the rectangular waveguide into a square waveguide [51]. This enables the conversion of waveguide modes E_{31} and E_{13} to fiber-like modes LP_{02} and LP_{21b}, respectively. To connect with the photonic lantern 6-mode MUX, we set the waveguide width at the input port of the mode converter to W_{in} = 12 μm, with the waveguide height fixed at H = 10 μm [21]. As mentioned in the previous section and indicated in Fig. 6.1 (b), the E_{31}-LP_{02}, E_{13}-LP_{21b} mode converter (hereafter referred to as E-LP taper) can be achieved through a taper waveguide with the waveguide width from W_{in} = 12 μm at the input port to W_{out} = 10 μm at the output port.

Figure 6.11 shows the adiabatic parameter $c(z)$ of the ideal FAQUAD taper using Eq. (6.7) (black line), linear taper (blue line), and shape designed FAQUAD taper waveguide (structure in Fig. 6.13 (b)) using Eq. (6.1) (red line). Figure 6.12 shows the shape parameters $z(W)$ of the linear and the FAQUAD E-LP taper with waveguide widths ranging from W_{in} = 12 μm to W_{out} = 10 μm. Figures 6.13 (a) and (b) show the structure of the linear E-LP taper and the FAQUAD E-LP taper for photonic lantern 6-mode MUX, respectively.

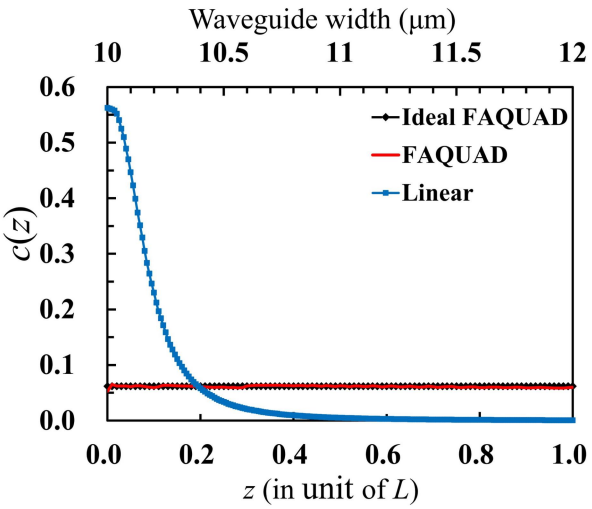

Figure 6.11 Adiabaticity parameter $c(z)$ for the linear taper (blue line), ideal FAQUAD taper (black line), and shape designed FAQUAD taper waveguide (red line).

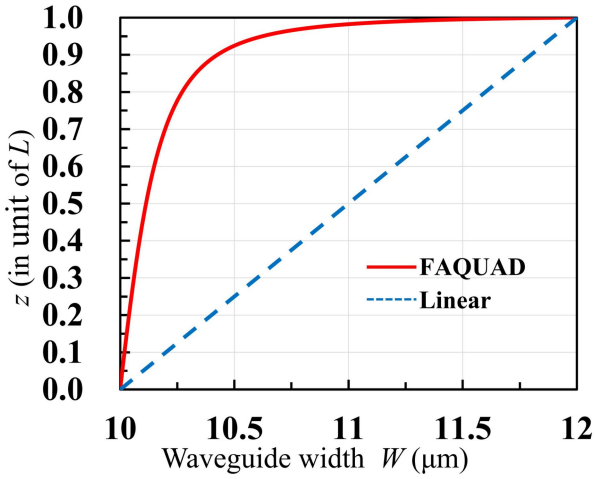

Figure 6.12 Shape parameters $z(W)$ for the linear and FAQUAD taper waveguides with waveguide widths ranging from W_{in} = 12 μm to W_{out} = 10 μm.

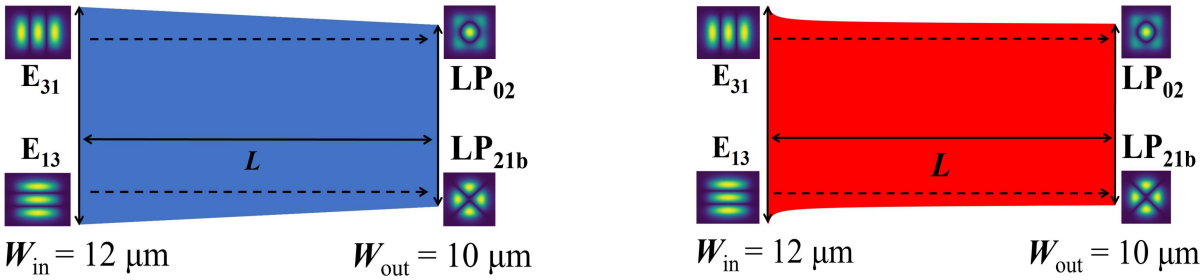

(a) Linear E-LP taper. (b) FAQUAD E-LP taper.

Fig. 6.13 The structure of the E-LP tapers for photonic lantern 6-mode MUX.

Figures 6.14 (a) and (b) show the relationship between the transmission for the input E_{31} mode and the waveguide length L in the case of (a) linear E-LP taper and (b) FAQUAD E-LP taper, when W_{in} = 12 μm and W_{out} = 10 μm, respectively. From Fig. 6.14, it can be seen that the results of CLMT are basically consistent with those of BPM. According to the CLMT results, it is determined that a linear taper requires an L of 18000 μm to achieve a transmission over 90%, while over 50000 μm is needed to achieve a transmission over 99%. The FAQUAD taper only needs a length of about 4000 μm to achieve a transmission of over 99%. Figure 6.15 shows the relationship between the transmission for the input E_{31} mode and the wavelength of the FAQUAD E_{31}-LP_{02}, and E_{13}-LP_{21b} mode converter when the waveguide length is L = 4000 μm (calculated by CLMT). According to Fig. 6.15, when L = 4000 μm, the device can maintain transmission of over 95% within the wavelength range of 1.5 μm to 1.6 μm. Figure 6.16 shows the field distribution of the E_{31} mode input when L = 4000 μm, at the wavelength of 1.55 μm, which proves that the device can realize the E_{31}-LP_{02} mode conversion with a shorter waveguide length.

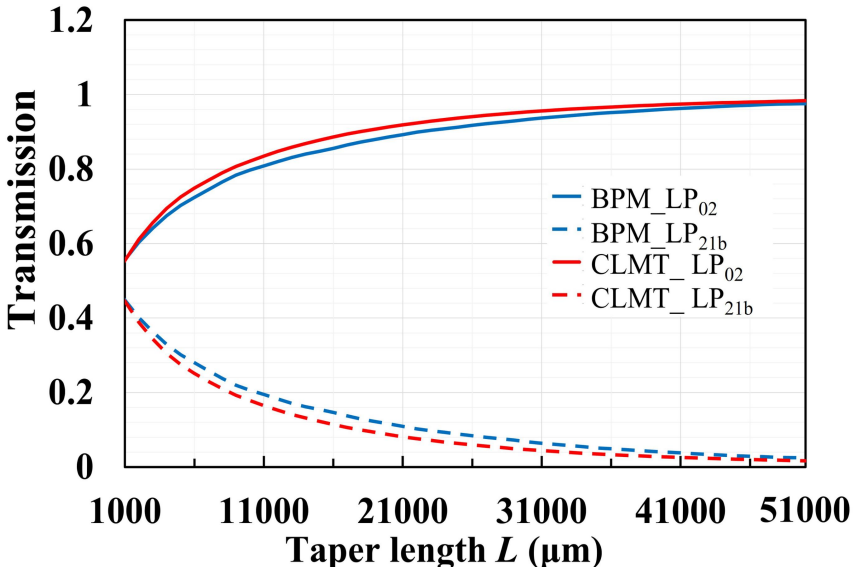

(a) In the case of linear E-LP taper.

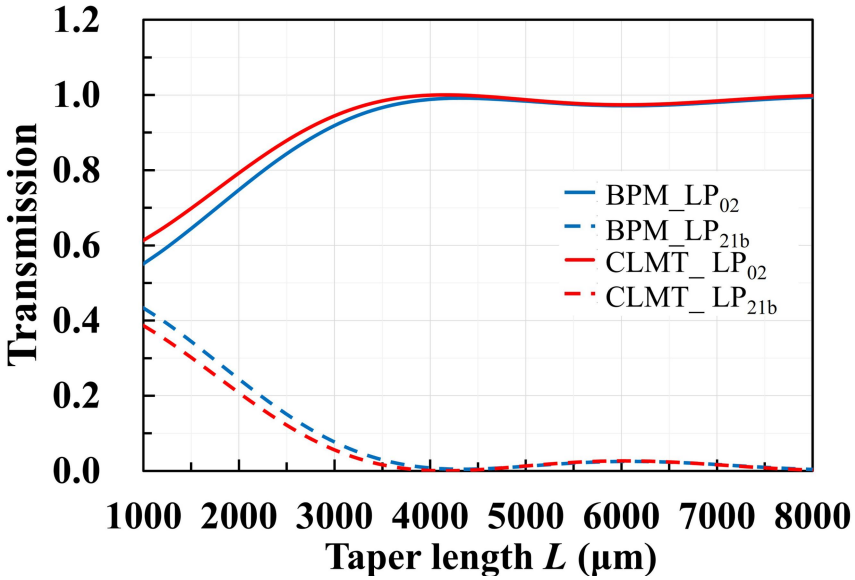

(b) In the case of FAQUAD E-LP taper.

Figure 6.14 Relationship between the transmission for the input E_{31} mode and L.

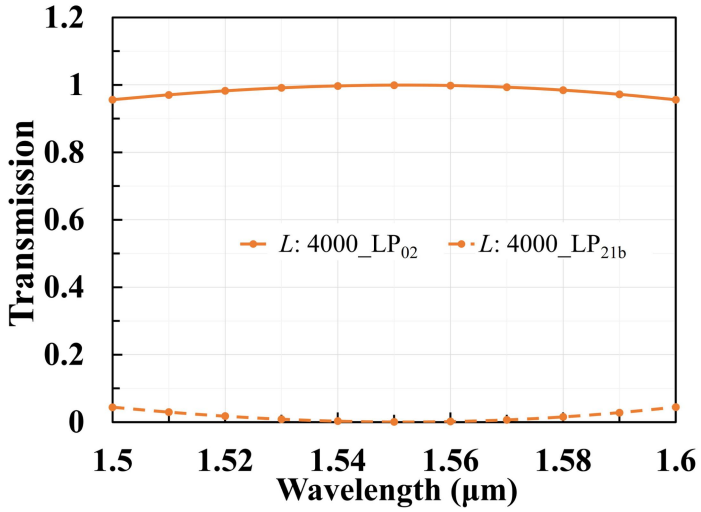

Figure 6.15 Relationship between the transmission for the input E_{31} mode and the wavelength for FAQUAD E_{31}-LP_{02}, and E_{13}-LP_{21b} mode converter at various waveguide lengths.

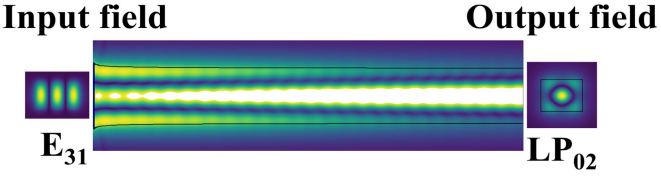

Figure 6.16 The field distribution when E_{31} mode is input from the input port. The taper length L = 4000 μm, at the wavelength of 1.55 μm.

6.5 PLC FAQUAD E-LP taper mode converter for 10-mode photonic lantern MUX

To connect with the photonic lantern 10-mode MUX, we set the waveguide width at the input port of the mode converter to W_{in} = 18 μm, with the waveguide height fixed at H = 15 μm [21]. In this case, we need to convert E_{31}, E_{13}, E_{32}, E_{23}, E_{41} and E_{14} to LP_{02}, LP_{21a}, LP_{31a}, LP_{31b}, LP_{12a}, and LP_{12b} respectively. Same as we mentioned in the previous section, we can achieve mode conversion by converting a rectangle into a square using a tapered waveguide with the waveguide width from W_{in} = 18 μm at the input port to W_{out} = 15 μm at the output port. Since the E_{32}, E_{23}, E_{41}, and E_{14} modes already have field distributions similar to that of the fiber modes, mode conversion can be achieved by directly connecting the waveguide to the fiber. Therefore, in the case of 10-mode, we still need to design the taper mode converter focused on the E_{31} and E_{13} modes.

Figure 6.17 (a) shows the calculated waveguide width dependency of the effective refractive index when H = 15 μm at the wavelength of 1.55 μm. In Fig. 6.17 (b), we have presented a zoomed-in view of the region corresponding to W ranging from 12 μm to 18 μm, as shown in the region enclosed by the red dashed line in Fig. 6.17 (a).

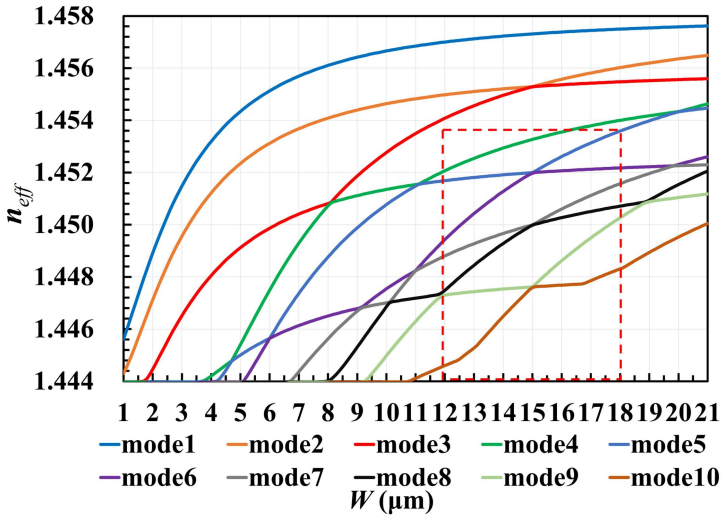

(a) In the case of H = 12 μm.

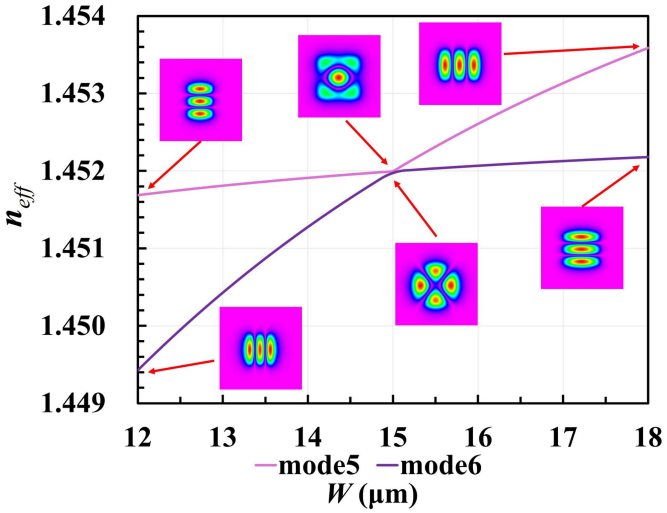

(b) The detail image of the region enclosed by the red dashed line in Fig. 6.17 (a).

Figure 6.17 Waveguide width dependency of the n_{eff}.

Figure 6.18 shows the adiabatic parameter $c(z)$ of the linear taper using Eq. (6.1). Figure 6.19 shows the shape parameters $z(W)$ of the linear and the FAQUAD E-LP taper with waveguide widths ranging from W_{in} = 18 μm to W_{out} = 15 μm. Figures 6.20 (a) and (b) show the structure of the linear E-LP taper and the FAQUAD E-LP taper, respectively.

As shown in Fig. 6.17 (b), since the gap of the E_{31} and E_{13} mode dispersion curves at the point of W = 15 μm is very small, this means that a longer taper length is required for the taper mode converter to achieve adiabatic conversion. Since the length required for the linear taper is too long here, we only show the output field distribution when the mode begins to convert (L = 2000000 μm = 2 m), as shown in Fig. 6.21. As can be seen from Fig. 6.21, the linear taper requires a length of more than 2 m to achieve adiabatic conversion. Figure 6.22 shows the relationship between the LP_{02} mode transmission and the waveguide length L in the case of FAQUAD E-LP taper when E_{31} mode input. According to the results, the FAQUAD taper only needs a length of about 47500 μm to achieve a transmission of over 95%.

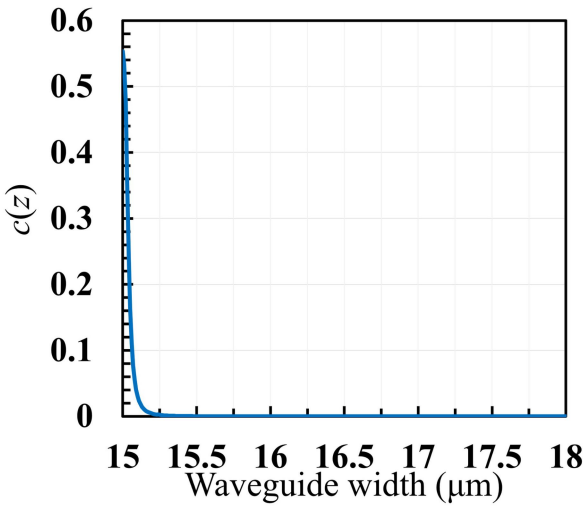

Figure 6.18 Adiabatic parameter $c(z)$ of the linear taper.

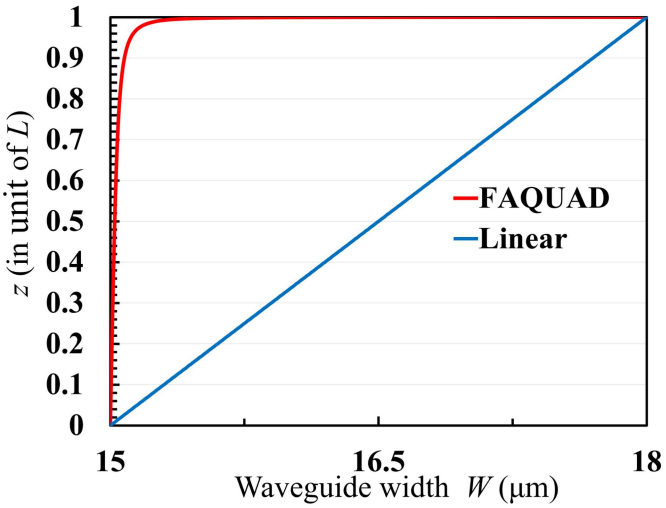

Figure 6.19 Shape parameters $z(W)$ of the linear and the FAQUAD taper.

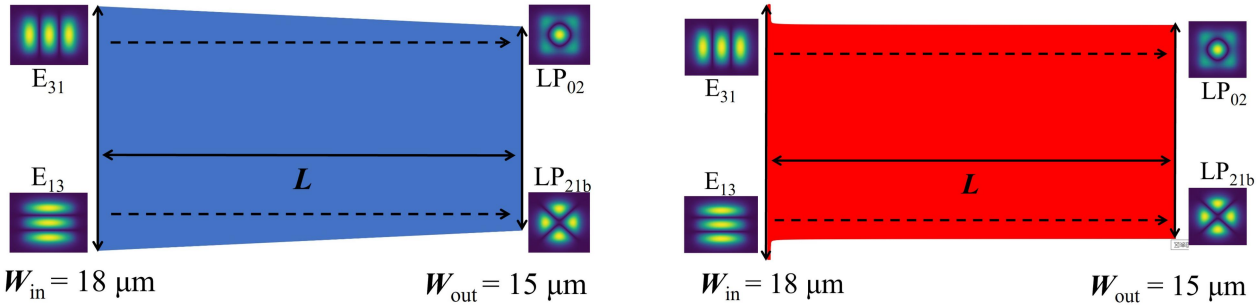

(a) Linear taper. (b) FAQUAD taper.

Figure 6.20 The structure of the E-LP tapers for photonic lantern 10-mode MUX.

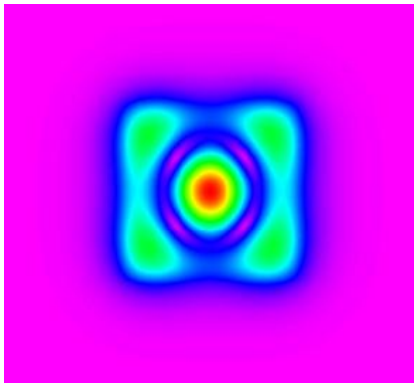

Figure 6.21 Output field distribution of linear taper with L = 2 m, when E_{31} mode input from the input port.

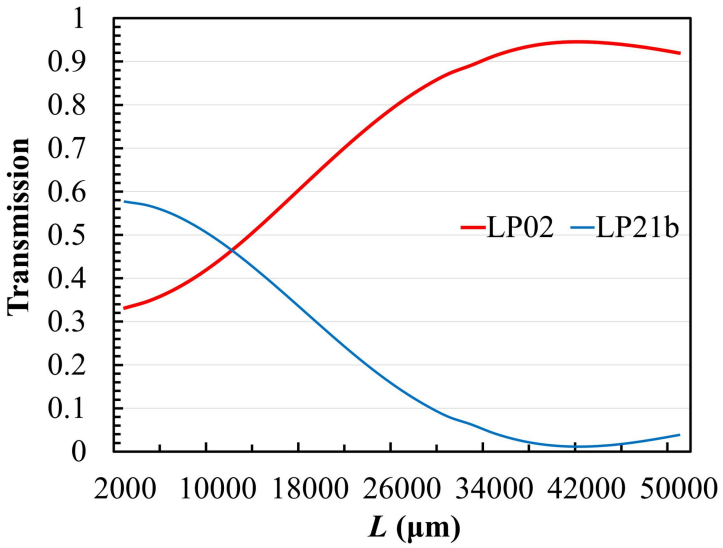

Figure 6.22 Relationship between the transmission for the input E_{31} mode and L of the FAQUAD.

At the same time, we can find that the sum of the output LP_{02} mode and LP_{21b} mode is not 1. This is because the shape of the taper starting from 18 μm changes too drastically near the input, thus causing scattering loss. Therefore, we designed a 2-segment structure connected by a linear taper and a FAQUAD taper to reduce the intensity of the shape change of the near input section. In the 2-segment structure, we use the linear structure in the part with waveguide width W = 18 ~ 16 μm, and the FAQUAD structure in the part with 16 ~ 15 μm. Figure 6.23 shows the adiabatic parameter $c(z)$ of the linear taper using Eq. (6.1). Figure 6.24 shows the shape parameters $z(W)$ of the linear and the FAQUAD E-LP taper with

waveguide widths ranging from W_{in} = 16 μm to W_{out} = 15 μm. Figure 6.25 shows the structure of the 2-segment E-LP taper.

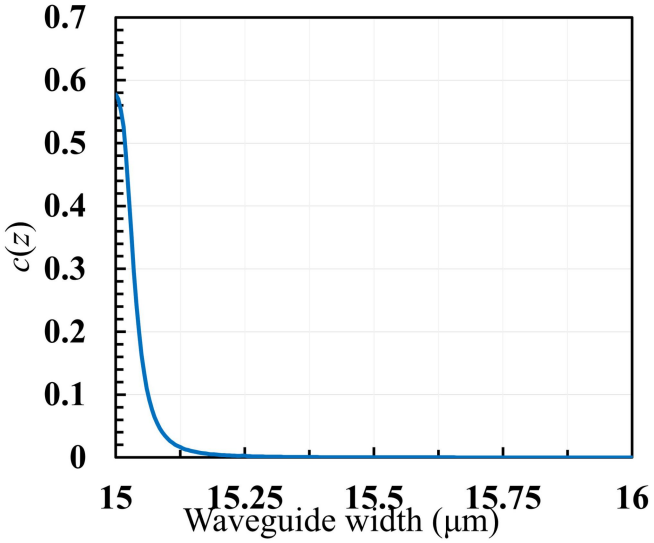

Figure 6.23 Adiabatic parameter $c(z)$ of the linear taper when W_{in} = 16 μm and W_{out} = 15 μm.

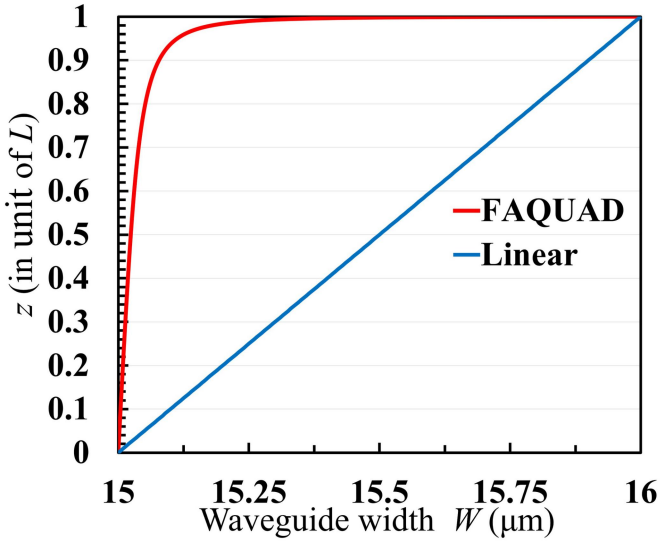

Figure 6.24 Shape parameters $z(W)$ of the linear and the FAQUAD taper when W_{in} = 16 μm and W_{out} = 15 μm.

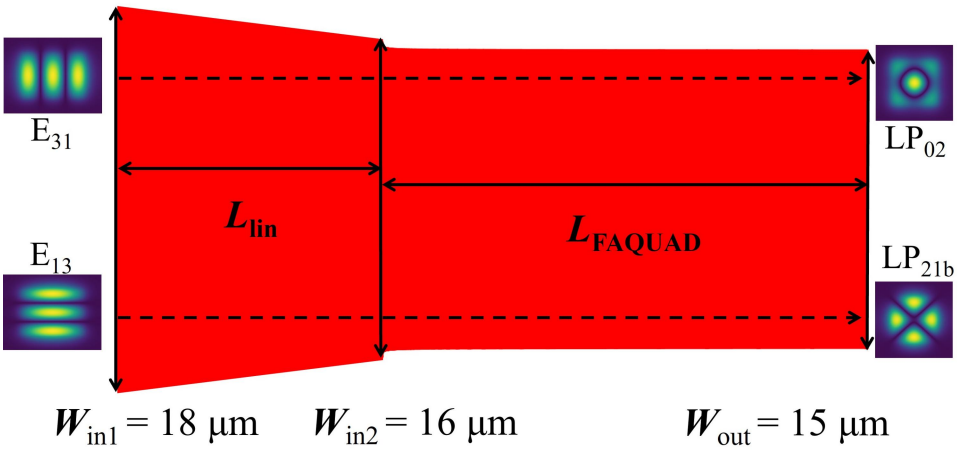

Figure 6.25 The structure of the 2-segment E-LP taper.

Figure 6.26 shows the relationship between the LP_{02} mode transmission and the waveguide length L_{lin} *and* L_{FAQUAD} when E_{31} mode input. According to the results, the 2-segment taper can achieve transmission of over 98% when L_{lin} = 4000 μm and L_{FAQUAD} = 42000 μm. Figure 6.27 shows the relationship between LP_{02} mode transmission and L_{FAQUAD} when L_{lin} is fixed at 4000 μm. We can observe that at this time, due to the slowdown in shape changes near the input port, the transmission of the LP_{02} mode is 0.9869, while the transmission of the LP_{21b} mode is 0.0098, the sum of the transmission of the two modes is 0.9967. Therefore, the scattering loss is reduced.

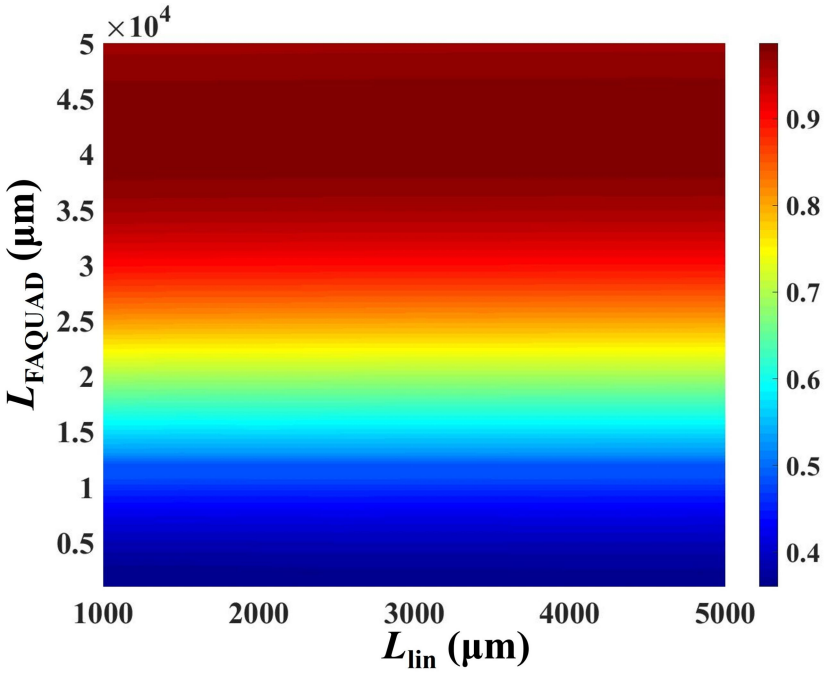

Figure 6.26 The relationship between the LP_{02} mode transmission and the waveguide length L_{lin} *and* L_{FAQUAD} when E_{31} mode input.

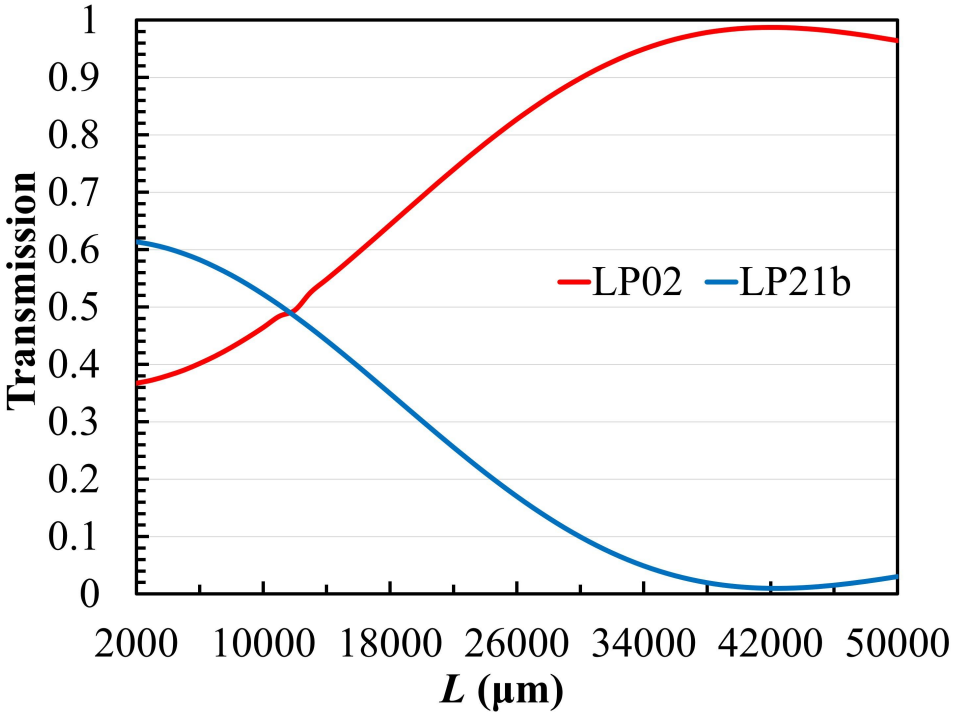

Figure 6.27 The relationship between LP_{02} mode transmission and L_{FAQUAD} when L_{lin} is fixed at 4000 μm.

Chapter 7 Photonic crystal mode MUXs

7.1 Preface

Combining WDM and MDM technologies is effective in expanding transmission capacity from long-distance fiber communication to very-short-reach chip-based communication. WDM/MDM hybrid multiplexing technology that can realize wavelength and mode division multiplexing at the same time was proposed [38]–[40]. Photonic Crystals (PC) are widely studied because of their unique performance and high integration density [53], [54]. In some studies of WDM/MDM hybrid MUXs, WDM and MDM parts adopt different structures, WDM parts use hole-type PC, and MDM use Si wire waveguides [38]. In this case, the loss will occur in the connection part of the PC and Si waveguide. Therefore, all PC mode MUX is desired to integrate all components for chip communications with PC Waveguides (PCWs).

In this study, we proposed a 5-mode multiplexer by cascading four ADCs based on 2D pillar square-lattice PCWs. The device can selectively excite 5 target modes (TE_0, TE_1, TE_2, TE_3, and TE_4 modes) by choosing the input ports. Then, we proposed a ultracompact mode MUX based on the air-hole type triangular-lattice PCWs which have more practical applications. By using ADC, it is possible to compose TE_0-TE_1 mode MUX by changing the waveguides widths. The longitudinal sizes are only 2.05 μm, which is significantly smaller than those based on Si-wire waveguides [22].

7.2 The working principle of photonic crystal

PC is an artificial nanoscale microstructure, which is composed of periodically arranged media with different refractive indexes. As shown in Fig. 7.1, based on the distribution of the medium, PCs can be divided into 1D PC, 2D PC, and 3D PC. In a 1D PC, two different materials alternate periodically in one direction while remaining constant in the other two directions. A 2D PC features two different materials alternating periodically in two directions while remaining constant in the vertical direction. A 3D PC involves two different materials arranged periodically in all three directions. The structure and fabrication of 1D PCs are relatively simple. 2D PCs, while more complex in structure compared to 1D PCs, are widely studied and applied. Removing a single material pillar/hole or a row of material pillars/holes in a complete 2D PC can alter its performance. The theoretical calculations for 3D structures are challenging, and the manufacturing process is complex. However, 3D PCs exhibit the absence of light leakage in all directions, a characteristic known as a complete bandgap. Since 2D PC is widely used and can form PCW more intuitively, we chose 2D PC as the main research object in this study.

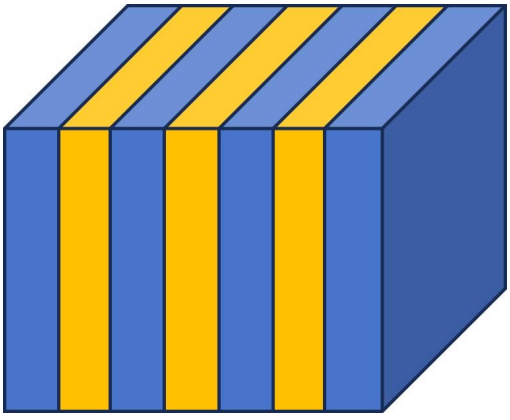

(a) 1D PC

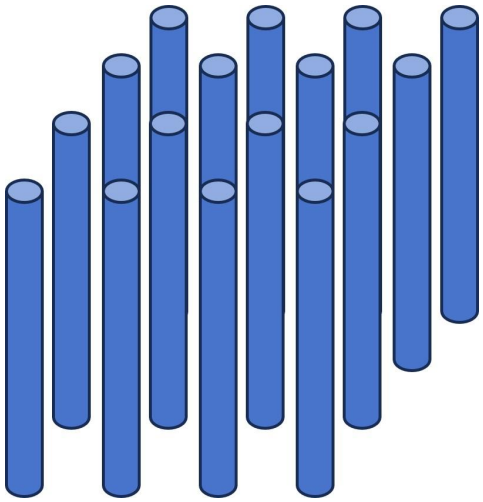

(b) 2D PC

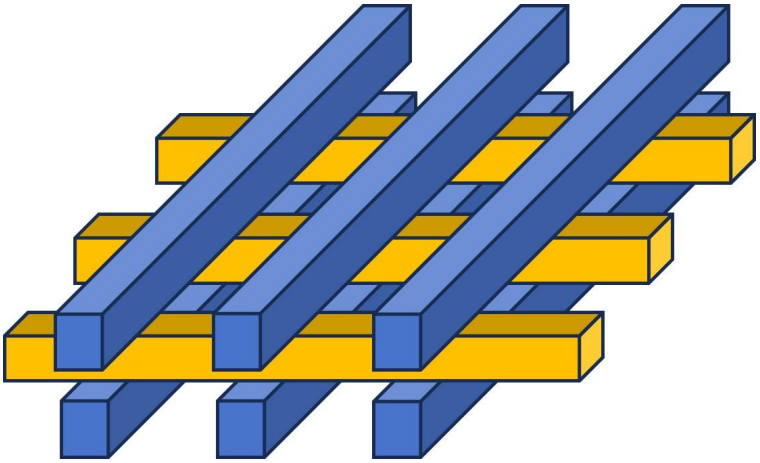

(c) 3D PC

Figure 7.1 Photonic crystal structures.

PC exhibits two crucial characteristics: Photonic Band Gap (PBG) and Photonic Localization.

Due to the periodic distribution of the dielectric constant inside the PC, a periodic potential field is generated, leading to the influence of Bragg scattering on photons. This phenomenon results in the formation of the PC's band structure, and the gaps between the bands are called PBGs. Light with frequencies within the PBG range is suppressed and cannot propagate, serving as a mechanism for wavelength selection. Figures 7.2 (a) and (b) show XZ-plane views of a 2D square-lattice pillar-type PC and triangular-lattice air-hole-type PC, respectively. Figures 7.3 (a) and (b) show the corresponding band diagrams of the 2D PCs, with the shaded orange regions representing PBGs. Light with frequencies within these shaded regions cannot propagate in the PC.

The photonic localization is also known as the defect mode characteristic. In a complete PC, light with frequencies within the PBG cannot transmit. However, by introducing point defects or line defects, the periodic structure is disrupted, confining light within the defect. As shown in Fig. 7.4 (a), removing a single air hole forms a PC cavity, and in Fig. 7.4 (b), removing a row of air holes creates a PCW.

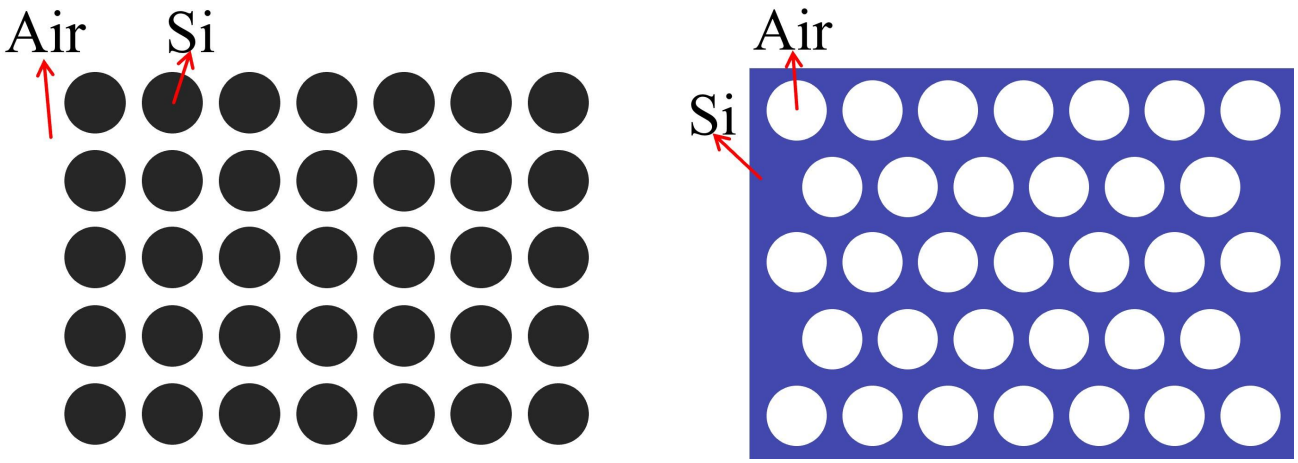

(a) Square-lattice pillar PC. (b) Triangular-lattice air-hole PC.

Figure 7.2 Two typical 2D PC structures.

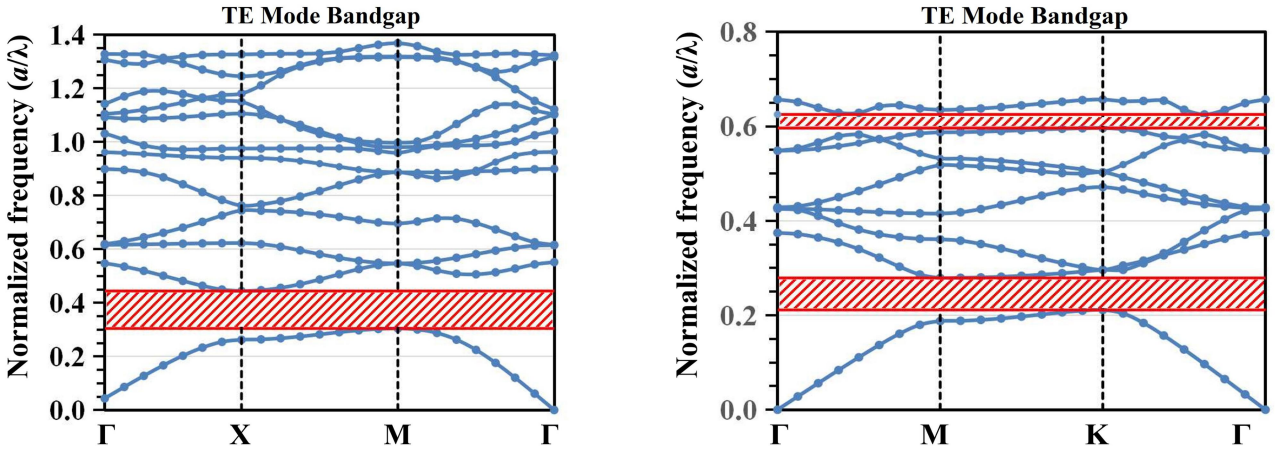

(a) Suare-lattice pillar PC PBG. (b) Triangular-lattice air-hole PC PBG.

Figure 7.3 The band structures of the two PCs in Fig. 7.2.

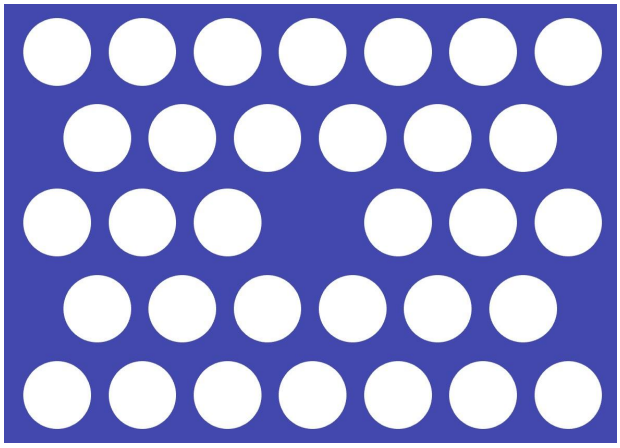

(a) Point defect.

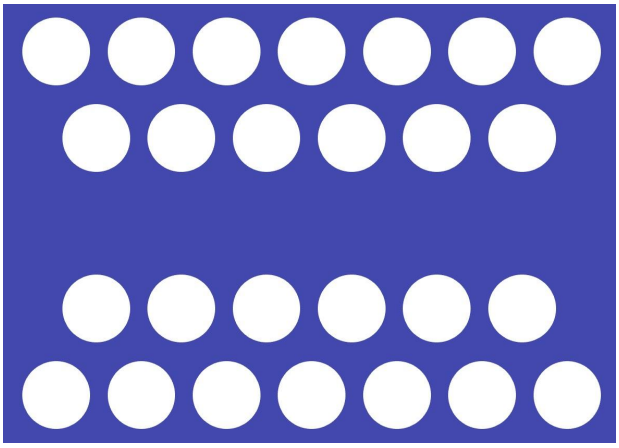

(b) Line defect.

Figure 7.4 Two defective structures of PC.

7.3 PBG calculation method – Plane Wave Expansion method

The PC structure is periodic. Therefore, when calculating the PBG, you only need to calculate the band structure of one period to get the band gap of the entire PC. First, the light waves transmitted in PC satisfy Maxwell's equations:

$$\begin{aligned}
&\nabla \cdot \mathbf{D}(\mathbf{r},t) = \rho(\mathbf{r},t) \\
&\nabla \cdot \mathbf{B}(\mathbf{r},t) = 0 \\
&\nabla \times \mathbf{H}(\mathbf{r},t) = \mathbf{J}(\mathbf{r},t) + \frac{\partial}{\partial t}\mathbf{D}(\mathbf{r},t) \\
&\nabla \times \mathbf{E}(\mathbf{r},t) = -\frac{\partial}{\partial t}\mathbf{B}(\mathbf{r},t)
\end{aligned} \tag{7.1}$$

Assuming that the space where electromagnetic waves exist is a passive space and the medium is a lossless medium, the relative permittivity $\varepsilon(\mathbf{r})$ is a real number, the current density vector $\mathbf{J}(\mathbf{r}) = 0$, and the charge density $\rho(\mathbf{r}) = 0$. If the electromagnetic wave satisfies Fourier theory as a plane wave and the magnetic field is uniform, the magnetic permeability $\mu(\boldsymbol{r})$ is a constant. Therefore, an isotropic linear medium has the following inherent relationship.

$$\begin{cases} \mathbf{D}(\mathbf{r},t) = \varepsilon_0 \varepsilon(\mathbf{r},t)\mathbf{E}(\mathbf{r},t) \\ \mathbf{B}(\mathbf{r},t) = \mu \mathbf{H}(\mathbf{r},t) \\ \mathbf{J}(\mathbf{r},t) = \sigma \mathbf{E}(\mathbf{r},t) \end{cases} \tag{7.2}$$

If the input field is a sine function, the electric and magnetic fields are expressed as follows.

$$\begin{cases} \mathbf{E}(\mathbf{r},t) = \mathbf{E}(\mathbf{r})\exp(i\omega t) \\ \mathbf{H}(\mathbf{r},t) = \mathbf{H}(\mathbf{r})\exp(i\omega t) \end{cases} \tag{7.3}$$

Substituting equations (2) and (3) into equation (1), we get

$$\begin{cases} \nabla \cdot \varepsilon_0 \varepsilon(\mathbf{r})\mathbf{E}(\mathbf{r}) = 0 \\ \nabla \cdot \mu_0 \mathbf{H}(\mathbf{r}) = 0 \\ \nabla \times \mathbf{H}(\mathbf{r}) = i\omega\varepsilon_0 \varepsilon(\mathbf{r})\mathbf{E}(\mathbf{r}) \\ \nabla \times \mathbf{E}(\mathbf{r}) = -i\omega\mu \mathbf{H}(\mathbf{r}) \end{cases} \tag{7.4}$$

If we take the rotation from the above equation, we get the following PC characteristic equation.

$$\begin{aligned} \nabla \times \left[\frac{1}{\mu(\mathbf{r})} \nabla \times \mathbf{E}(\mathbf{r}) \right] &= \omega^2 \varepsilon(\mathbf{r})\mathbf{E}(\mathbf{r}) \\ \nabla \times \left[\frac{1}{\varepsilon(\mathbf{r})} \nabla \times \mathbf{H}(\mathbf{r}) \right] &= \frac{\omega^2}{c^2} \mathbf{H}(\mathbf{r}) \end{aligned} \tag{7.5}$$

Here, $\varepsilon(\mathbf{r})$ is the dielectric constant, $\mathbf{H}(\mathbf{r})$ is the magnetic field strength vector and are periodic function whose period is the lattice constant $\mathbf{R}$ of PC. Form Bloch's theorem, in a perfect lattice structure, electron movement is only affected by defects that destroy the lattice structure, and this conclusion can be applied to PC as well. Therefore, $\mathbf{H}(\mathbf{r})$ can be expressed as follows.

$$\begin{cases} \mathbf{H}(\mathbf{r}) = \exp(i\mathbf{k}\cdot\mathbf{r})h(\mathbf{r})\mathbf{e}_k \\ h(\mathbf{r}+\mathbf{R}) = h(\mathbf{r}) \end{cases} \tag{7.6}$$

Here, $\mathbf{R} = m_1\mathbf{a}_1 + m_2\mathbf{a}_2 + m_3\mathbf{a}_3$ is a regular lattice vector, $\mathbf{a}_i$ is a regular lattice basis

vector, and m_i is an arbitrary integer. And define $\mathbf{G} = n_1\mathbf{b}_1+n_2\mathbf{b}_2+n_3\mathbf{b}_3$ as a reciprocal lattice vector, $\mathbf{b}_i$ is a reciprocal lattice basis vector, and n_i is an arbitrary integer. The normal basis vector and the inverse basis vector satisfy the following relationship.

$$\mathbf{a}_i \cdot \mathbf{b}_j = 2\pi\delta_{ij} = \begin{cases} 2\pi, i = j \\ 0, i \neq j \end{cases} (i, j = 1, 2, 3)\ldots \tag{7.7}$$

Since the relative dielectric constant $\varepsilon(\mathbf{r})$ of PC is periodically distributed in space, $\varepsilon(\mathbf{r})$, $1/\varepsilon(\mathbf{r})$, and the periodic function $h(\mathbf{r})$ can be expanded as plane waves in a reciprocal vector space. inversely distributed as shown in the following equation.

$$\begin{cases} \varepsilon(\mathbf{r}) = \Sigma_{\mathbf{G}}\varepsilon(\mathbf{G})\exp(i\mathbf{G}\cdot\mathbf{r}) \\ \dfrac{1}{\varepsilon(\mathbf{r})} = \Sigma_{\mathbf{G}}\varepsilon^{-1}(\mathbf{G})\exp(i\mathbf{G}\cdot\mathbf{r}) \\ h(\mathbf{r}) = \Sigma_{\mathbf{G}}h(\mathbf{G})\exp(i\mathbf{G}\cdot\mathbf{r}) \end{cases} \tag{7.8}$$

Substituting equation (8) into equation (6), we get

$$\mathbf{H}(\mathbf{r}) = \sum_{\mathbf{G},\lambda} h(\mathbf{G},\lambda)\exp\left[i(\mathbf{k}+\mathbf{G})\cdot\mathbf{r}\right]\cdot\mathbf{e}_{\lambda,\mathbf{k}+\mathbf{G}}(\lambda = 1, 2) \tag{7.9}$$

Here, $\mathbf{G}$ represents a reciprocal lattice vector, and $\mathbf{e}_{1,\,\mathbf{k}+\mathbf{G}}$ and $\mathbf{e}_{2,\,\mathbf{k}+\mathbf{G}}$ represent two direction vectors perpendicular to $\mathbf{k}+\mathbf{G}$, respectively. Substituting equations (8) and (9) into equation (5), we obtain the following eigen equation for $h(\mathbf{r})$.

$$\sum_{\mathbf{G}}\varepsilon^{-1}(\mathbf{G}_i-\mathbf{G})|\mathbf{k}+\mathbf{G}||\mathbf{k}+\mathbf{G}_i|\begin{pmatrix} \mathbf{e}_{2,\mathbf{k}+\mathbf{G}_i}\cdot\mathbf{e}_{2,\mathbf{k}+\mathbf{G}} & -\mathbf{e}_{2,\mathbf{k}+\mathbf{G}_i}\cdot\mathbf{e}_{1,\mathbf{k}+\mathbf{G}} \\ -\mathbf{e}_{1,\mathbf{k}+\mathbf{G}_i}\cdot\mathbf{e}_{2,\mathbf{k}+\mathbf{G}} & \mathbf{e}_{1,\mathbf{k}+\mathbf{G}_i}\cdot\mathbf{e}_{1,\mathbf{k}+\mathbf{G}} \end{pmatrix}\begin{pmatrix} h(\mathbf{G},1) \\ h(\mathbf{G},2) \end{pmatrix} = \frac{\omega^2}{c^2}\begin{pmatrix} h(\mathbf{G}_i,1) \\ h(\mathbf{G}_i,2) \end{pmatrix} \tag{7.10}$$

When a certain wave number vector k is selected, a series of eigenvalues corresponding to the wave number vector k are obtained by the above formula, and therefore the eigenfrequency can be obtained and the band gap of the photonic crystal can be obtained. For 2D PC, the above equation can be simplified into two independent unique equations corresponding to the TE and TM modes.

$$\text{TE}:\sum_{\mathbf{G}}\varepsilon^{-1}(\mathbf{G}_i-\mathbf{G})|\mathbf{k}+\mathbf{G}||\mathbf{k}+\mathbf{G}_i|\begin{pmatrix}h(\mathbf{G},1)\\h(\mathbf{G},2)\end{pmatrix}=\frac{\omega^2}{c^2}\begin{pmatrix}h(\mathbf{G}_i,1)\\h(\mathbf{G}_i,2)\end{pmatrix}$$
$$\text{TM}:\sum_{\mathbf{G}}\varepsilon^{-1}(\mathbf{G}_i-\mathbf{G})(\mathbf{k}+\mathbf{G})\cdot(\mathbf{k}+\mathbf{G}_i)\begin{pmatrix}h(\mathbf{G},1)\\h(\mathbf{G},2)\end{pmatrix}=\frac{\omega^2}{c^2}\begin{pmatrix}h(\mathbf{G}_i,1)\\h(\mathbf{G}_i,2)\end{pmatrix} \quad (7.11)$$

Take 2D square-lattice PC shown in Fig. 7.5 (a) as an example, the lattice constant is a, the regular lattice basis vectors can be expressed as $\mathbf{a}_1 = \mathbf{a}[1,0]$, $\mathbf{a}_2 = \mathbf{a}[0,1]$, and the points Γ, X, and M are Γ = 2π/**a**[0,0], X = 2π/**a**[1/2,0], and M = 2π/**a**[1/2,1/2], respectively. By solving the characteristic equation (7.10), we can obtain the PBG of the 2D square lattice PC.

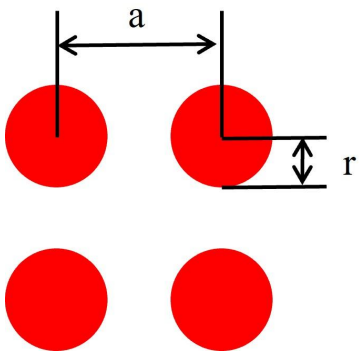

(a) 2D square-lattice PC.

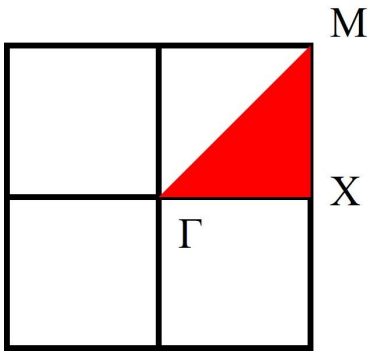

(b) First Pluanzone of 2D square-lattice PC.

Figure 7.5 2D square-lattice PC for example.

7.4 5-mode MUX using pillar type PCWs

Figure 7.6 shows the schematic of the complete structure of the 2D square-lattice PC with dielectric pillars used in this study. We set the background to air and Si as the material for the dielectric pillars, with effective refractive indices of $n_{\text{Air}} = 1$ and $n_{\text{Si}} = 3.4$, respectively. Figure 7.7 shows the PBG diagram of the complete PC when the lattice constant is a, and the radius of the Si pillars is $r = 0.167a$, which using the same parameter as in [39], calculated by PWE method (the shaded region represents the PBG. As can be seen from Fig. 7.7, the PC structure has a PBG around normalized frequency from 0.304 to 0.444 (a/λ). To

achieve a PBG around the target wavelength of 1.55 μm, we set the lattice constant to a = 0.54 μm, corresponding to the PBG ranging from 1.22 to 1.78 μm. The Si pillar radius is also determined as r = 0.09 μm from r = 0.167a.

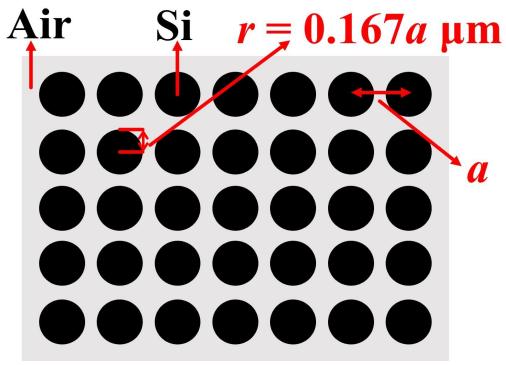

Figure 7.6 The complete structure of the 2D PC.

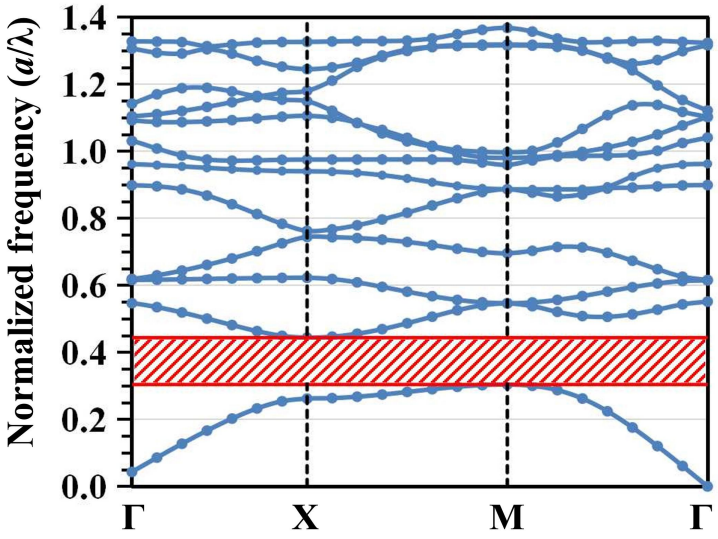

Figure 7.7 The PBG of the complete PC.

To enable the multimode transmission by the PC structure, line defect is introduced into the complete PC structure by removing a row of dielectric pillars, thus forming a PC waveguide. Figures 7.8 (a) and (b) show the W1-PC waveguide structure formed after removing a row of dielectric pillars and the dispersion curve of the waveguide calculated by PWE, respectively. As shown in Fig. 7.8 (b), we can see that there exists a guided mode dispersion curve in the PBG for the case where the width of the PC waveguide is $W = 2a$ = 1.08 μm, which means that the

fundamental TE_0 mode can propagate in the W1-PC waveguide. In the case of a = 0.54 μm, the target wavelength of 1.55 μm corresponds to a normalized frequency of 0.348, and the normalized propagation constant β of the TE_0 mode is 0.176, as shown in Fig. 7.8 (b).

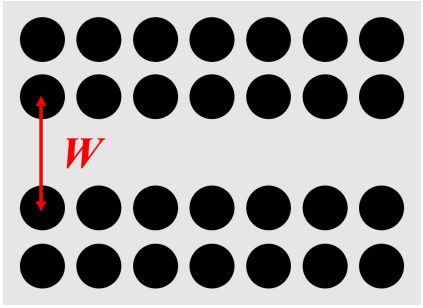

(a) W1-PC waveguide structure.

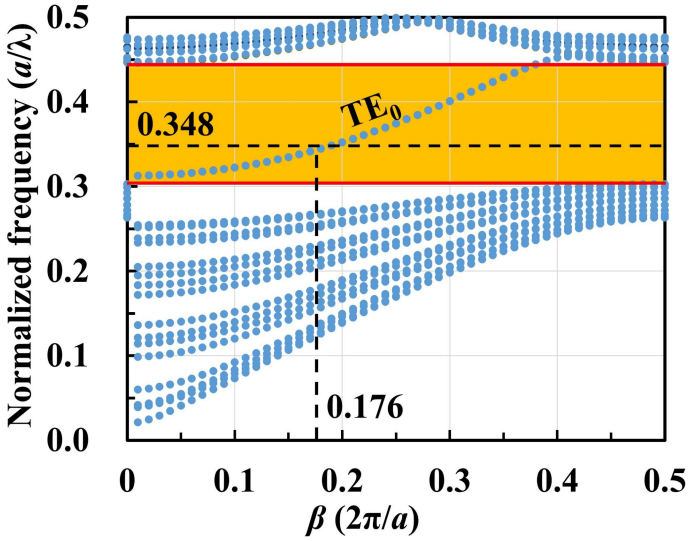

(b) Dispersion curve.

Figure 7.8 W1-PC waveguide structure and the dispersion curve of the waveguide.

To enable the waveguide to support higher-order modes, we gradually increased the width of the W1-PC waveguide and calculated the relationship between the propagation constant β of each mode and the waveguide width W at a normalized frequency of 0.348 as shown in Fig. 7.9. The horizontal axis in Fig. 7.9 represents the width of the W1-PC waveguide in units of the lattice constant a, while the

vertical axis represents the normalized propagation constant β. From Fig. 7.9, we can see that when $W = 2a$, the normalized propagation constant of the TE_0 mode is 0.176, which is consistent with the result in Fig. 7.8 (b). Moreover, we can observe that as the width W increases to $3.66a$, $5.32a$, $6.99a$, and $8.65a$, higher order modes (TE_1, TE_2, TE_3, and TE_4 modes) will have the same propagation constants of TE_0 mode, which are 0.176, respectively. This means that at these waveguide widths, each higher-order mode can achieve phase matching with the TE_0 mode.

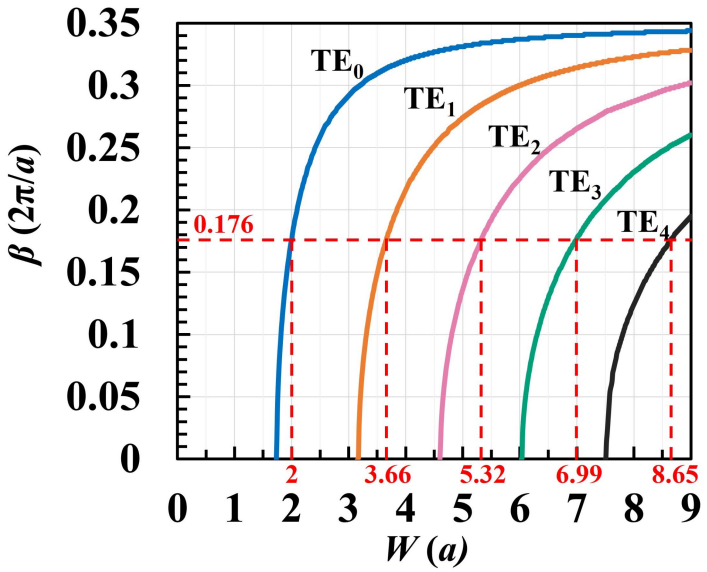

Figure 7.9 Relationship between the propagation constant β of each mode and the width W of the waveguide at a normalized frequency of 0.348.

Figure 7.10 shows a schematic structure of the PC 5-mode MUX designed in this study. The device consists of four ADC structures, each connected by a tapered waveguide. When TE_0 mode is respectively input from ports 1, 2, 3, 4, and 5, the output ports will output TE_0, TE_1, TE_2, TE_3, and TE_4 modes, respectively. We designed the PC mode MUX using an ADC structure, where the width of each input single-mode waveguide was set to $W_1 = 2a = 1.08$ μm. To achieve phase matching, we designed each multimode waveguide based on Fig. 7.9, where the parameters for each waveguide were set as follows: $W_2 = 3.66a = 1.976$ μm, $W_3 = 5.32a = 2.873$ μm, $W_4 = 6.99a = 3.775$ μm, and $W_5 = 8.65a = 4.671$ μm. The two waveguides of each ADC are separated by two rows of pillars, as shown in Fig. 7.10. We used the same taper structure as in [41] at the connection part of each

multimode waveguide, with a length of $L_1 = 5a = 2.7$ μm. We conducted transmission simulations using Finite Difference Time Domain method (FDTD by Lumerical) on a structure with a parallel arrangement of the single-mode waveguide and multi-mode waveguide to determine the coupling lengths of each ADC section. The coupling lengths of each ADC section are set to $L_2 = 21a = 11.34$ μm, $L_3 = 25a = 13.5$ μm, $L_4 = 28a = 15.12$ μm, and $L_5 = 30a = 16.2$ μm, respectively.

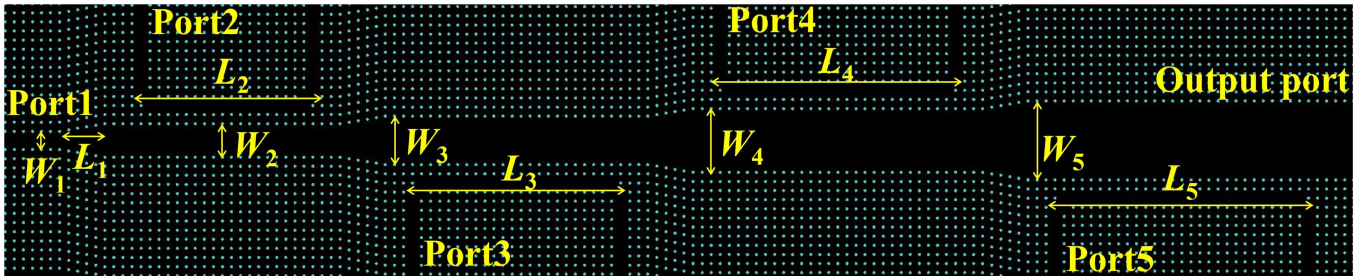

Figure 7.10 Structure of the PC 5-mode MUX.

The electric field distribution of the device, when the TE_0 mode is input from the input ports 1, 2, 3, 4, and 5, are shown in Figs. 7.11 (a), (b), (c), (d), and (e), respectively. It can be seen from Fig. 7.11 that the device can achieve 5-mode multiplexing. The transmission of each output mode at the output port is shown in Fig. 7.12. The losses when the TE_0 mode is input from each port are Port1: -0.16 dB, Port2: -0.43 dB, Port3: -0.36 dB, Port4: -0.49 dB, and Port5: -0.16 dB, respectively.

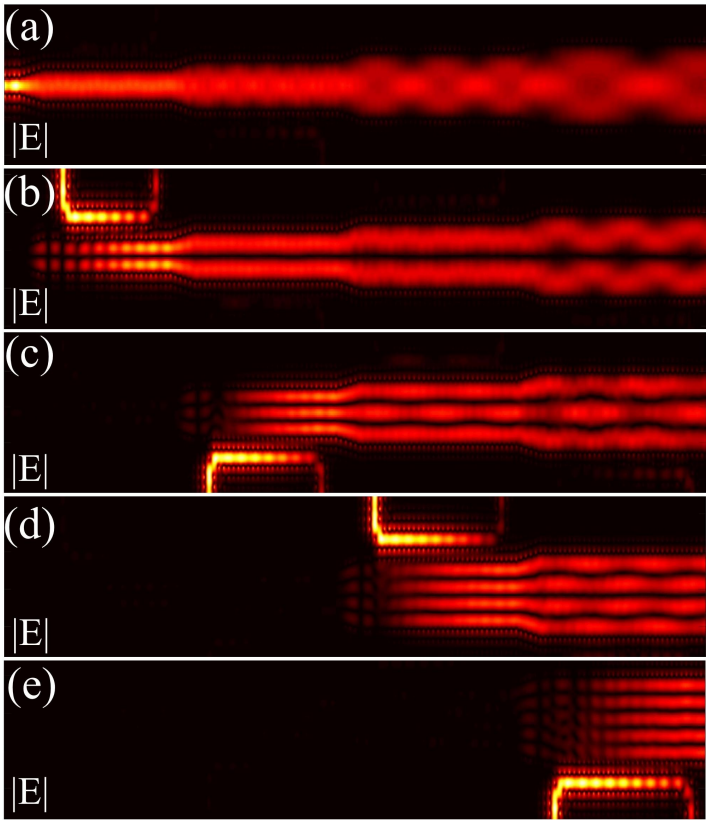

Figure 7.11 The electric field distribution when the TE_0 mode is input from (a) Port1, (b) Port2, (c) Port3, (d) Port4, and (e) Port5, at wavelength of 1.55 μm.

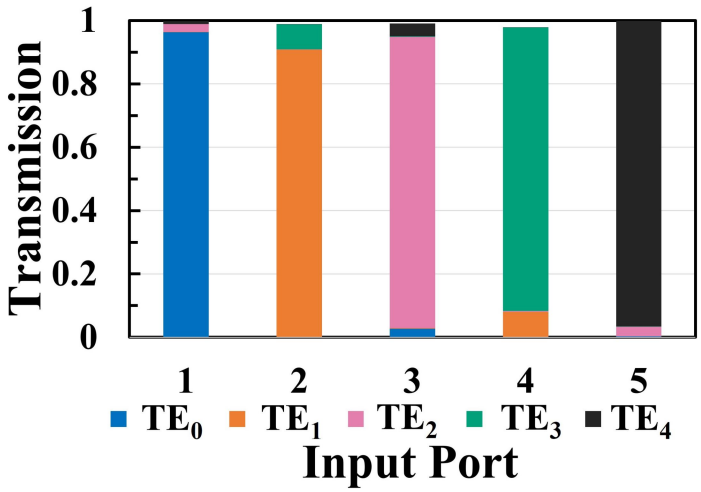

Figure 7.12 The transmission of each mode when the TE_0 mode is input from each port, at wavelength of 1.55 μm.

7.5 Ultra-compact 2-mode MUX using air-hole type PCWs

The schematic diagrams of the 3D PC structure and its plane view considered in this study are shown in Fig. 7.13. It consists of Si plate with the thickness of d_{Si}. Air-holes with the radius of r are arranged in triangular lattice with the lattice constant of a. The refractive index of the 3D Si slab is set to $n_{Si} = 3.48$. Here, we examine an equivalent 2D structure with the equivalent refractive index $n_{Si(eq)}$, because the purpose of this work is to show the theoretical possibility of mode MUX based on air-hole PCWs, which have not been considered yet.

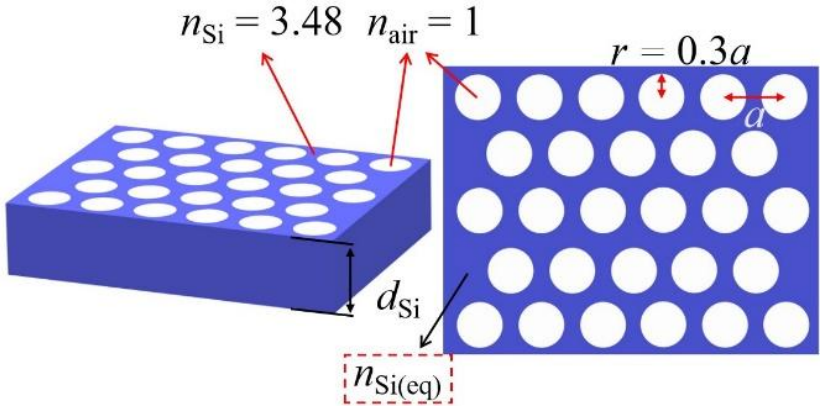

Figure 7.13 The schematic diagrams of the 3D PC structure (left) and its plane view (right).

The equivalent 2D structure to the 3D structure is determined as follows. In this study, all the calculations were done with FDTD. Figure 7.14 (a) shows normalized frequencies (a/λ) of the upper edge, center, and lower edge of the PBG for 2D PC as a function of $n_{Si(eq)}$. Figure 7.14 (b) shows the same one for 3D PC as a function of d_{Si}. Figure 7.14 (a) and (b) are calculated under the parameters of a = 0.41 μm and $r = 0.3a$. For both Figures, the PBG widths are also plotted for the right axis. The PBG width and the position are changed with the parameters. Figure 7.15 (a) shows the 2D and 3D PBG width as a function of $n_{Si(eq)}$ (lower horizontal axis) and d_{Si} (upper horizontal axis). The 3D PBG width is not so changed with d_{Si}, while the 2D PBG width has its maximum around $n_{Si(eq)} = 3.037$, where the difference between 2D and 3D PBGs is small. To ensure that the higher-order mode and the fundamental mode can appear simultaneously in the PBG, we selected the widest

2D PBG when the $n_{Si(eq)}$ = 3.037 as the parameter for subsequent calculation. Figure 7.15 (b) shows the 2D and 3D normalized frequency at the center of the PBGs as a function of $n_{Si(eq)}$ and d_{Si}. The center frequency of the 3D PC at d_{Si} = 460 nm is equal to the center frequency of the 2D PC at $n_{Si(eq)}$ = 3.037, where the PBG widths are also similar between 2D and 3D PCs. Therefore, a 3D PC with d_{Si} = 460 nm can be well approximated by a 2D PC with $n_{Si(eq)}$ = 3.037. PBG parameters for these 2D and 3D PCs are summarized in Table 7.1, and hereafter, we use them for the 2D equivalent PC. It should be noted that 3D PBG width is slightly larger for smaller values of d_{Si}, as shown in Fig. 7.15 (a) (although the difference is very small). Therefore, there is a possibility that thinner Si slab will lead to better performance in 3D design. However, as stated above, the purpose of this paper is to show mode multiplexing possibility in air-hole PCWs, and therefore, we used above parameters in this work. Full optimization of 3D structure will be reported elsewhere.

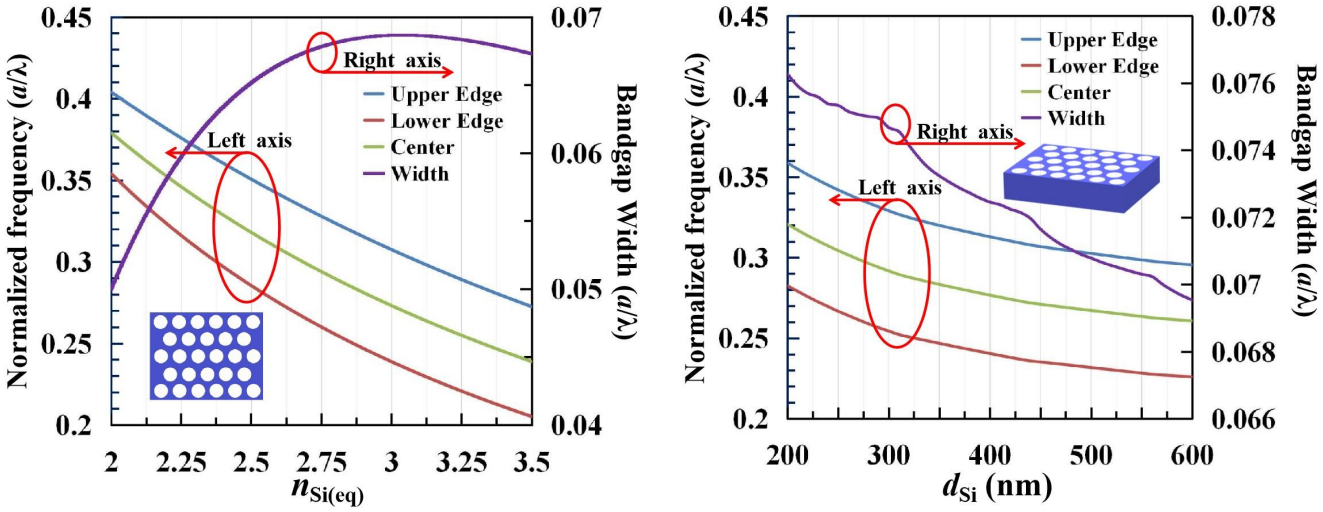

(a) 2D PBG structure as a function of $n_{Si(eq)}$.

(b) 3D PBG structure as a function of d_{Si}.

Figure 7.14 PBG parameters of air-hole PC.

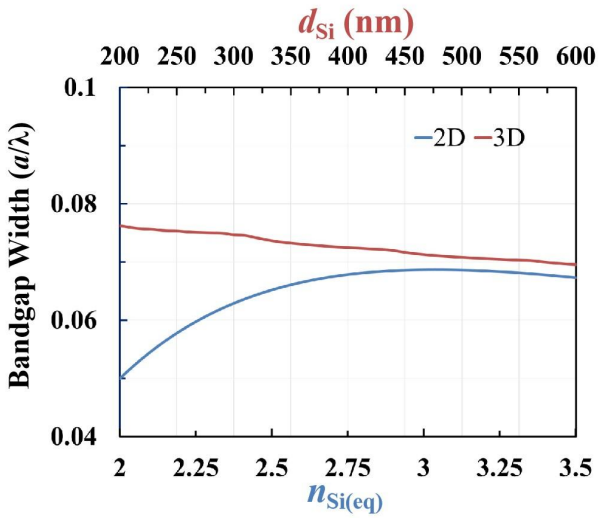

(a) PBG width of 2D and 3D PCs.

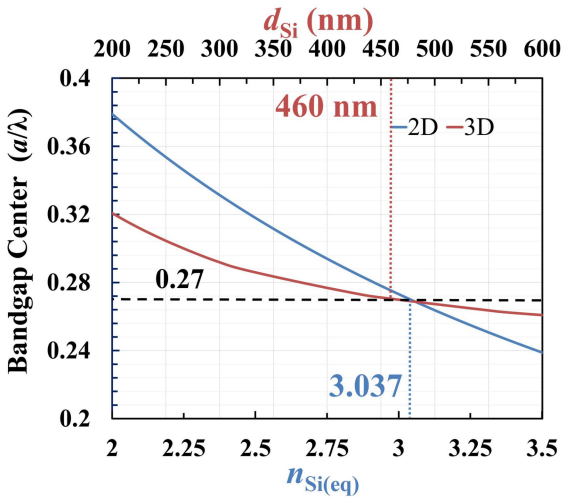

(b) PBG center frequency of 2D and 3D PCs.

Figure 7.15 Comparisona of air-hole PC PBG parameters in 2D and 3D situations.

Table 7.1 Bandgap parameters (a/λ)

$r = 0.3a$	2D structure	3D structure
	$n_{Si(eq)} = 3.037$	$d_{Si} = 460$ nm
Upper edge	0.30463	0.30605
Lower edge	0.23596	0.23465
Center	0.27029	0.27035
Width	0.06868	0.07141

Once the PC structure is determined, the next task is to investigate the guided modes. A line defect with the width of W is introduced into a complete PC by removing an array of air holes, forming a PCW. Hereafter, the lattice constant is set to a = 0.41 μm. For this lattice constant, normalized frequency of 0.265 corresponds to a wavelength of 1550 nm. Figure 7.16 (a) shows the dispersion curve of the PCW with W = 0.632 μm. The hatched area is the PBG. The waveguide is single-mode for the normalized frequency from 0.259 to 0.282 under the light line. Here, we define the *xyz* coordinate as shown in the inset of Fig. 7.16 (a), and TE mode is defined as the modes, whose principal electromagnetic components are H_z, E_x, and E_y. Figure 7.16 (b) shows the dispersion curve of the

PCW with W = 0.763 μm. By increasing the width, a higher-order mode (TE_1) appears in the PBG. There are two curves for the mode and labeled as TE_1-A and -B modes. They are also under the light line and can be used for the guided mode. Figure 7.16 (c) shows the dispersion curves of PCWs with W = 0.632 and 0.763 μm superimposed on the same Figure (Here, we only focus on the TE_0 mode when W = 0.632 μm and the TE_1 modes when W = 0.763 μm). The TE_0 mode of the single-mode waveguide and the TE_1-B mode of the multimode waveguide have an intersection point at the normalized frequency of 0.265, and the propagation constant β of the two modes are both 0.355. Therefore, the TE_1 mode can be excited by using the phase matching conditions [17].

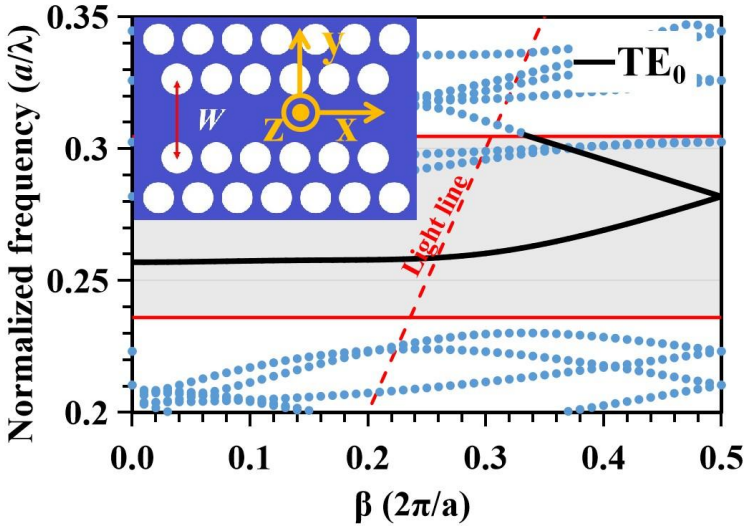

(a) W = 0.632 μm.

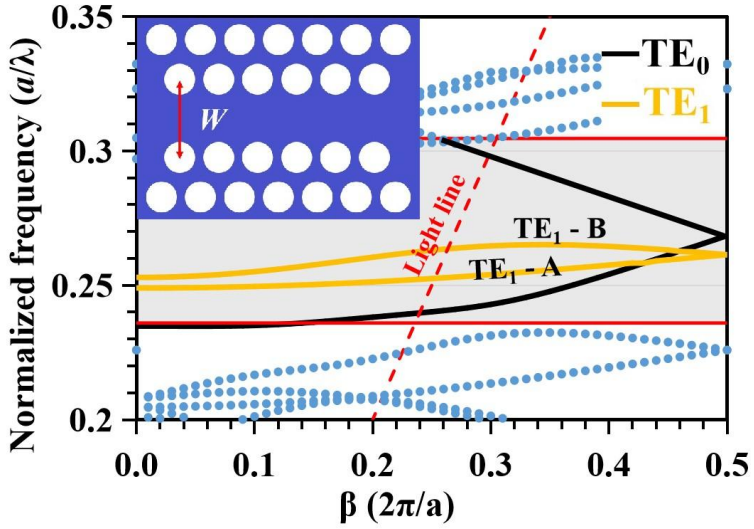

(b) W = 0.763 μm.

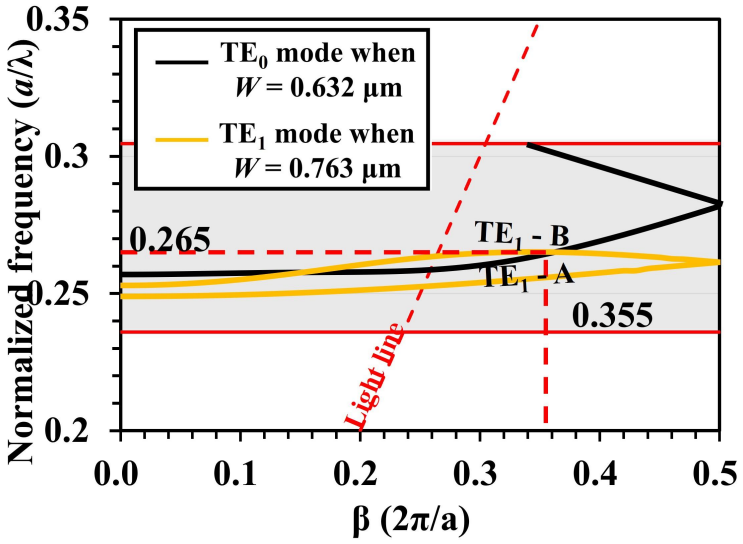

(c) The dispersion curves of PCWs in Fig. 7.16 (a) and (b) superimposed on the same Figure.

Figure 7.16 Dispersion curves of the PCW.

Here, we consider a mode MUX based on an ADC. It consists of a single-mode waveguide with the width of W_1 and a multi-mode waveguide with the width of W_2 arranged in parallel as shown in Fig. 7.17. Two rows of air-holes are placed between two waveguides and the separation between two waveguides is 0.355 μm. Figure 7.18 shows the propagation constant β of TE_0 and TE_1 modes as a function of the waveguide width W at $a/\lambda = 0.265$ (λ = 1550 nm for a = 0.41 mm). For the TE_0 mode with $W_1 = 1.78*(a*\cos(\pi/6)) = 0.632$ μm, the phase matching conditions are satisfied for TE_1 mode with $W_2 = 2.15*(a*\cos(\pi/6)) = 0.763$ μm.

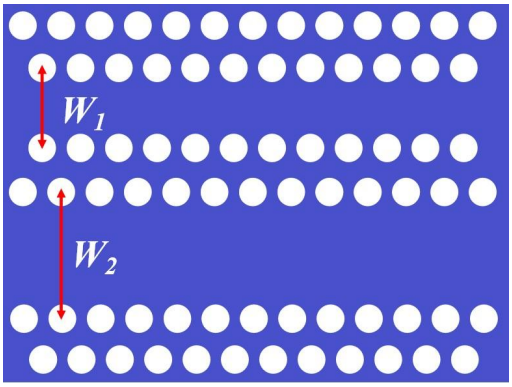

Figure 7.17 Mode MUX structure.

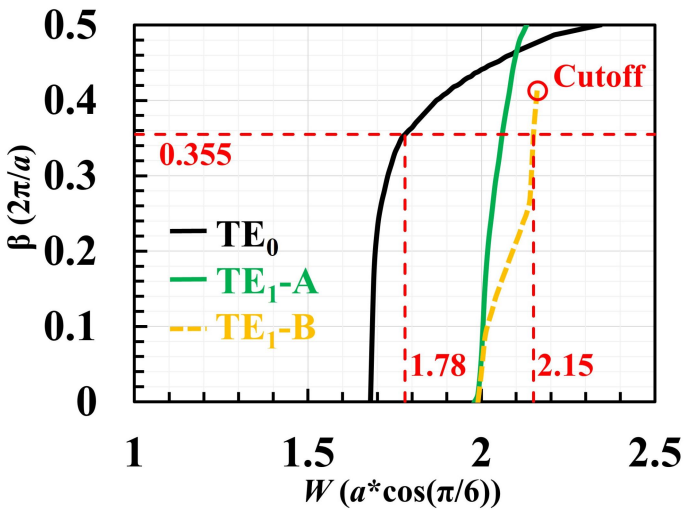

Figure 7.18 Relationship between propagation constant β and the waveguide width W at $a/\lambda = 0.265$.

Figure 7.19 shows the field distribution of TE_0-TE_1 mode MUX, where W_1 and W_2 are 0.632 and 0.763 μm, at the wavelength 1550 nm. As we can see, the TE_0 mode launched from narrow waveguide is coupled to the TE_1 mode of wide waveguide. The coupling length is only 2.05 μm for the lattice constant a = 0.41 μm. The typical coupling length for the ADC based on Si-wire waveguides with the waveguide separation of 200 nm around 1550 nm is about 10 μm [22]. Here, the coupling length of proposed PCW ADC is 1/5 even though the waveguide separation is increased to 0.355 μm. Figure 7.20 shows the calculated transmission spectrum of the TE_1 mode MUX for the lattice constant a = 0.41 μm. Since the TE_1-B mode only exists in the normalized frequency range of a/λ = 0.2615 ~ 0.2652, we only show the results in the range, where the TE_1-B mode exists. The transmissions of the TE_1 mode at the wavelength of 1550 nm are greater than 90%. However, the transmissions at other wavelengths are degraded, especially for longer wavelength region. This partly comes from that the phase matching condition is not satisfied for the other wavelength region. Figure 7.21 shows the effective index difference, Δn_{eff} spectrum between TE_0 and TE_1-B modes. Dn_{eff} is zero at 1550 nm and is not zero for other wavelengths, and the value is large for longer wavelength side. Therefore, the phase mismatch seems to be the dominant factor for longer wavelength side degradation.

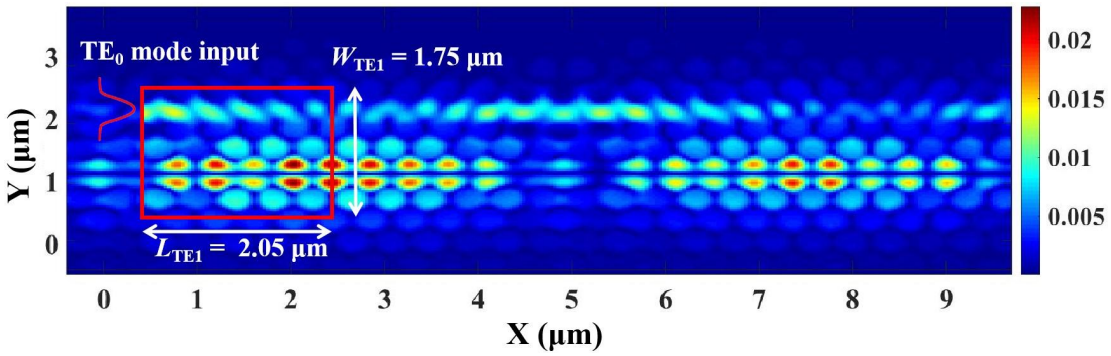

Figure 7.19 Magnetic field distribution $|H_z|$ of TE_0-TE_1 mode MUX at a/λ = 0.265.

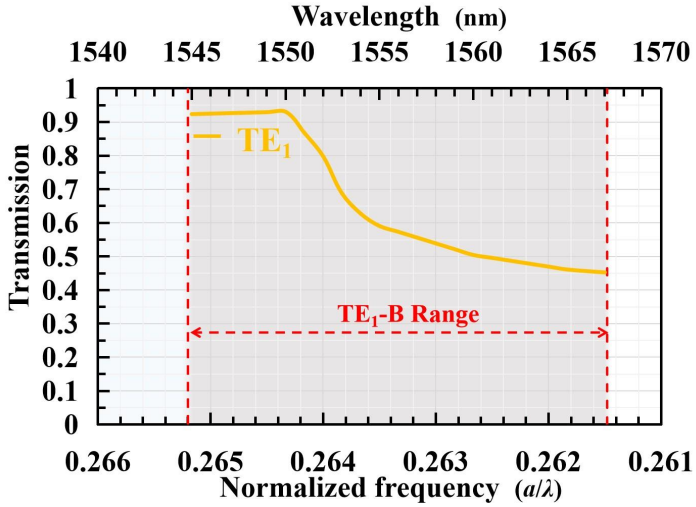

Figure 7.20 Transmission spectrum of TE_1 mode MUX.

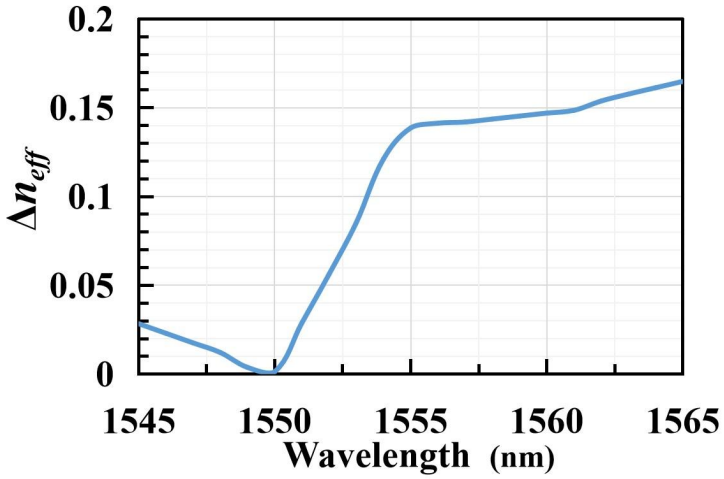

Figure 7.21 Δn_{eff} spectrum.

Chapter 8 Conclusion

We have proposed a 6-mode-selective photonic lantern multiplexer based on PLC and verified that the device can selectively multiplex six modes of E_{11}, E_{21}, E_{12}, E_{22}, E_{31}, and E_{13}, which have low MDL is 0.42 dB when the wavelength is 1550 nm. Crosstalk is lower than −12.93 dB and low loss which is lower than 0.5 dB in the C+L band.

We then proposed a broadband 10-mode photonic lantern mode multiplexer based on three-layer PLC structure and verified that the device can realize E_{11}, E_{21}, E_{12}, E_{22}, E_{31}, E_{13}, E_{32}, E_{23}, E_{41}, and E_{14} ten-mode multiplexing, which have crosstalk less than −10.97 dB and low MDL 1.43 dB at wavelength 1550 nm, and less than -8.74 dB in the C-band, and also verified that we can skip unwanted modes to directly excite the required mode by optimizing the device. Although we focused on silica-based PLC in this paper, a polymer waveguide platform may be suitable for realizing the proposed device, at which two-layer structure was already realized [27]. We consider that the design method proposed here can be applied to different material platforms.

Then we proposed three types of PLC tapered structures that can be applied in different scenarios using FAQUAD. These structures enable mode conversions of E_{31}-E_{13}, as well as E_{31}-LP_{02} and E_{13}-LP_{21b}, respectively. In the case of the E_{31}-E_{13} mode converter, compared with the one-stage linear taper greater than 30000 μm, and the previous three-stage linear taper of greater than 12000 μm [17], the FAQUAD taper can achieve a transmission over 99% with a length of 4000 μm. In the case of the E_{31}-LP_{02}, and E_{13}-LP_{21b} mode converter for 6-mode photonic lantern MUX, compared with the one-stage linear taper greater than 50000 μm, and the previous two-stage linear taper of greater than 6000 μm [17], the FAQUAD taper can achieve a transmission over 99% with a length of 4000 μm. In

the case of the E_{31}-LP_{02}, and E_{13}-LP_{21b} mode converter for 10-mode photonic lantern MUX, compared with the one-stage linear taper greater than 2 m, the FAQUAD taper can achieve a transmission over 98% with a length of 47500 μm.

Finally, we proposed an ultra-compact air-hole PC mode MUX using waveguide phase matching principle. 2-mode (TE_0 and TE_1 modes) multiplexing is possible and the size of the MUX can be reduced to 1/5 compared with those of Si-wire based mode MUX [22]. > 90% transmission is possible at the wavelength of 1550nm.

Acknowledgements

Here, I would like to express my sincere thanks to Professor Kunimasa Saitoh from the Laboratory of Information and Communication Photonics at the School of Information Science, Hokkaido University, who has been patiently guiding my research life for past few years and helping me solve problems during the research process.

At the same time, I also want to deeply thank the strict and gentle associate professor Takeshi Fujisawa and in the same laboratory and associate professor Takanori Sato form Intelligent Communications Laboratory at the School of Information Science, Hokkaido University.

Then, I would like to thank all the students in the laboratory who have always taken care of me and brought me a lot of warmth in my life and lots of help in my study.

Finally, I would like to express my special thanks to my parents and family who raised me and provided support for my study abroad life. And I am very grateful to my fiancée who laughs with me when I am happy and gives me endless patience and companionship when I am down.

Research achievements

Academic journals

(1) H. Wang, T. Fujisawa, T. Sato, T. Mori, T. Sakamoto, Y. Yamashita, R. Imada, K. Nakajima, and K. Saitoh, "6-mode and 10-mode photonic lantern mode multi/demultiplexer based on silica planar Lightwave circuit", Opt. Commun. Vol: 529, No: 129098, 2023.

(2) H. Wang, T. Fujisawa, T. Sato, M. Wada, T. Mori, T. Sakamoto, R. Imada, T. Matsui, K. Nakajima, and K. Saitoh, "Design of PLC E31-E13 and E-LP tapered mode converters using fast quasiadiabatic dynamics", IEICE ELEX.Vol: 20, No: 23, 2023.

Drafts of Lectures at International Conferences

(1) H. Wang, T. Fujisawa, T. Sato, T. Mori, T. Sakamoto, Y. Yamashita, R. Imada, K. Nakajima, and K. Saitoh, "Optimization of PLC 10-mode photonic lantern mode multiplexer". The 7th International Symposium on Extremely Advanced Transmission Technologies (EXAT), Paper P-06, Matsue, Japan, May 17-19, 2023.

(2) H. Wang, T. Fujisawa, T. Sato, and K. Saitoh, "Proposal of an ultra-compact mode multiplexer using air-hole type photonic crystal waveguides". The 28th OptoElectronics and Communications Conference (OECC), Paper OECC2023-0317-5, Shanghai, China, July 2-6, 2023.

(3) H. Wang, T. Fujisawa, T. Sato, and K. Saitoh, "Proposal of 5-mode multiplexer using pillar type photonic crystal waveguides". Microoptics Conference (MOC), Paper PO-3, Miyazaki, Japan, Sep. 24-27, 2023.

Drafts of Lectures at Domestic Conferences

(1) Han Wang, Yusuke Sawada, Takeshi Fujisawa, Taiji Sakamoto, Takashi Matsui, Kazuhide Nakajima, Kunimasa Saitoh, “Proposal of PLC 6-mode-selective Photonic Lantern Mode Multiplexer”. IEICE Society Conference, C-3/4-45, Sep. 15-18, 2020.

(2) H. Wang, Y. Sawada, T. Fujisawa, T. Sato, T. Mori, T. Sakamoto, Y. Yamashita, R. Imada, K. Nakajima, and K. Saitoh, “Proposal of PLC 10-mode-selective Photonic Lantern Mode Multiplexer”. IEICE Society Conference, C-3/4-27, Sep. 14-17, 2021.

References

[1] K. C. Kao, G. A. Hockham, and I. E. E. Synopsis, “Dielectric-fibre surface waveguides for optical frequencies,” *Proc. Iee*, vol. 113, no. 7, pp. 1151–1158, 1966.

[2] T. Morioka, “New generation optical infrastructure technologies: 'EXAT initiative' towards 2020 and beyond,” *OptoElectronics and Communications Conference*, pp. 1–2, Jul, 2009, doi: 10.1109/OECC.2009.5213198.

[3] T. Morioka, “Recent Progress in Space-Division Multiplexed Transmission Technologies,” in *Optical Fiber Communication Conference/National Fiber Optic Engineers Conference*, 2013, p. OW4F.2, 2013, doi: 10.1364/OFC.2013.OW4F.2.

[4] R. Nagase, “How to connect multicore and multimode fibers,” *Conf. Opt. Fiber Commun. Tech. Dig. Ser.*, no. 2, pp. 2–4, 2014, doi: 10.1109/OFC.2014.6886943.

[5] Y. Tottori, H. Tsuboya, T. Kobayashi, and M. Watanabe, “Integrated optical connection module for 7-core multi-core fiber and 7 single mode fibers,” *IEEE Photonics Soc. Summer Top. Meet. Ser. PSSTMS*, vol. 2, no. 2, pp. 82–83, 2013, doi: 10.1109/PHOSST.2013.6614463.

[6] N. Zhao, B. Huang, R. Amezcua-Correa, X. Li, and G. Li, “Few-mode fiber optical parametric amplifier,” *Opt. Fiber Commun. Conf.* no. May, pp. 2–5, 2013, doi: 10.1364/ofc.2013.otu2d.5.

[7] G. Labroille, P. Jian, N. Barré, B. Denolle, and J.-F. Morizur, “Mode Selective 10-Mode Multiplexer based on Multi-Plane Light Conversion,” in *Optical Fiber Communication Conference*, p. Th3E.5, 2016, doi: 10.1364/OFC.2016.Th3E.5.

[8] R. Ryf *et al.*, “Mode-division multiplexing over 96 km of few-mode fiber using coherent 6×6 MIMO processing,” *J. Light. Technol.*, vol. 30, no. 4, pp. 521–531, 2012, doi: 10.1109/JLT.2011.2174336.

[9] S. H. Chang *et al.*, “Mode division multiplexed optical transmission enabled by all–fiber mode multiplexer,” *Opt. Express*, vol. 22, no. 12, p. 14229, 2014, doi: 10.1364/oe.22.014229.

[10] N. K. Fontaine, R. Ryf, J. Bland-Hawthorn, and S. G. Leon-Saval, “Geometric requirements for photonic lanterns in space division multiplexing,” *Opt. Express*, vol. 20, no. 24, p. 27123, 2012, doi: 10.1364/oe.20.027123.

[11] S. G. Leon-Saval, N. K. Fontaine, J. R. Salazar-Gil, B. Ercan, R. Ryf, and J. Bland-Hawthorn, “Mode-selective photonic lanterns for space-division multiplexing,” *Opt. Express*, vol. 22, no. 1, p. 1036, 2014, doi: 10.1364/oe.22.001036.

[12] A. M. Velazquez-Benitez *et al.*, “Six mode selective fiber optic spatial multiplexer,” *Opt. Lett.*,

vol. 40, no. 8, p. 1663, 2015, doi: 10.1364/ol.40.001663.

[13] S. G. Leon-Saval, T. A. Birks, J. Bland-Hawthorn, and M. Englund, "Multimode fiber devices with single-mode performance," *Opt. Lett.*, vol. 30, no. 19, p. 2545, Oct. 2005, doi: 10.1364/ol.30.002545.

[14] S. G. Leon-Saval, "Photonic Lantern: harnessing multimode photonics for optical communications," *Asia Communications and Photonics Conference*, vol. Part F83-A, p. Su3A.5, 2017, doi: 10.1364/ACPC.2017.Su3A.5.

[15] J. van Weerdenburg *et al.*, "10 Spatial mode transmission using low differential mode delay 6-LP fiber using all-fiber photonic lanterns," *Opt. Express*, vol. 23, no. 19, p. 24759, Mar. 2015, doi: 10.1364/oe.23.024759.

[16] A. M. Velázquez-Benítez *et al.*, "Scaling photonic lanterns for space-division multiplexing," *Sci. Rep.*, vol. 8, no. 1, pp. 1–9, 2018, doi: 10.1038/s41598-018-27072-2.

[17] K. Saitoh *et al.*, "PLC-based mode multi/demultiplexers for mode division multiplexing," *Opt. Fiber Technol.*, vol. 35, pp. 80–92, Feb. 2017, doi: 10.1016/j.yofte.2016.08.002.

[18] N. Hanzawa *et al.*, "Demonstration of PLC-based six-mode multiplexer for mode division multiplexing transmission," *Eur. Conf. Opt. Commun.*, vol. 2015-Novem, no. 1, pp. 9–11, 2015, doi: 10.1109/ECOC.2015.7341717.

[19] T. Fujisawa *et al.*, "Scrambling-Type Three-Mode PLC Multiplexer Based on Cascaded Y-Branch Waveguide with Integrated Mode Rotator," *J. Light. Technol.*, vol. 36, no. 10, pp. 1985–1992, 2018, doi: 10.1109/JLT.2018.2798619.

[20] M. Shirata, T. Fujisawa, T. Sakamoto, T. Matsui, K. Nakajima, and K. Saitoh, "Design of small mode-dependent-loss scrambling-type mode (de)multiplexer based on PLC," *Opt. Express*, vol. 28, no. 7, p. 9653, 2020, doi: 10.1364/oe.387890.

[21] H. Wang *et al.*, "6-mode and 10-mode photonic lantern mode multi/demultiplexers based on silica planar lightwave circuit," *Opt. Commun.*, vol. 529, p. 129098, Feb. 2023, doi: 10.1016/j.optcom.2022.129098.

[22] Y. Sawada, T. Fujisawa, and K. Saitoh, "Broadband and compact silicon mode converter designed using a wavefront matching method," *Opt. Express*, vol. 28, no. 25, p. 38196, 2020, doi: 10.1364/oe.411769.

[23] Q. Huang, Y. Wu, W. Jin, and K. S. Chiang, "Six-Mode Multiplexer With Cascaded Vertical Asymmetric Waveguide Directional Couplers," *J. Light. Technol.*, vol. 36, no. 14, pp. 2903–2911, 2018, doi: 10.1109/JLT.2018.2829143.

[24] L. Zuo, K. Chen, and K. S. Chiang, "Ultra-Broadband Mode Multiplexer with Cascaded

Adiabatic Vertical Directional Couplers," *Opt. Lett.*, vol. 42, no. 3, p. 407, 2017, doi: 10.1364/OL.42.000407

[25] J. Dong, W. Jin, and K. S. Chiang, "Mode multiplexer based on integrated horizontal and vertical polymer-waveguide directional couplers," *Conf. Lasers Electro-Optics Eur. - Tech. Dig.*, vol. 2015-Augus, no. c, pp. 1–2, 2015.

[26] A. Lobato *et al.*, "Maximum-Likelihood Detection in Few-Mode Fiber Transmission With Mode-Dependent Loss," *IEEE Photonics Technol. Lett.*, vol. 25, no. 12, pp. 1095–1098, Jun. 2013, doi: 10.1109/LPT.2013.2257724.

[27] Y. Wu and K. S. Chiang, "Ultra-broadband mode multiplexers based on three-dimensional asymmetric waveguide branches," *Opt. Lett.*, vol. 42, no. 3, p. 407, 2017, doi: 10.1364/ol.42.000407.

[28] T.-Y. Lin, F.-C. Hsiao, Y.-W. Jhang, C. Hu, and S.-Y. Tseng, "Mode conversion using optical analogy of shortcut to adiabatic passage in engineered multimode waveguides," *Opt. Express*, vol. 20, no. 21, p. 24085, Oct. 2012, doi: 10.1364/OE.20.024085.

[29] S. Martínez-Garaot, A. Ruschhaupt, J. Gillet, T. Busch, and J. G. Muga, "Fast quasiadiabatic dynamics," *Physical Review A - Atomic, Molecular, and Optical Physics*, vol. 92, no. 4. 2015, doi: 10.1103/PhysRevA.92.043406.

[30] H.-C. Chung, K.-S. Lee, and S.-Y. Tseng, "Short and broadband silicon asymmetric Y-junction two-mode (de)multiplexer using fast quasiadiabatic dynamics," *Opt. Express*, vol. 25, no. 12, p. 13626, 2017, doi: 10.1364/oe.25.013626.

[31] H.-C. Chung and S.-Y. Tseng, "Ultrashort and broadband silicon polarization splitter-rotator using fast quasiadiabatic dynamics," *Opt. Express*, vol. 26, no. 8, p. 9655, 2018, doi: 10.1364/oe.26.009655.

[32] H. C. Chung, S. Martínez-Garaot, X. Chen, J. G. Muga, and S. Y. Tseng, "Shortcuts to adiabaticity in optical waveguides," *Epl*, vol. 127, no. 3, pp. 159–167, 2019, doi: 10.1209/0295-5075/127/34001.

[33] H.-C. Chung, C.-H. Chen, Y.-J. Hung, and S.-Y. Tseng, "Compact polarization-independent quasi-adiabatic 2×2 3 dB coupler on silicon," *Opt. Express*, vol. 30, no. 2, p. 995, 2022, doi: 10.1364/oe.446492.

[34] Y.-L. Wu, F.-C. Liang, H.-C. Chung, and S.-Y. Tseng, "Adiabaticity engineering in optical waveguides," *Opt. Express*, vol. 28, no. 20, p. 30117, 2020, doi: 10.1364/oe.402545.

[35] Y.-J. Hung *et al.*, "Mode-evolution-based silicon-on-insulator 3 dB coupler using fast quasiadiabatic dynamics," *Opt. Lett.*, vol. 44, no. 4, p. 815, 2019, doi: 10.1364/ol.44.000815.

[36] T. Sato *et al.*, “Design of silica-PLC LP 11 mode rotator based on adiabatic mode conversion,” *Opt. Express*, vol. 31, no. 15, p. 23910, Jul. 2023, doi: 10.1364/OE.493501.

[37] H. Wang *et al.*, “Design of PLC E_{31}-E_{13} and E-LP tapered mode converters using fast quasiadiabatic dynamics,” *IEICE Electron. Express*, vol. 20, no. 23, p. 20.20230392, Dec. 2023, doi: 10.1587/elex.20.20230392.

[38] Y. Zhuang, H. Chen, K. Ji, and Y. Hu, “On-chip hybrid demultiplexer for mode and coarse wavelength division multiplexing,” *Appl. Phys. B Lasers Opt.*, vol. 125, no. 1, p. 0, 2019, doi: 10.1007/s00340-018-7123-6.

[39] K. Ji, H. Chen, Y. Zhuang, and W. Zhou, “A hybrid multiplexer/de-multiplexer for wavelength-mode-division based on photonic crystals,” *J. Mod. Opt.*, vol. 65, no. 14, pp. 1623–1633, 2018, doi: 10.1080/09500340.2018.1457184.

[40] O. M. Nawwar, H. M. H. Shalaby, and R. K. Pokharel, “Photonic crystal-based compact hybrid WDM/MDM (De)multiplexer for SOI platforms,” *Opt. Lett.*, vol. 43, no. 17, p. 4176, 2018, doi: 10.1364/ol.43.004176.

[41] W. Zhou, Y. Zhuang, K. Ji, and H. Chen, “Multi/demulti-plexer based on transverse mode conversion in photonic crystal waveguides,” *Opt. Express*, vol. 23, no. 19, p. 24770, 2015, doi: 10.1364/oe.23.024770.

[42] H. Wang, T. Fujisawa, T. Sato, and K. Saitoh, “Proposal of 5-mode multiplexer using pillar type photonic crystal waveguides,” *Microoptics Conference*, no. 1, pp. 1–2, Sep, 2023, doi: 10.23919/MOC58607.2023.10302931.

[43] H. Wang, T. Fujisawa, T. Sato, and K. Saitoh, “Proposal of an ultra-compact mode multiplexer using air-hole type photonic crystal waveguides,” *Opto-Electronics and Communications Conference*, vol. 3, pp. 1–3, Jul, 2023, doi: 10.1109/OECC56963.2023.10209814.

[44] K. Saitoh and M. Koshiba, “Approximate scalar finite-element beam-propagation method with perfectly matched layers for anisotropic optical waveguides,” *J. Light. Technol.*, vol. 19, no. 5, pp. 786–792, May 2001, doi: 10.1109/50.923493.

[45] Y. Gao *et al.*, “Compact six-mode (de)multiplexer based on cascaded asymmetric Y-junctions with mode rotators,” *Opt. Commun.*, vol. 451, no. February, pp. 41–45, 2019, doi: 10.1016/j.optcom.2019.06.010.

[46] L. Shen *et al.*, “Design of highly mode group selective photonic lanterns with geometric optimization,” *Appl. Opt.*, vol. 57, no. 24, p. 7065, 2018, doi: 10.1364/ao.57.007065.

[47] G. R. Castillo, L. Labrador-Paez, F. Chen, S. Camacho-Lopez, and J. R. V. De Aldana, “Depressed-Cladding 3-D Waveguide Arrays Fabricated with Femtosecond Laser Pulses,” *J.*

Light. Technol., vol. 35, no. 13, pp. 2520–2525, 2017, doi: 10.1109/JLT.2017.2696163.

[48] S. Gross, M. Ams, S. G. Leon-Saval, and M. J. Withford, "Ultrafast laser inscribed mode-group-selective 6-mode photonic lanterns for mode-Division multiplexing," *Opt. InfoBase Conf. Pap.*, vol. Part F82-C, no. 2013, p. 6736, 2017, doi: 10.1109/cleoe-eqec.2017.8087236.

[49] H. Chen, N. K. Fontaine, R. Ryf, B. Guan, S. J. B. Yoo, and T. A. M. J. Koonen, "Design constraints of photonic-lantern spatial multiplexer based on laser-inscribed 3-D waveguide technology," *J. Light. Technol.*, vol. 33, no. 6, pp. 1147–1154, 2015, doi: 10.1109/JLT.2014.2370673.

[50] Yunfei Wu and K. S. Chiang, "Broadband photonic lantern mode multiplexers based on multilayer polymer waveguides," *Optoelectronics and Communications Conference*, pp. 1–3, Jun, 2015, doi: 10.1109/OECC.2015.7340134.

[51] Y. Yamashita *et al.*, "Excitation of LP21b and LP02 modes with PLC-based tapered waveguide for mode-division multiplexing," *Optoelectronics and Communications Conference*, pp. 31–33, 2016.

[52] D. F. Siriani and J.-L. Tambasco, "Adiabatic guided wave optics – a toolbox of generalized design and optimization methods," *Opt. Express*, vol. 29, no. 3, p. 3243, 2021, doi: 10.1364/oe.415653.

[53] Y. Zhang, Y. Zhang, and B. Li, "Optical switches and logic gates based on self-collimated beams in two-dimensional photonic crystals," *Opt. Express*, vol. 15, no. 15, p. 9287, 2007, doi: 10.1364/oe.15.009287.

[54] E. Tresa, P. Mankar, and J. Digge, "Silicon based 2D Photonic Crystal Power Splitter for Optical Network," *Int. Conf. Innov. Trends Adv. Eng. Technol*, pp. 144–147, 2019, doi: 10.1109/ICITAET47105.2019.9170243.